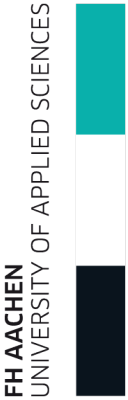

European Master in Nuclear Applications

Monte Carlo Simulation of the Radiation Induced Material Damage in a Tantalum Target

---

Author:
Niklas Ophoven
Matr.-Nr.: 4015585

Supervisors:
1st: Prof. Dr. Christoph Langer
2nd: Dr. Jingjing Li

A thesis submitted in partial fulfillment of the requirements for the degree of

MASTER OF SCIENCE

FH Aachen University of Applied Sciences

Faculty 3 Chemistry and Biotechnology

Campus Jülich

October 2020

Statutory Declaration

I hereby declare that this research thesis completely is my own original work and was written without the use of any sources beyond those cited, and all passages and ideas taken from other sources are cited accordingly. I further declare that, neither parts or the whole thesis have been submitted to any other university or institution for a degree.

Signature **Location, Date**

Abstract

Neutrons are an ideal probe to examine condensed matter and invaluable for fundamental physics research in scattering experiments as well as for medical purposes. Drawbacks of conventional neutron provision by nuclear reactors regarding the disposal of radioactive waste and governmentals' restrictions triggered a transition towards advanced and superior compact accelerator based neutron sources. Radiation induced material damage is of major concern to limit a target's lifetime due to detrimental alterations of macroscopic properties. In view of a continuously growing demand in neutron beam time worldwide, hence extensive radiation damage analyzes for a classification of the expected damage play a crucial key role.

In the frame of this thesis the expected radiation damage in the tantalum target designed for the Jülich High Briliance Neutron Source project (HBS) is investigated by strong Monte Carlo programs, FLUKA and SRIM. The extracted information on the induced damage patterns focus on atomic displacements as a powerful standard indicator for radiation damage and are supplemented by information on energy deposition and neutron spectra. The back of the target represents the most endangered area, with primary protons as the main damage contributors. Neutrons' minor contribution, totally regardless of thermal moderators, was found out to be a material specific issue, as the mean free transport pathlength λ_{tr} exceeds the target thickness, resulting in rare interaction events. Intercode comparisons highlight differences between the physical models of the displacements per atom (dpa) concept. Using the Norget-Robinson-Torrens (NRT) model, based on the nuclear deposited energy and consideration of defect recombination processes, FLUKA is superior over SRIM, which is based on the model after Kinchin and Pease (KP) and inherently overestimates the predicted damage.

In the context of a final damage assessment, the minimum lifetime τ_{min} of the target that can be reasonably expected is estimated carefully and qualitatively. A meticulous review of the sparsely literature defines great radiation resistance of tantalum and proposes τ_{min} to be roughly 2.5 years ($\sim$ 31 Ah). Though unclear at the moment, it is likely and rational to assume that this lifetime keeps to be valid at the actual irradiation conditions foreseen. A final clarification of the maximum lifetime requires challenging experimental investigations of irradiated samples.

Kurzfassung

Neutronen sind ideal für Untersuchungen kondensierter Materie und von enormen Wert für Grundlagenforschung in Physik durch Streuexperimente sowie medizinischen Zwecken. Nachteile konventioneller Versorgung mit Neutronen durch Kernreaktoren bezüglich Entsorgung radioaktiven Abfalls und Restriktionen der Regierungen haben einen Wandel hin zu überlegenen kompakten beschleunigerbasierten Neutronenquellen ausgelöst. Strahleninduzierte Materialschäden limitieren die Lebensdauer eines Targets auf Grund nachteiliger Veränderungen in makroskopischen Eigenschaften. Angesichts einer kontinuierlich steigenden Nachfrage für Neutronenstrahlzeit weltweit spielen daher umfangreiche Strahlschädenanalysen zwecks Einordnung der erwarteten Schäden eine entscheidende Schlüsselrolle.

Im Rahmen dieser Arbeit werden die erwarteten Strahlschäden im Tantaltarget des Jülich High Brilliance Neutron Source Projektes (HBS) mit starken Monte Carlo Programmen, FLUKA und SRIM, untersucht. Die erlangten Informationen über induzierte Schadensmuster konzentrieren sich auf Atomverschiebungen und werden ergänzt durch Informationen über Energiedeposition und Neutronenspektren. Die Rückseite des Targets ist die meist gefährdete Stelle, mit Primärprotonen als Hauptschadensverursacher. Der geringe Beitrag von Neutronen, völlig unabhängig von thermischen Moderatoren, liegt materialspezifisch begründet, da die mittlere freie Transportweglänge λ_{tr} größer als die Targetdicke zu seltenen Wechselwirkungen führt. Intercode-Vergleiche betonen Unterschiede in den physikalischen Modellen des displacements per atom (dpa) Konzeptes. Das Norget-Robinson-Torrens (NRT) Modell nutzend, basierend auf der nuklear deponierten Energie und Beachtung von Defektrekombinationsprozessen, ist FLUKA SRIM überlegen, da Letzteres auf dem Modell nach Kinchin und Pease (KP) basiert und den Schaden somit überschätzt.

Im Rahmen einer endgültigen Schadensbewertung wurde eine rationale minimale Lebenszeit τ_{min} des Targets vorsichtig und qualitativ geschätzt. Ein akribischer Abgleich der dünnen Literatur zeigt großes Widerstandsvermögen von Tantal gegen Strahlung und schlägt einen Wert von $\tau_{min} \approx 2{,}5$ Jahren ($\sim$ 31 Ah) vor. Es scheint wahrscheinlich und rational anzunehmen, dass dieser Wert auch unter realen Strahlbedingungen gültig bleibt. Eine finale Klärung der maximalen Lebenszeit erfordert herausfordernde experimentelle Untersuchungen bestrahlter Proben.

Acknowledgements

At this point I would like to take the opportunity to thank everyone who helped me during the time of my master thesis and acknowledge all the support I have received.

First of all I want to express Prof. Dr. Christoph Langer many thanks for the supervision of this thesis. Special thanks also go to him for all his efforts regarding a subsequent PhD position.

Thanks also go to Dr. Jingjing Li and Dr. Eric Mauerhofer for the local supervision of my work at the research centre Jülich. Whether in person or by email, they were always open minded and friendly towards me and had time for me whenever I encountered problems and questions. Their ideas and help always pushed advance into my work.
I want to thank Ms. Li especially for her efforts to get me the student job at the research centre and also for taking the role of the second supervisor of this thesis.

I want to thank all members of the HBS group for all the interesting scientific exchanges and for the given opportunity to present the current status of my work at regular meetings. In particular, my participation at the 5th HBS Workshop in Unkel in september 2019 as well as the 4th RIKEN-JCNS joint workshop in June 2020 were very new and nice experiences for me.

At the end, I also want to dedicate special thanks to my parents. I want to thank them for all the great help and support during my whole study time.

Table of Contents

List of Figures

List of Tables

List of Abbreviations

Abbreviation	**Meaning**
ASTM	American Society for Testing and Materials
BCA	Binary collision approximation
CANS	Compact accelerator based neutron source
CDR	Conceptual design report
CERN	Conseil Européen pour la Recherche Nucléaire
dpa	Displacements per atom
FLUKA	FLUktuierende KAskade, Fluctuating Cascade
FP	Frenkel pair
HBS	High Brilliance Neutron Source
JCNS	Jülich Centre for Neutron Science
KP	Kinchin and Pease
LINAC	Linear accelerator
LSS	Lindhard-Scharff-Schiøt
MC	Monte Carlo
MD	Molecular dynamics
NIEL	Non-ionizing energy loss
NRT	Norget-Robinson-Torrens
PD	Point defect
PKA	Primary knock-on atom
RPV	Reactor pressure vessel
SRIM	Stopping and Range of Ions in Matter
TDE	Threshold displacement energy

List of Symbols

Symbol	Description	Unit
α_0	Bohr radius	cm
α_{TF}	Thomas-Fermi screening length	cm
α_U	Universal screening length	cm
β	Fraction of the speed of light	
γ	Collisional parameter	
ΔE_K	Transferred energy	eV[a]
ΔE_{max}	Projectile maximum energy transfer to target	eV
ϵ_L	Lindhard reduced energy	
$\epsilon_{r,TF}$	Thomas-Fermi reduced energy	
$\epsilon_{r,U}$	Universal reduced energy	
η	Displacement efficiency	
θ	Projectile scattering angle	°
θ_{inc}	Incidence angle	°
$\bar{\Theta}_D$	Mean deposited energy in a thermal spike	eV
λ	Wavelength	nm
λ_d	Displacement mean free path length	cm
λ_{tr}	Mean free transport path length	cm
Λ	Collisional parameter	
π	Mathematical constant	
ρ	Physical density	g cm^{-3}
σ	Cross section	barn [b]
σ_d	Displacement cross section	barn
Σ	Macroscopic cross section	cm^{-1}
Σ_a	Macroscopic absorption cross section	cm^{-1}
Σ_s	Macroscopic scattering cross section	cm^{-1}
Σ_{tr}	Macroscopic transport cross section	cm^{-1}
τ	Lifetime of the collisional phase	s
τ_{min}	Minimum expected target lifetime	a
$\nu(E)$	Nuclear energy loss	eV
ξ	Average logarithmic energy decrement	

[a] 1 eV= $1.602 \cdot 10^{-19}$ J

[b] 1 barn= $10^{-24} cm^2$

ξ_L	Lindhard partition function	
ϕ	Particle flux	$cm^{-2}\ s^{-1}$
ϕ	Target atom scattering angle	$^\circ$
Φ	Particle fluence	cm^{-2}
A	Mass number	
A_1	Projectile mass number	
A_2	Target mass number	
A_s	Screening parameter	
b	Impact parameter	
c	Speed of light	$m\ s^{-1}$
C	Concentration	
C_p	Specific heat capacity	$J\ kg^{-1}\ K^{-1}$
C_{TF}	Thomas-Fermi model constant	
d	Thickness	cm
D	Diffusion coefficient	$cm^2\ s^{-1}$
D_T	Thermal diffusivity	$cm^2\ s^{-1}$
e	Elementary charge	C
E	Energy	eV
E_c	Electronic stopping cutoff energy	eV
E_d	Threshold displacement energy	eV
E_D	Cascade energy	eV
E_{kin}	Kinetic energy	eV
$E_{kin}(PKA)$	PKA kinetic energy	eV
$(E_K)_i$	Projectile kinetic energy	eV
E_{max}	Maximum particle energy	eV
E_{min}	Minimum particle energy	eV
E^*	Critical energy for displacement spikes	eV
f	Thomas-Fermi scattering function	
F_L	Constant	
g	Constant	
J	Flux	$cm^{-2}\ s^{-1}$
k_B	Boltzmann's constant	$J\ K^{-1}$
k_T	Thermal conductivity	$W\ m^{-1}\ K^{-1}$
m_1	Projectile mass	kg
m_2	Target atom mass	kg
M	Atomic weight	$g\ mol^{-1}$
n_a	Atomic density	$atoms\ cm^{-3}$
N	Number density	$atoms\ cm^{-3}$
N_{Av}	Avogadro constant	mol^{-1}
$N_{d,NIEL}$	NIEL predicted defect number	dpa
$N_{d,KP}$	KP model predicted defect number	dpa
$N_{d,NRT}$	NRT model predicted defect number	dpa
N_F	Number of Frenkel pairs after KP model	

N_{NRT}	NRT model predicted defect number	dpa
p_i	Projectile momentum	kg m s^{-1}
P_d	Atomic displacement probability	
r	Radius	cm
R	Total ion range	cm
R_d	Displacement rate	dpa s^{-1}
S	Total stopping power	MeV cm^{-1}
S_n	Nuclear stopping power	MeV cm^{-1}
t	Time	s
t_c	Collisional parameter	
t_i	Irradiation time	s
t_q	Quenching time	s
T	Kinetic energy	eV
T_d	Damage energy	eV
T_i	Kinetic energy of the ith particle	eV
T_K	Temperature	K
T_i^{max}	Maximum kinetic energy of the ith particle	
T_{max}	Maximum possible energy transfer	eV
U_a	Energy per atom	eV
v	Velocity	m s^{-1}
v_p	Proton velocity	m s^{-1}
V	Volume	cm^3
Z	Atomic number	
Z_1	Projectile atomic number	
Z_2	Target atomic number	

1. Introduction

As a neutral particle, the neutron does not carry an electric charge and hence remains insensitive towards the electromagnetic force in contrast to charged particles and exhibits astonishingly unique properties. Since the corresponding wave length λ of neutrons according to the wave-particle duality originally proposed by Albert Einstein and Louis de Broglie is comparable to the interatomic distances present within condensed matter (0.1 Å to 1000 Å [1, 2]), it is undisputed that neutrons are an invaluable tool as an ideal probe of atomic and molecular structures such as the nuclear spin order for example. Coupled with their high penetration depth, this gives neutrons rise to highly qualified tasks under extreme conditions of pressure, temperature, magnetic fields or other external influences. Therefore, after its discovery by James Chadwick in 1932, it is not surprising that these fascinating particles have been continuously used to advance our human knowledge and understanding of fundamental principles of condensed matter in neutron scattering experiments but also to enrich and propel our standard of life and technology in a diverse variety of other disciplines such as biology, chemistry, particle physics, engineering and medicine [3–8].

In principle, the following methods exist to produce neutrons with useful yields [9, 10] in an industrial scale; **(i)** *fission reactions* in nuclear reactors, **(ii)** *spallation reactions* of heavy metals (e.g. Hg, W, Pb, Ta) with energies up to $\sim$ 1 GeV and **(iii)** *low energy reactions* ($\sim$ 10 - 100 MeV[1]) of protons or deuterons with light targets (e.g. Li, Be).

In nuclear reactors **(i)** *fission reactions*, mostly of enriched uranium (increased isotopic ratio of ^{235}U/^{238}U, usually 2.5% to 5% for commercial power plants [13]) as fuel material, are used to sustain a chain reaction, releasing $\sim$ 200 MeV of thermal energy and roughly 2.5 neutrons (prompt and delayed) per fission event in the fissile ^{235}U isotope [14]. Although strategies for the nuclear waste management exist [15], disposal and treatment of the long-lived waste is still subject to intense debates and of great public concern. Accordingly, a transition towards alternative production methods could be observed over the last years.

[1] The threshold energy for spallation reactions is located at $\sim$ 100 MeV [11, 12].

Especially in Germany, this situation got reinforced with the governmental's decision about the exit from nuclear power in June 2011, leaving a gap in the supply of neutrons.

Accelerator-driven neutron sources (ADNS) are a promising alternative and are expected to secure the availability of neutrons for both research and industrial applications. Yet, most of these sources (e.g. SNS, ISIS TS2, JPARC, ESS) are based on endothermic **(ii)** *spallation reactions* [11, 12], mostly induced by protons in the energy regime of GeV [9, 16]. With $\sim$ 20 to 30 neutrons per incident beam particle [17] the neutron yield is much higher than in the case of low energy reactions, but is at cost of the required shielding extent and produced waste.

In case of **(iii)** *low energy reactions* one can keep the Target-Moderator-Reflector assembly (TMR) very compact compared to large spallation facilities, acknowledged with the term compact accelerator based neutron source (CANS) [10]. Besides their physical compactness, in contrast to nuclear reactors CANS benefit from; a greater public acceptance, lower regulatory requirements and building at reasonable costs. Also, the pulsed nature of CANS facilities allows a perfect adjustment of time-dependent neutronics such as the Time-of-Flight principle (ToF) to the individual scattering experimental stations [10].

Since neutron scattering has become such a powerful and popular standard tool over the years and neutrons keep "publishing" well all over the world [18], the demand for neutron beam time is expected to rise in the near future. As large spallation facilities like the ESS in Lund (Sweden) cannot meet that demand alone, worldwide a trend towards neutron provision via CANS can be observed, accelerated by the foundation of the Union for Compact Accelerator-driven Neutron Sources (UCANS) in 2010, aiming to support the ongoing development around the world and to allow scientific exchange [19].

1.1 High Brilliance Neutron Source project (HBS)

Regarding the current development of accelerator based neutron sources, an expected increase in the demand of neutron beam times and the precarious situation in relation to nuclear reactors in Germany mentioned before, the Jülich Centre for Neutron Science (JCNS) aims to construct a medium-flux CANS in the frame of the so called High Brilliance Neutron Source project (HBS) [20–25]. The possible future layout of this facility is depicted in figure 1.1, important accelerator related parameters are given in appendix A.1 and the conceptual design report (CDR) [26]. The project aims for a cost-efficient, competitive and scalable source with a maximized brilliance of neutron beams and shall be used for a multitude of different neutron scattering experiments on small samples.

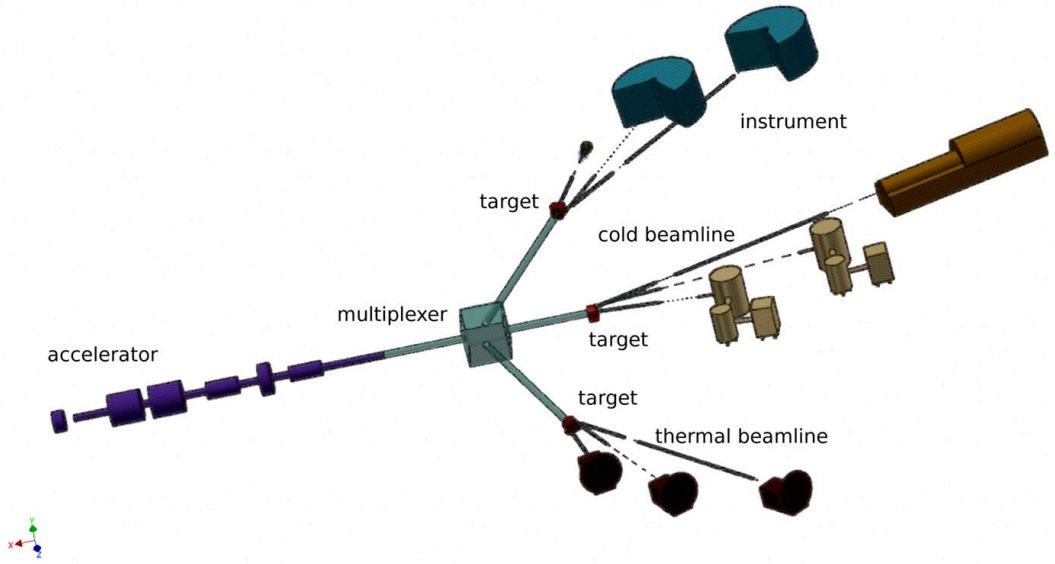

Figure 1.1: Schematic layout of the HBS. A linear accelerator (LINAC) will accelerate protons up to 70 MeV, a multiplexer (magnet) will then deflect the beam into equal parts with different pulse sequences to three different target stations. Every target experiences the same beam power of 100 kW and the neutrons are thermalized to different energies which meet the requirements of the individual instruments. [21]

Generally, accelerator targets have to withstand extreme conditions and keep their mechanical integrity, especially during long-term irradiation. Consequently, a wise choice of the target material is made based on a reduction of radiation damage and a simultaneous maximization of the neutron yield.
Based on the considerations above, **tantalum** (Z=73) was chosen to be the superior choice as target material for the HBS due to the following reasons; *remarkable corrosion resistance* in contact with water and under irradiation, *high melting point* (2996°C [27]), *high thermal conductivity* (57.55 W/m/K at 20°C [27]), *high hydrogen solubility* (0.76 H/Ta at 100°C and 1 atm [28]) and a *high blistering threshold* ($>$ 230E+22 m^{-2} [29]). These properties are in fair balance with the neutron ^{181}Ta(p,xn)W reaction yield of 9.1E+14 s^{-1} mA^{-1} ($\sim$ 0.15 n/p) estimated with the Monte Carlo N-Particle Transport (MCNP) code[2].

1.2 Radiation damage in accelerator environments

Particle accelerators are surrounded by strong and intense radiation fields of a diverse multitude of different particles such as protons, heavy and light ions, neutrons, photons or even more "exotic" particles namely muons, pions or neutrinos. Massive shielding made of a thick concrete wall with highly specific compositions in order to efficiently stop the different particles, is used to envelop the whole infrastructure with the aim to prevent leakage of radiation capable to harm human beings around.

[2]Numerical studies were conducted with a 5.07 mm thick target, 70 MeV proton energy and the TENDL 2017 database for proton reaction cross sections [26].

Components encased within the shielding block are made of special materials designed with a state of the art philosophy to withstand extreme conditions and to ensure a safe operation. However, since the radiation interacts with every kind of matter present in this environment, the materials will suffer damage. Not only the target but every part such as collimators, moderators, reflectors, beam dumps (see fig. 2.1), magnets and so on will be affected by the radiation. The radiation alters the structure of the materials on atomic scale and then change their properties first on a microscopic level before macroscopic changes become visible. Detrimental changes ultimately destroy a material and hence prevent any further use of it.

The operation of an accelerator is always preceded by a licensing process, in which one has to prove a safe operation posing no health risk to any one. In any accelerator facility the target represents the most endangered and critical entity due to its direct exposure to the primary ion beam. When a target suffers substantial damage, its mechanical integrity is at risk and hence it becomes unsafe.
A **target's lifetime** is predominantly limited by; **(i)** the *activation of the material* (i.e. transmutation of non-radioactive into radioactive material), the **(ii)** *thermodynamical target degradation* (i.e. through excessive heat production) and the **(iii)** ***radiation induced material damage***.

With regard to radiation protection laws, the **(i)** *activation of the material* can be studied very precisely with simulation tools and experiments and thus represents no special problem [30]. The process of **(ii)** *thermodynamical target degradation* can be counteracted and slowed down with an efficient heat removal.

The **(iii)** *radiation induced material damage* however, mainly emerging from **atomic displacements**, can show very diverse patterns (see chap. 2) and represents the bottleneck. Although extensive research is observed in this field, already originating in the mid-20th century with embrittlement investigations of reactor pressure vessels (RPVs) [31–36], still many unknowns remain and the estimation of radiation damage is anything but trivial. Since nuclear scientists are currently trying to increase maximum possible ion energies and beam currents and CANS enjoy growing popularity, the analysis of radiation damage has gained essential key importance.

Since experiments either exhibit great challenges with respect to radiation safety aspects (material activation) or are simply not feasible yet from the technology and physics point of view, one mostly has to rely on the outcome proposed by theoretical means. Strong tools such as molecular dynamics (MD) simulations or Monte Carlo (MC) based simulation softwares are able to depict the damage in a highly precise and realistic manner [37–40]. Though tantalum was studied extensively in the past [41], a comparison with the literature is difficult, since the expected damage strongly depends on the framework conditions such as irradiation time or temperature [42]. Consequently, an extensive radiation damage analysis becomes indispensable.

Matching the demand of neutron beam time to proceed in science is only possible if estimations about the expected damage and our current picture of the ongoing processes gain reliability. For the sake of authentic predictions for the radiation response of target and structural materials, the RaDIATE collaboration (Radiation Damage In Accelerator Target Environments) was founded in 2012, with currently 14 institutions worldwide participating [43].

1.3 Thesis goal and reader trajectory

Within this thesis, the expected radiation damage in the tantalum target of the HBS project gets investigated for the first time and the begin of an extensive damage analysis is initiated. Therefore, the extent of atomic displacements in the target as a standard indicator for radiation damage in materials will be examined with strong MC programs, namely FLUKA and SRIM. FLUKA simulations, making the main part of the simulative work, focus on the neutron damage. As a result of all simulations, at least a rough and qualitative estimation about the target's expected lifetime is drawn.

In order to achieve this ambitious goal, chapter 2 first of all introduces the required physics background and fundamental concepts necessary to understand radiation damage in all of its facets. Owing an intense prior literature research, the theory is presented in a broad and detailed manner, though references to the literature are given at certain points to keep that part as compact as possible.

In chapter 3 the methods applied, i.e. the used simulation softwares, are presented. Characteristics of the different codes, especially the way of the obtainment of damage values with regard to physical models given in chapter 2 and set parameters as well as used geometries, are presented.

Chapter 4 presents the results of all simulations in the form of plots and first comments are done.

In chapter 5 the results of the simulations will be discussed in detail and compared to each other. Numerical results are given and a final damage assessment including a qualitative estimation of the target's lifetime is done based on a broad and meticulous literature review.

Finally, chapter 6 will draw a general conclusion and end the thesis. The results are expected to be useful also for other similar CANS projects and the nuclear community in general shall benefit from the thesis outcomes.

2. Radiation induced material damage physics

Radiation induced material damage plays a crucial role in virtually every type of nuclear facilities and due to its inherent nature it is present wherever nuclear materials or technology are used [44–46]. Irrespective of the area of application of ionizing radiation, in the vast majority radiation induced material damage represents a dominant bottleneck, which physically limits the efficiency (i.e. gained physics/cost) and impairs a safe and economic operation.

For a maximized benefit and also a proper justification of a meaningful use of nuclear applications it is essential to understand the underlying physics and mechanisms of the damage creation and its further evolution over time. Only if these complex processes behind are recognized in their complete extent, useful measures, such as for a prolongation of an accelerator target's lifetime, can be taken.

Therefore, this chapter intends to describe fundamental physics, mechanisms and methods (MC) required for a proper understanding of radiation damage. The considerations focus on the damage creation and evolution due to atomic displacements, as the major damage mechanism in metals such as tantalum.

2.1 Diverse nature of radiation damage patterns

Energetic particles (i.e. $E_{kin} > 1$ eV) such as originating from our universe or any kind of human built nuclear facility are capable to alter the micro- and macroscopic structure of matter [39]. Although these changes might also have beneficial influences, detrimental ones usually dominate, justifying the impact of ionizing radiation on materials to be referred as "radiation damage" [47].

Though the actual damage pattern in its details might vary depending on the material type, one can observe common damage mechanisms, finding their origin in the following compilation of radiation effects [48] that may depend in a synergetic manner on each other; **(i)** *thermal heating*, **(ii)** *production of impurities*, **(iii)** *ionization*, **(iv)** *blister formation* and **(v)** ***atomic displacements***.

So, generally the interaction of radiation with matter can lead to the production of phonons (lattice vibrations), excitons, plasmons, secondary electrons and photons, resulting in a **(i)** *heating* of the material due to energy release.

When material atoms are transmuted into other atoms via nuclear reactions (especially such induced by neutrons), stable or radioactive **(ii)** *impurities* are created, that may affect the material performance.

During the electronic stopping of radiation in matter, **(iii)** *ionization* processes eject electrons from atoms, leaving charged ions behind that are highly reactive and hence might alter the chemical composition of the material.

Ions traversing a metal can catch missing electrons from the electron cloud in the conduction band and recombine to their neutral atom counterpart. The local accumulation of these neutral atoms leads to a grain boundary embrittlement and accelerated swelling, resulting in an increased pressure [49]. The swelling might cause cracks, known as **(iv)** *blistering* (see fig. 2.1) if this process occurs near the surface, since formed gas bubbles can be seen with the bare eye. Hydrogen and helium (mainly via (n,α)-reactions) blistering is of major concern in accelerator targets [50–52], and can limit the target's lifetime substantially [53].

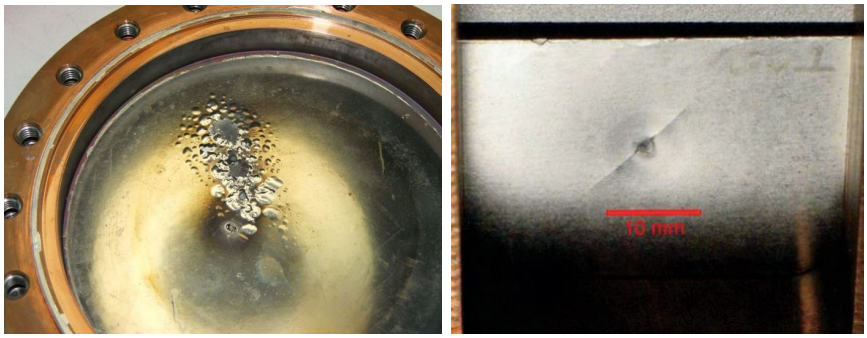

Figure 2.1: Radiation damage in accelerator environments. Left: Radiation induced blister formation in a tungsten beam dump of 40 cm diameter from the Soreq Applied Research Accelerator Facility (SARAF) in Yavne, Israel. The damage occured several minutes after irradiation by 4 MeV protons at a beam current of 6E+15 protons/sec. [51] Right: Cracking of a 0.03 cm thick tungsten target after irradiation with 5.77E+16 $^{76}Ge^{30+}$ ions at the National Superconducting Cyclotron Laboratory (NSCL). The crack was induced by swelling and embrittlement. [12, 54]

In solids however, the damage is mainly on account of lattice defects in the crystal, which arise through the **(v)** *displacement of atoms* in atomic collisions. Atoms struck at the surface can leave the material, which is known as sputtering [55]. In the bulk of a material, these point defects (PDs) can then migrate and cluster to form more complex damage patterns like e.g. dislocation loops [56], adatoms [57] or craters [58] on surfaces, empty regions [59] or over- or undercoordinated atoms [60] (see also fig. 2.2).

All these processes **(i)** to **(v)** ultimately affect virtually all materials' properties, but mainly [12]; *mechanical* (e.g. radiation hardening, embrittlement, ductility, irradiation creep, void swelling, fatigue performance), *thermal* (e.g. conductivity, resistivity) and *electrical* (e.g. conductivity, resistivity) ones. Beneficial changes like a radiation hardening (i.e. increased yield strength) may be accompanied by negative changes such as embrittlement, a decrease in ductility.

Damage patterns in crystal lattices

Understanding the nature of radiation damage on the atomic level is indispensable to recognize macroscopic effects of ionizing radiation on materials. In metallic crystals (e.g. tantalum), defects can be classified into four categories [55, 61–63]; **(i)** 0-dimensional *point defects* (PDs; vacancies, interstitials, substitutional atoms), **(ii)** 1-dimensional *line defects* (dislocation lines, e.g. edge and screw dislocations), **(iii)** 2-dimensional *planar (surface) defects* (dislocation loops, grain and phase boundaries, twins) and **(iv)** 3-dimensional *volume defects* (voids, bubbles, precipitates, amorphous phases and stacking-fault tetrahedras).
The most basic defects are depicted in figure 2.2 for a single crystal.

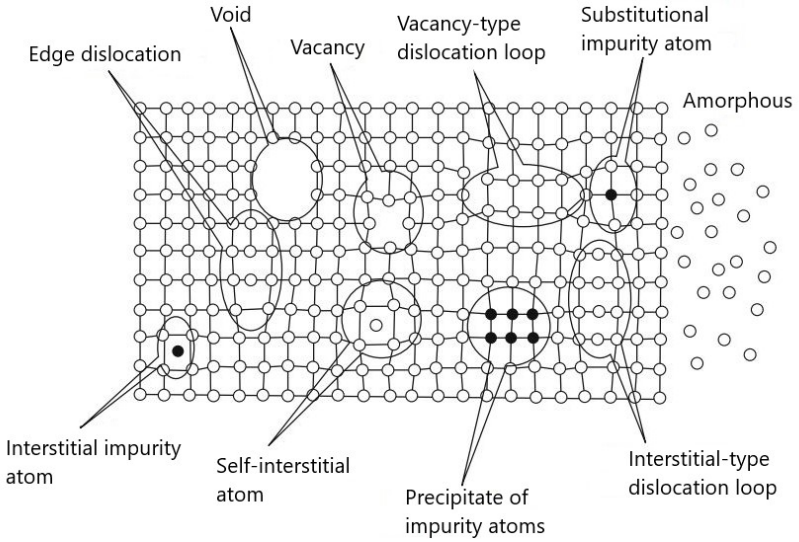

Figure 2.2: Most important defects in a single crystal lattice structure. PDs are the starting point for the evolution of complex defects. [64]

Complicated defects originate from simple and 0-dimensional **(i)** *point defects* (PDs), omnipresent due to crystallographic imperfections. The most fundamental PDs are vacancies and interstitials, i.e. empty lattice sites and atoms located in a crystal position other than a regular site [61, 65, 66]. If a radiation induced vacancy and the corresponding interstitial are in close proximity to each other, the resulting defect is called Frenkel pair (FP). PDs give rise to atomic mixing, for monoatomic materials like tantalum however not posing a significant risk.

As **(ii)** 1-dimensional *line defects* dislocation lines are disturbances (vacancies, interstitials) of the crystal lattice along a fictive line (dislocation line) [63].

In the case of dislocation loops as **(iii)** 2-dimensional *planar (surface) defects*, simply a part of a lattice plane is either missing (matter deficit, vacancy type) or has been added (matter excess, interstitial type) [65].

The clustering of vacancy-type dislocation loops leads to the agglomeration of vacancies, finally resulting in a **(iv)** 3-dimensional *volume defect* of a void, regions characterized by low densities and hence favored for the aggregation of gases and bubbles (e.g. hydrogen and helium accumulation during irradiation).

2.2 The displacements per atom (dpa) concept

In an atomic displacement, a stationary lattice atom receives an energy transfer high enough to overcome binding energies and leave the lattice site (see fig. 2.3). Produced FPs represent stable defects only if they are not too close to each other (i.e. distance > 2 nm to prevent spontaneous defect recombination).

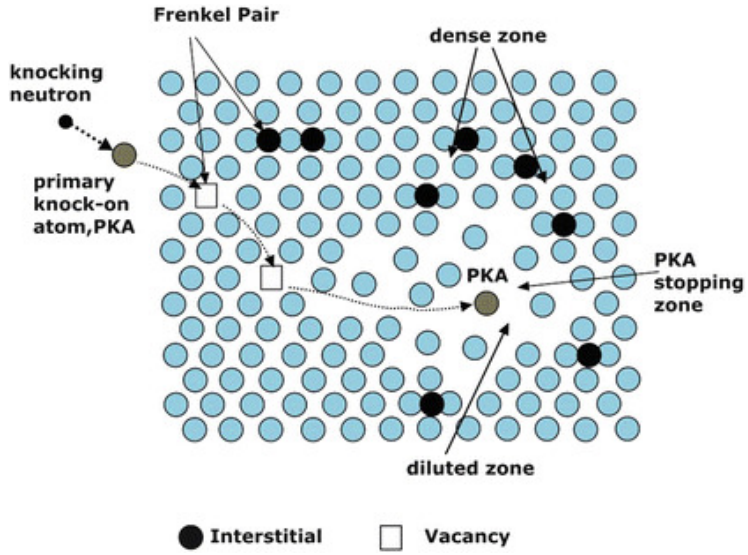

Figure 2.3: Displacement of atoms in a crystal lattice. An incident particle (neutron) kicks an atom out of its equilibrium lattice position. This primary knock-on atom (PKA) further ejects atoms during its thermalization. FPs represent stable defects. [36]

The extent of atomic displacements is expressed in terms of *displacements per atom (dpa)*, a physical unitless quantity defined as [67]:

$$dpa \;=\; displacements\,per\,atom \;=\; \frac{\#\,displaced\,atoms\,in\,volume\,V}{\#\,material\,atoms\,in\,volume\,V} \qquad \text{(Eq. 2.1)}$$

As atomic displacements arise as a result of nuclear collisions, there is a clear connection to a cross section σ [33, 67–69]:

$$dpa = \int_0^{t_i} dt \int_{E_{min}}^{E_{max}} \sigma_d(E)\,\phi(E,t)\,dE \qquad \text{(Eq. 2.2)}$$

where $\phi(E,t)$ is the energy and time dependent particle flux, $\sigma_d(E)$ the displacement cross section as a function of energy E, t_i the irradiation time, E_{min} the minimum and E_{max} the maximum particle energy respectively.
Based on the Norget-Robinson-Torrens (NRT) formalism (see chap. 2.5), the *displacement cross section* σ_d can be computed as [69]:

$$\sigma_d = \sum_i \int_{E_d}^{T_i^{max}} \frac{d\sigma}{dT_i} \eta\, N_{NRT}\,(T_i)\,dT_i \qquad \text{(Eq. 2.3)}$$

with E_d as the threshold displacement energy (TDE), $d\sigma/dT_i$ as the recoil atom energy distribution, T as the kinetic energy of the ith particle, T_i^{max} as the maximum energy, η as the displacement efficiency and N_{NRT} as the number of produced PDs (i.e. FPs). It must be noted that $E_{min} = E_d$ in equation 2.2.

Threshold displacement energy (TDE)

The threshold displacement energy (TDE) is the most fundamental parameter required for a successful radiation damage assessment, particularly in the dpa concept. As a key ingredient in every single present dpa model, its precision crucially determines the accuracy of simulative and experimental outcomes and hence the quality of depicting radiation damage.

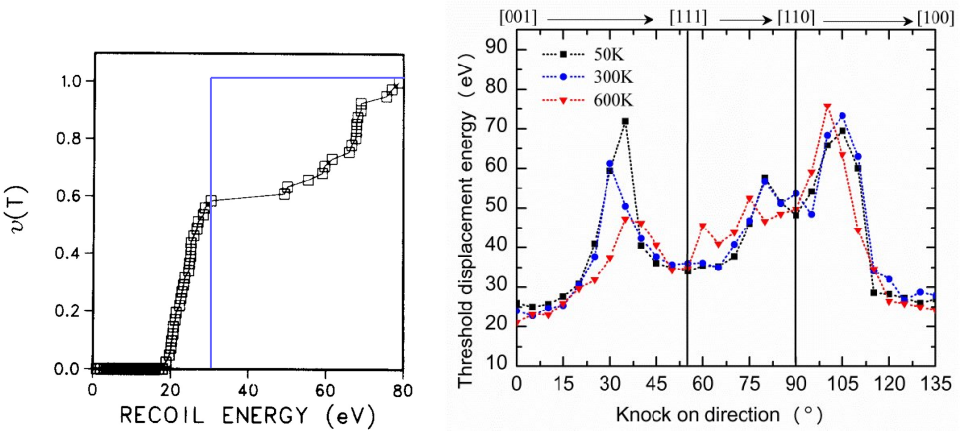

Figure 2.4: Dependencies of the threshold displacement energy (TDE). Left: Damage function (probability for a displacement) for polycrystalline Cu with different recoil atom energies (averaged over 40 collision directions). The step function in blue depicts the accepeted average value for Cu of 30 eV. [39] Right: Variation of the threshold displacement energy for Nb with different crystallographic PKA knock-on directions and temperatures. [70]

In principle, the TDE is defined as the minimum amount of energy ($\sim$ 10 - 100 eV for most metals [67]) a projectile has to transfer to a material atom to leave its initial lattice site and create a stable defect (i.e. FP). Spontaneous defect recombination processes can appear even at cryogenic temperatures ($\sim$ 0 K to 123 K [71, 72]), with a spontaneous recombination distance of $\sim$ 0.5-2 nm [73–76]. Though the TDE is a material property, unique and sharp values do not exist since it exhibits a tremendously non-trivial behavior, most notably due to crystallographic effects, temperature and strain [39, 77].

Owing to the anisotropy of crystal structures the TDE value varies with the crystal direction, being lower for low-index (e.g. <111> in FCC metals) than high-index directions [67]. Higher temperatures generally increase the damage probability [78–80], which however still depends on the material [81], externally applied strain is observed to lower TDE values [77].

Though the defect production probability in principle follows no discrete relationship [82], for the sake of simplification the *probability for a displacement event* $P_d(E)$ is usually described by a simple step function [83, 84]:

$$P_d(E) = \begin{cases} 0 & \text{if } E < E_d \\ 1 & \text{if } E \geq E_d \end{cases} \qquad \text{(Eq. 2.4)}$$

with E as the particle's actual energy and E_d as the threshold displacement energy. The latter one is obtained either experimentally via electron irradiation and high-voltage electron microscopy [77, 85–88], or theoretically via MD simulations that rely on databases of realistic interatomic potentials [70]. Averaged values are generally well justified since one has to deal with a huge number of displacements usually (statistics) [89].

2.3 Collision cascade

A particle traversing matter generates a huge diversity of particles by interactions, forming a cascade of displacements (i.e. collision cascade, see fig. 2.5). If that particle is a hadron (i.e. proton, neutron), the term hadronic collision cascade is used. Depending on the time scale, damage production mechanisms are divided into two mechanisms; the *primary damage* ($\sim$ 10 ps) and the *long-time scale damage evolution* induced by thermally activated processes ($\sim$ nanoseconds to years) [39]. A more precise description of the cascade development over time classifies four stages; **(i)** the *collisional phase* (until $E_{kin}(PKA) < E_d$, duration < 1 ps), the **(ii)** *thermal spike* (creation $\sim$ 1 ps after end of collisional phase), the **(iii)** *quenching* ($\sim$ 10 ps) and the **(iv)** *defect annealing* (up to years).

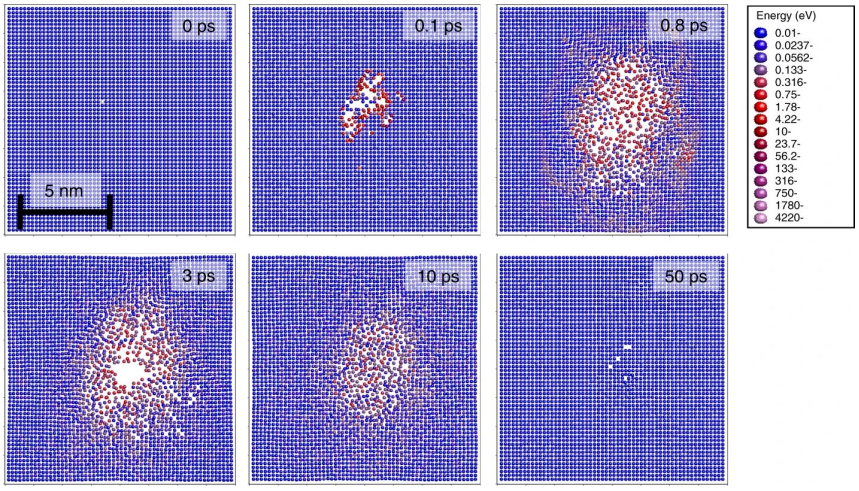

Figure 2.5: Molecular dynamics (MD) simulation of a collision cascade initiated by a 10 keV PKA in Au. Circles represent individual atoms of different kinetic energies according to the energy scale on the right. In the early phase of the cascade, many atoms are displaced. In the final stage however, most of them occupy perfect lattice sites again. [90]

The *lifetime* τ of the **(i)** *collisional* (ballistic) phase can also be determined in a computational way [61]:

$$\tau = \frac{1}{4\,D_T}\left(\frac{3\,E_D}{4\,\pi\,n_a\,U_a}\right)^{\frac{2}{3}} \qquad \text{(Eq. 2.5)}$$

where D_T is the thermal diffusivity of target atoms ($D_T = k_T/C_p$, with k_T as thermal conductivity and C_p as specific heat capacity), n_a the atomic density, U_a the energy per atom that might be estimated by the material's melting temperature [61] and E_D the available damage energy in the cascade. Typical values for τ of $\sim$ 1 ps fit to a few vibrations of the crystal lattice.

Depending on the time scale and physical dimension of the damage in the cascade, different simulation methodologies are used for investigations (see fig. 2.6).

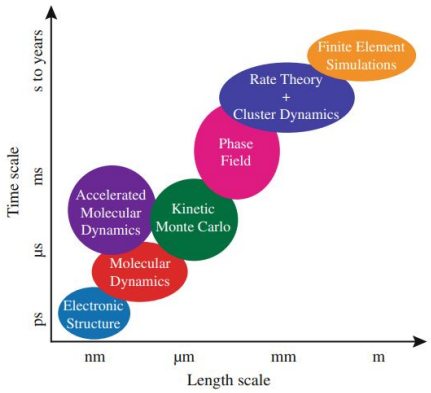

Figure 2.6: Simulation methodologies for radiation damage in dependence of the time and length scale. [61]

Spike concepts

The concept of spikes is substantial in the analysis of cascades as ongoing processes crucially influence the remaining defects and their possible evolution over time, especially in heavy and dense materials [91, 92] as Ta. Although different definitions and types exist [91], it is most common to define a spike as "a high density cascade that possesses a limited volume in which the majority of atoms are temporarily in motion" (from [55] and after; Seitz and Koehler 1956, Sigmund 1974). A **(ii)** *thermal spike* is usually preceded by a *displacement spike*.

Brinkman firstly introduced the concept of *displacement spikes* (see fig. 2.7) [93, 94], proposing a net outward motion of lattice atoms along the trajectory of traversing ions when the average distance between displacement collisions comes closer to interatomic distances [91]. A vacancy rich core (termed "depleted zone" by Seeger [95]) enveloped with interstitial atoms is formed.

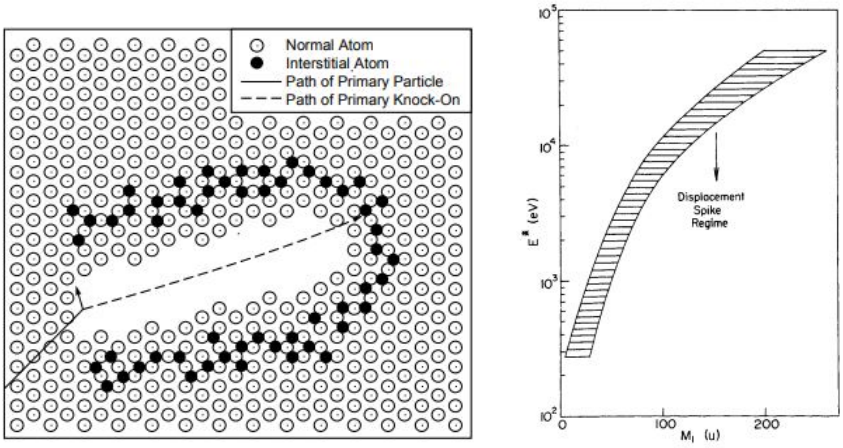

Figure 2.7: Concept of displacement spikes. Left: The incident ion pushes all atoms along its trajectory to the outside, leaving a vacancy rich core surrounded by a shell of interstitial atoms behind. [55] Right: Critical energy E^* for the creation of displacement spikes as a function of the ion's mass in u. [91]

A short distance between the PKA's atomic collisions (i.e. displacements) during its thermalization favors displacement spikes. This is quantified by the *mean free path length* λ_d, defined as the inverse of the macroscopic cross section $\Sigma(E)$:

$$\lambda_d = \frac{1}{n_a\,\sigma(E)} = \frac{1}{\Sigma(E)} \qquad \text{(Eq. 2.6)}$$

Knowing the total ion range $R(E)$ and its velocity v allows to approximate the time t it takes a displacement spike to form [55]:

$$t \approx \frac{R(E)}{\frac{1}{2}\,v} \qquad \text{(Eq. 2.7)}$$

If the energy of displaced atoms falls below the TDE value, subthreshold energy transfers are distributed in low-energy many-body atomic collisions as heat (i.e. lattice vibrations) [55, 92] - a **(ii)** *thermal spike* is born. As the vibrational energy resembles a Maxwell-Boltzmann function [55, 91], local heating and melting starts to play a role, and the *mean deposited energy* $\bar{\Theta}_D$ in the spike is given as:

$$\bar{\Theta}_D = \frac{3}{2} k_B T_K \qquad \text{(Eq. 2.8)}$$

where k_B is Boltzmann's constant and T_K the temperature. Temperatures of up to 10.000 K might be reached for a short time within the spike [96], justifying a treatment of atoms as a classical liquid [92]. These high temperatures are able to cause local melting and related phase transitions in the crystal structure [97].

The time it takes a **(ii)** *thermal spike* to get rid of all the vibrational energy is called the *quench time* t_q. Assuming the spike to be circular shaped with a radius r, one can estimate that **(iii)** *quenching* time in first approximation as [55]:

$$t_q = \frac{r^2}{4\, D_T} \qquad \text{(Eq. 2.9)}$$

Defect migration and annealing

The cooling down of a thermal spike (i.e. quenching stage) can be treated as a rapid recrystallization process [39], during which defects produced in the collisional phase recombine, resulting in a number of displaced atoms smaller than predicted by many physical models (e.g. NRT model [39]). These recombination processes are termed as "athermal" since thermally activated processes play no role, the subsequent relaxation processes are called **(iv)** *defect annealing*. Though most defects are immobile at temperatures below 10 K, for a proper long-term damage assessment one should consider migration effects since exposure temperatures are usually much greater [67].

Considered as diffusion processes driven by concentration gradients and ambient influences (e.g. temperature), the migration of defects can be described with *Fick's first and second law* (eq. 2.10 and eq. 2.11) in one dimension [55, 61]:

$$J = -D \nabla C = -D \frac{\partial C}{\partial x} \qquad \text{(Eq. 2.10)}$$

$$\frac{\partial C}{\partial t} = -\nabla J = -\nabla D \nabla C = -\frac{\partial}{\partial x}\left(D \frac{\partial C}{\partial x}\right) \qquad \text{(Eq. 2.11)}$$

where J is the flux, $\partial C/\partial x$ the conentration gradient and D the diffusion coefficient.

In metals (e.g. tantalum) a trend of increased defect recombination at elevated temperatures can be observed and defect structures already present before irradiation may be "annealed" if interstitial atoms move inside the hot liquid core of thermal spikes to recombine with radiation induced vacancies [98].

2.4 Physics of the displacement process

This section intends to provide the nuclear physics background knowledge, required to understand the origin of atomic displacements.
As the kinetic energy of protons in the HBS project with 70 MeV is too high to justify a sole treatment with classical physics ($v_p \approx 0.386\,c > 0.1\,c$), additionally relativistic considerations are done.

Collision kinematics

PKAs are born in atomic displacements, mainly via elastic collisions (see fig. 2.8). In principle, the more energy an incident particle transfers to a lattice atom (ΔE_K), the greater is the expected radiation damage.

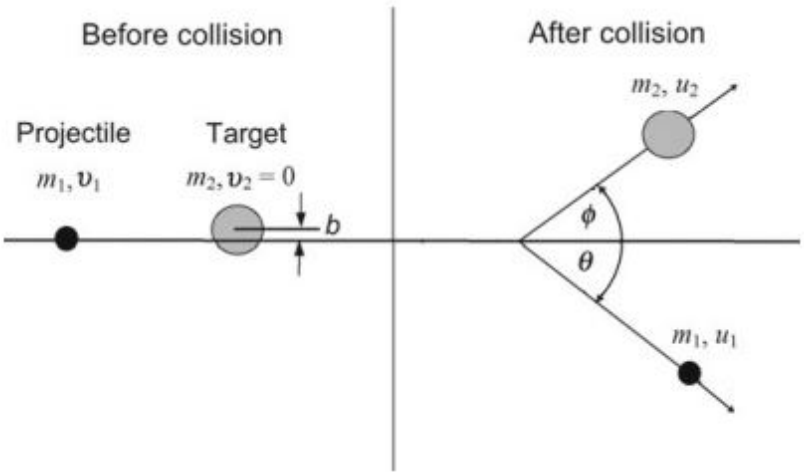

Figure 2.8: Elastic collision between a projectile and a stationary target. A projectile with mass m_1, velocity v_1, momentum p_i and kinetic energy $(E_K)_i$ hits a stationary target of mass m_2 and $v_2 = 0$ at an impact parameter b. The projectile and target leave the interaction place with an angle of θ and ϕ respectively. The projectile moves with the velocity u_1 and the target with the velocity u_2 after the collision. [99]

The energy transfer from the projectile to the target is given by [99]:

$$\Delta E_K = (E_K)_i \frac{4\,m_1\,m_2}{(m_1 + m_2)^2} \cos^2\phi = (E_K)_i\,\Lambda\cos^2\phi \qquad \text{(Eq. 2.12)}$$

Maximum energy transfer occurs in the case of a head-on collision (i.e. $b = 0$, $\phi = 0$ and $\theta \in \{0, \pi\}$) [99]:

$$\Delta E_{max} = \frac{4\, m_1\, m_2}{(m_1 + m_2)^2}\, (E_K)_i \qquad \text{(Eq. 2.13)}$$

If the incident particle approaches relativistic conditions, one has to use [99]:

$$\Delta E_{max} = \frac{2\,(\gamma + 1)\, m_1\, m_2}{m_1^2 + m_2^2 + 2\,\gamma\, m_1\, m_2}\, (E_K)_i \qquad \text{(Eq. 2.14)}$$

$$\gamma = \left(1 - \beta^2\right)^{-\frac{1}{2}} = \left(1 - \left(\frac{v}{c}\right)^2\right)^{-\frac{1}{2}} \qquad \text{(Eq. 2.15)}$$

where v is the projectile's velocity before the collision and c the speed of light. In the case of the HBS project, the maximum energy transfer of relativistic 70 MeV protons to tantalum atoms in a head-on collision is hence ~ 1.60 MeV.

Nuclear stopping power

A particle of initial kinetic energy $(E_K)_i$ loses energy as it traverses matter by interactions with atoms (nuclear stopping, n) and surrounding electrons (electronic stopping, e). The energy loss per unit distance travelled dE/dx, is quantified as the *total stopping power* [55, 100]:

$$-\left(\frac{dE}{dx}\right)_{tot} = \left(\frac{dE}{dx}\right)_e - \left(\frac{dE}{dx}\right)_n \qquad \text{(Eq. 2.16)}$$

As atomic displacements result exclusively due to nuclear deposited energy via elastic collisions [55], assuming non-relativistic conditions, the *universal stopping power for nuclear stopping* can be evaluated based on a Ziegler-Biersack-Littmark (ZBL) universal screened coulomb potential from the Thomas-Fermi model of the atom [101]:

$$-\left(\frac{dE}{dx}\right)_n = n_a \int_0^{T_{max}} \frac{d\,\sigma^U(E,\, T)}{dT}\, T\, dT \qquad \text{(Eq. 2.17)}$$

where $E = (E_K)_i$ is the projectile's kinetic energy, T is the amount of kinetic energy transferred to the recoiling target, T_{max} the maximum possible energy transfer in a non-relativistic approach (see eq. 2.13) and $d\sigma^U(E,\, T)/dT$ the *universal screened Coulomb energy-transfer differential cross section* that can be expressed as [101]:

$$\frac{d\sigma^U(E,\,T)}{dT} \;=\; \left[\frac{\pi\,\alpha_U^2\,\epsilon_{r,U}^2}{T_{max}}\right]\,\frac{f\left(t_c^{\frac{1}{2}}\right)}{2\,t_c^{\frac{3}{2}}} \qquad \text{(Eq. 2.18)}$$

where α_U is the universal screening length, t_c a collisional parameter, $\epsilon_{r,U}$ the universal reduced energy and $f\left(t_c^{\frac{1}{2}}\right)$ the Thomas-Fermi scattering function (e.g. after [102]).

For a unity charge state of protons, one has to replace α_U and $\epsilon_{r,U}$ with the *Thomas-Fermi screening length* and the *Thomas-Fermi reduced energy* respectively [101]:

$$\alpha_{TF} \;=\; \frac{C_{TF}\,\alpha_0}{Z_2^{\frac{1}{3}}} \qquad \text{(Eq. 2.19)}$$

$$\epsilon_{r,TF} \;=\; \frac{\alpha_{TF}}{Z_1\,Z_2\,e^2}\left(\frac{m_2}{m_1\,+\,m_2}\right)(E_K)_i \qquad \text{(Eq. 2.20)}$$

where C_{TF} is a Thomas-Fermi model constant, α_0 the Bohr radius and Z is the atomic number with the indices 1 and 2 referring to the projectile and target.

In relativistic cases, equation 2.17 is valid if the universal screened Coulomb energy-transfer differential cross section $d\sigma^U(T)/dT$ is replaced by the *differential cross section after Wentzel and Molière (WM)* [101]:

$$\frac{d\,\sigma^{WM}(E,\,T)}{dT} \;=\; 2\,\pi\,\left(Z_1\,Z_2\,e^2\right)^2\,\frac{E^2}{p_i^2\,m_2\,c^4}\,\frac{1}{\left[T_{max}\,A_s\,+\,T\right]^2} \qquad \text{(Eq. 2.21)}$$

where A_s represents an additional screening parameter.

Non-Ionizing Energy Loss (NIEL)

A quantity closely related to the dpa concept, is the *non-ionizing energy loss (NIEL)*, defined as the energy lost due to nuclear stopping, the amount of energy responsible for atomic displacements.

The NIEL is obtained via integration of the spectrum of recoil particles $d\,\sigma\,/\,T$ over all recoil energies [102, 103]:

$$NIEL(E) \;=\; n_a\int_0^{\Lambda\,E}\xi_L(T)\,T\left(\frac{d\,\sigma}{dT}\right)_E dT \qquad \text{(Eq. 2.22)}$$

with Λ as given in equation 2.12, $E \;=\; (E_K)_i$ as the projectile's kinetic energy and:

$$\xi_L(T) = \frac{S_n(E)}{S(E)} = \frac{1}{1 + F_L \cdot g(\epsilon_L)} \quad \text{(Eq. 2.23)}$$

$$g(\epsilon_L) = \left(3.4008 \cdot \epsilon_L^{\frac{1}{6}} + 0.40244 \cdot \epsilon_L^{\frac{3}{4}} + \epsilon_L\right) \quad \text{(Eq. 2.24)}$$

$$F_L = 30.724 \cdot Z_1 \cdot Z_2 \sqrt{Z_1^{\frac{2}{3}} + Z_2^{\frac{2}{3}}} \quad \text{(Eq. 2.25)}$$

$$\epsilon_L = \frac{E}{0.0793 \cdot \frac{Z_1^{\frac{2}{3}} \cdot \sqrt{Z_2}}{\left(Z_1^{\frac{2}{3}} + Z_2^{\frac{2}{3}}\right)^{\frac{3}{4}}} \cdot \frac{(A_1 + A_2)^{\frac{3}{2}}}{A_1^{\frac{3}{2}} \sqrt{A_2}}} \quad \text{(Eq. 2.26)}$$

where $\xi_L(T)$ is the *Lindhard partition function*, defined as the ratio of the nuclear stopping power $S_n(E)$ to the total stopping power $S(E)$, F_L is a constant, A the mass number and ϵ_L is the *Lindhard's reduced energy*.
Note that equations 2.24 to 2.26 might be expressed in a different way depending on the used reference. However, as all forms are mathematically identical it will be referred to these equations taken from [101] at certain points.

If one wants to use the NIEL for the calculation of atomic displacements, one has to restrict it in energy, i.e. the *energy restricted RESNIEL* [102, 103]:

$$RESNIEL(E) = n_a \int_{E_d}^{\Lambda E} \xi_L(T)\, T \left(\frac{d\sigma}{dT}\right)_E dT \quad \text{(Eq. 2.27)}$$

Since the NIEL is contained in the formalism of the nuclear stopping power (compare eq. 2.17 with eq. 2.22 and eq. 2.27), the calculation of a relativistic NIEL is in principle possible based on a nuclear stopping power from the differential cross section after Wentzel and Molière (eq. 2.21).

2.5 Physical models

A correct damage assessment, regardless if experimental or theoretical, requires physical models that are capable to depict the ongoing mechanisms as realistic as possible. Hence, carefully considered and useful models are invaluable since they essentially determine the precision of such assessment outcomes.

In detail, the methodology of the Kinchin and Pease (KP) model as a first practical model will be introduced, the enhancements done later in the Norget-Robinson-Torrens (NRT) model as a key and standard tool in the radiation damage analysis are pointed out as well as shortcomings in current models get addressed.

Kinchin and Pease (KP) model

The first accepted model for a simple and useful defect prediction of atomic displacements was suggested in 1955 by Kinchin and Pease (KP) [104]. They introduced a hard-sphere model [55] depending on three parameters; the primary particle (i.e. PKA) kinetic energy E, the threshold displacement energy E_d of the considered material and an energy cutoff E_c.

The whole model is based on the conventional hard-sphere assumptions [55, 61, 84, 105]. Consequently; only collisions between like atoms ($m_1 = m_2$) are considered, the damage cascade is treated as a sequence of elastic two-body collisions, the probability of damage production is discrete (after eq. 2.4), electronic stopping is ignored via a cutoff energy E_c beyond which electronic stopping dominates over nuclear stopping and the crystal structure is ignored.

Based on the mentioned parameters and assumptions, the KP model in its original form can be postulated as:

$$N_{d,KP}(E) = \begin{cases} 0 & \text{for } E < E_d \\ 1 & \text{for } E_d < E < 2\,E_d \\ \frac{E}{2\,E_d} & \text{for } 2\,E_d < E < E_c \\ \frac{E_c}{2\,E_d} & \text{for } E > E_c \end{cases} \qquad \text{(Eq. 2.28)}$$

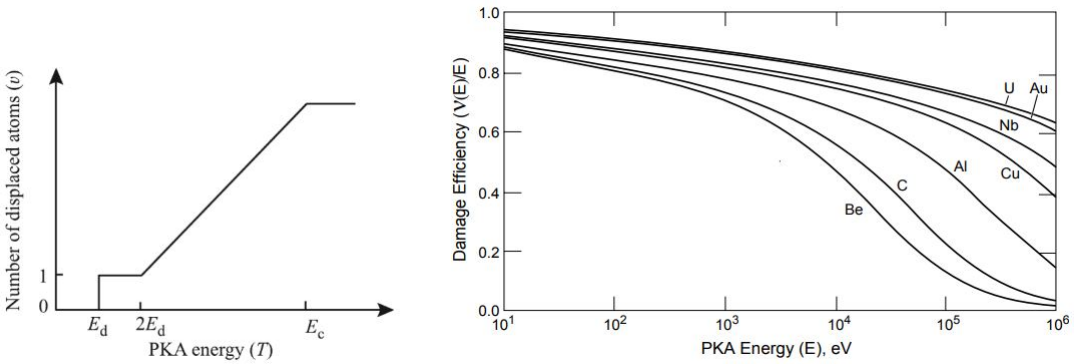

Figure 2.9: Visualization of the KP model and PKA energy losses. Left: Visualization of atom displacements as a function of the PKA energy according to equation 2.28. [55] Right: Ratio of nuclear energy loss $\nu(E)$ to particle energy E for self-ion types. [55]

For particles carrying a kinetic energy higher than E_d but less than the double of it, the number of displacements $N_{d,KP}(E)$ is exactly 1 due to the hard-sphere model [55]. For a kinetic energy between $2\,E_d$ and E_c, the model assumes linearity. Since E_c ensures elastic collisions during the cascade via a discrimination of inelastic, electronic energy losses above that value [106], the displacement probability remains constant beyond E_c.

Figure 2.9 visualizes the KP model and PKA energy losses. It shall emphasize that the concept of E_c is well justified since all materials regardless their atomic number Z show an increase in electronic stopping at higher energies.

Norget-Robinson-Torrens (NRT) model

The Norget-Robinson-Torrens (NRT) model represents a refinement of the KP model and as the current accepted standard model it is also the footing of the "American Society for Testing and Materials" (ASTM) for the estimation of radiation induced damage in iron and steel alloys [107].

Roughly 20 years after the KP model's success Norget, Robinson and Torrens performed binary collision computer simulations with the MARLOW code with realistic interatomic potentials [75, 108], revealing that some vacancies can happen to be refilled. This fact was taken into account by the displacement efficiency η, which was found out to be 0.8.

Also, after Lindhard et al. developed a comprehensive stopping theory [109] it got clear that one has to take only the nuclear deposited energy into account (i.e. NIEL). The complete and refined NRT model can then written to be:

$$N_{d,NRT}(T) = \begin{cases} 0 & \text{for } T_d < E_d \\ 1 & \text{for } E_d < T_d < \frac{2\,E_d}{\eta} \\ \frac{\eta\,T_d}{2\,E_d} & \text{for } \frac{2\,E_d}{\eta} < T_d < \infty \end{cases} \qquad \text{(Eq. 2.29)}$$

The available *damage energy* T_d can then be computed depending on the relation of E and E_d according to Robinson's parametrization of the Lindhard-Scharff-Schiøt (LSS) energy loss partitioning function, after [106, 109]:

$$T_d = \begin{cases} 0 & \text{for } E < E_d \\ \frac{2\,E_d}{\eta} & \text{for } E_d \leq E \leq \frac{2\,E_d}{\eta} = 2.5\,E_d \\ \frac{E}{2\,E_d} & \text{for } 2\,E_d < E < E_c \\ \frac{E}{1+F_L\,g(\epsilon_L)} & \text{for } E > \frac{2\,E_d}{\eta} \end{cases} \qquad \text{(Eq. 2.30)}$$

It must be noted that the NRT model keeps its validity for PKA energies up to $E_{PKA} = 24.9\,A\,Z^{\frac{4}{3}}\,keV$ [110, 111]. As a special case of the LSS theory, equations 2.24 to 2.26 are only applicable to monoatomic materials. If one wants to calculate the damage in a multi-component material, like alloys for example, one has to use an effective value for A and Z and one single value for E_d.

Shortcomings in the KP and NRT model

Both, the KP model as well as the NRT model overestimate the predicted damage. Though the NRT model accounts for electronic stopping in contrast to the KP model, the linearity assumed between the deposited energy and the number of FPs (see fig. 2.9) is not justified for high PKA energies, where cascades become energetically more dense (i.e. thermal spikes) and many-body collisions become important. Experiments revealed the damage efficiency to be in the order of 0.3 instead of 0.8 [112]. Furthermore, for metals exposed to high particle fluences a saturation character of displacements has been observed [113], completely disconnecting the dpa from the prediction by the models.

Though variations of the TDE with different crystallographic directions are accounted for by an averaged value, two other effects might influence the defect production essentially [55, 61]; **(i)** *focusing* and **(ii)** *channeling* (see fig. 2.10).

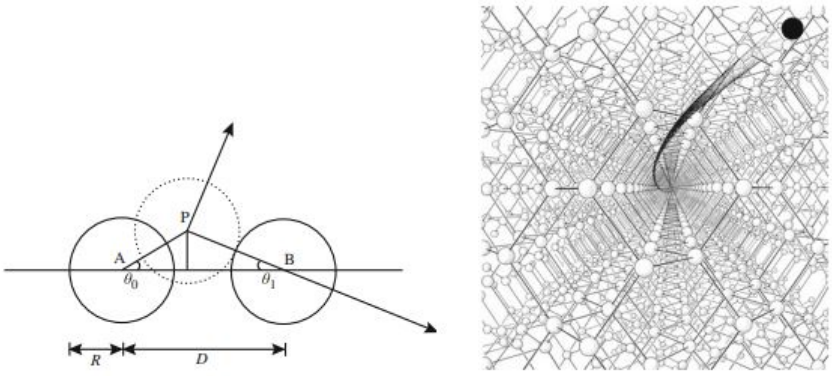

Figure 2.10: Principle of focusing and channeling. Left: In the focusing process an incident particle (A) strikes a stationary lattice atom (B) along the atom row in a close collision. Atom B will repeat that process with the next atom along the row and a "chain reaction" is induced. Focusing results in an increased number of atomic displacements. [61] Right: In the channeling process an ion moves through an atomic row ("channel"). It undergoes only glancing collisions and its energy loss dE/dx is reduced, hence λ_d is increased. [61]

The process of **(i)** *focusing* is defined as an energy transfer by means of near head-on collisions along a row of atoms in a crystal lattice. It will increase the amount of displacements due to a smaller mean free path length λ_d and thus increase the defect number relative to the prediction by the KP and NRT model. The **(ii)** *channeling* is a high energy phenomenon, in which the ion trajectory is aligned along atomic rows ("channels") of a certain crystallographic direction [55]. Channeling reduces the defect number as the ions have a lower energy loss dE/dx (i.e. higher range) and a larger mean free path length λ_d due to glancing collisions.

The shortcomings with regard to athermal recombination processes during many-body collisions due to non-linearity have been addressed shortly by Nordlund et al. in an athermal recombination corrected (arc) dpa model [67, 90].

2.6 Fundamentals of the Monte Carlo method

The Monte Carlo (MC) method is a tool from the field of stochastics that enables to solve complex problems whose solution in an analytically way is not or only with great efforts possible [114, 115]. Originally pioneered by John von Neumann, Enrico Fermi and Stan Ulam, MC methods have become an indispensable tool for simulative investigations of particle transport problems in any field governed by nuclear and radiation physics. MC methods make use of random numbers and rely on the probability theory, assuming that the considered system is completely described in terms of probability density functions (PDF) [116].

For problems affected by the random nature of radioactive processes, the user can choose from many software packages (e.g. FLUKA, SRIM, MCNP, MARS, PHITS), each based on the same fundamental method as depicted in figure 2.11.

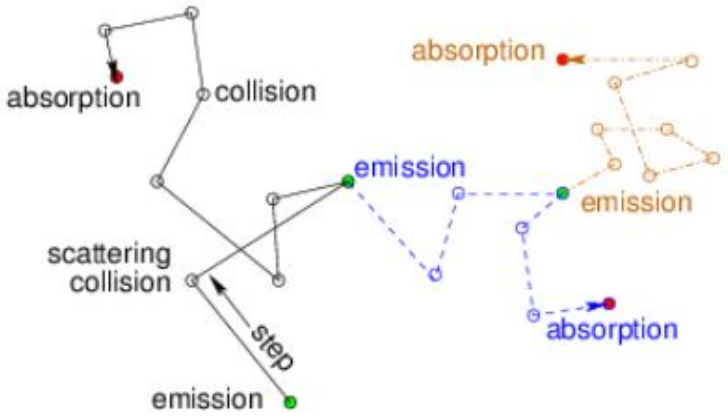

Figure 2.11: Monte Carlo principle of random walks in radiation transport problems. For an emitted neutron (green points), reaction events are mainly scattering, nuclear reactions or absorption (red points). The walk between each event (white circles) is random, and after each event the program recalculates basic properties of the particle such as energy and velocity based on the physics input. [117]

After the user has set a number of particles to be run ("histories"), the program simulates each particle individually [117]. The particle moves in random walks between "events" (interaction mechanisms), each separated by a calculation step. The steps are iterated until the particle is no longer tracked and based on nuclear data banks manifested in the software and corresponding PDFs, the program decides about the fate of the particle.

Quantities such as reaction type, reaction products, scattering angle, remaining energy and velocity are calculated based on the physics input. As the desired output MC simulations yield either quantities of the particle itself or of the traversed matter. These values can be averaged over the whole volume of interest or be divided into small pieces, called "tallies" or "bins".

3. Methods

This chapter represents the methodology part of this thesis, as such it provides information on all the methods and principles applied in the simulations.

The two MC codes used (i.e. FLUKA and SRIM) are handled in a similar manner, though FLUKA as the main part of this thesis is treated most detailed. For each code the frame conditions of the performed simulations, namely the geometrical set up, important parameters used and set and the route of the obtainment of dpa values are presented along with references to central equations given in chapter 2.

3.1 The SRIM code

SRIM (Stopping and Range of Ions in Matter) is a broad collection of MC software packages that enables to calculate numerous features of ion transport problems in matter over a wide range of elements [118, 119]. Typical applications of SRIM include the study of ion implantation, sputtering (emission of surface near target atoms), ion beam therapy in medical therapy but also the use for radiation damage assessments in materials can be observed quite frequently [120–123].

Until now more than 2300 papers have been published making use of the SRIM code [118] and the fact that it is a freeware and provides a user friendly interface (see appx. B.1) facilitates an uncomplicated handling, justifying its great popularity and high reputation within the nuclear community.

Written in FORTRAN, in its core it is based on TRIM (Transport of Ions and Range in Matter), under which name it was formerly termed in 1980 [124]. The ion penetration is treated based on the binary collision approximation (BCA), the underlying physics and recommended use of SRIM is extensively described within an own textbook [125].

SRIM geometry and input parameters

The tantalum target was modeled as a single layer of 5 mm thickness and the used ion and target data can be taken from table 3.1 (see also appx. B.1).

Table 3.1: Set parameters for the SRIM simulations. Lattice and surface binding energy have just been given for the sake of completeness. A total of 15.000 ion runs was observed to satisfy acceptable statistics as it diminished fluctuations.

Ion data	
Type	Proton (H^+)
Number	15.000
E [MeV]	70
Incidence angle θ_{inc} [°]	0
Target data	
Material	Tantalum (100%)
Thickness [mm]	5
Density ρ [g/cm^3]	16.601
Lattice binding energy E_l [eV]	3
Surface binding energy E_s [eV]	8.1
Displacement energy E_d [eV]	90

For the TDE, SRIM suggests a default value of $E_d = 25$ eV. A comparison with the literature revealed that this value sits slightly below a minimum value of ~ 32 eV suggested in [126, 127]. Furthermore, due to the anisotropy of E_d (see chap. 2) values between 32 and 130 eV have been reported in the literature [128]. The SRIM default value was changed to $\boldsymbol{E_d = 90}$ **eV**, as this average value seems to be very reasonable, well accepted and frequently used in the literature [129–131] and also the ASTM suggests this value for tantalum [39, 107]. In order to allow useful comparisons between the different simulation outcomes, that value was of course kept in the FLUKA simulations.

Damage calculation with SRIM

SRIM lacks to yield dpa values as a direct output, the user rather has to process the obtained data properly.

For damage calculation purposes, SRIM can be run in two different modes [67, 125]; **(i)** the *Ion Distribution and Quick Calculation of Damage* mode and **(ii)** the *Detailed Calculation with Full Damage Cascades* mode. Whereas the first one tracks only primary ions (i.e. protons), and hence lacks to be a proper solution to depict the whole cascade damage, the latter one tracks every recoil atom from its creation until its kinetic energy falls below the set threshold E_d.

In the frame of this thesis, simulations were performed only with the **(ii)** *Detailed Calculation with Full Damage Cascades* mode. Average and peak displacement doses (dpa/year) were calculated based on scaling a displacement rate R_d (dpa/s) with time (365 days continuous full power operation) in different ways.
Three different plots were used to calculate the damage (see fig. 4.3 - 4.5):

(a) COLLISION EVENTS

(b) ENERGY TO RECOILS

(c) PHONONS

In plot **(a)**, SRIM gives the number of target displacements, vacancies and replacement collisions in units of 1/Å/Ion. It might be not trivial if one has to take the vacancies or the displacements, but the displacements were taken since they lead to conservative results (see also chap. 4).
The utilized formalism for extracted average values from the **(a)** plots is in principle based on the KP model (eq. 2.28) and the method proposed in [67]:

$$R_d = \frac{dpa}{s} = \frac{\frac{n(Target\,Displacements/Ion)_{SRIM}}{Target\,thickness} \cdot Flux\,\phi}{Number\,density\,of\,Target\,N(Ta)} \qquad \text{(Eq. 3.1)}$$

For peak values, equation 3.1 modifies to:

$$R_d = \frac{dpa}{s} = \frac{n(Target\,Displacements/Ion/\text{Å})_{SRIM} \cdot Flux\,\phi}{Number\,density\,of\,Target\,N(Ta)} \qquad \text{(Eq. 3.2)}$$

In contrast to peak values, for average values the number given by SRIM was divided by the target thickness (i.e. 5 mm).

From **(b)** and **(c)** plots only peak doses were extracted [67]:

$$R_d = \frac{E}{2\,E_d} \cdot \frac{\phi}{N(Ta)} \qquad \text{(Eq. 3.3)}$$

Since SRIM typically uses the ångström unit, $N(Ta)$ was calculated to be 0.0554 atoms/Å^3. The flux (see appx. A.1) was calculated to be ϕ = 8.92606E-03/Å^2/s.

The different procedures are summarized in table 3.2, also indicating if an average (whole target volume) or a peak value (endangered area, bin) are calculated.

Table 3.2: Different calculation methods for dpa values extracted from SRIM.

Calculation method	**Target area**		**Values**	
	Whole	**Critical**	**Average**	**Peak**
Plot (a) & eq. 3.1	Yes	No	Yes	No
Plot (a) & eq. 3.2	No	Yes	No	Yes
Plot (b) & eq. 3.3	No	Yes	No	Yes
Plot (b) & (c) & eq. 3.3	No	Yes	No	Yes

3.2 The FLUKA code

FLUKA (FLUktuierende KAskade, Fluctuating Cascade) is a general purpose MC code qualified for calculations of particle transport and interactions in matter [132–134]. It was developed by Johannes Ranft in 1962 at CERN (Conseil Européen pour la Recherche Nucléaire) and has been improved with a more and more realistic physics input over time, ending up in the meanwhile third generation of the code [135] accounting for 60 different particles that can be simulated with a high accuracy.

FLUKA is applied in a wide diversity of particle transport problems such as accelerator, target and shielding design, dosimetry, neutrino physics, calorimetry, activation studies, astrophysics and medical physics [133].

Since it was originally developed for the assessment of shielding issues in the frame of high energy proton accelerators covering an energy up to several thousands of TeV, it is the standard tool for the radiation protection analyzes in the Large Hadron Collider (LHC) at CERN [136]. One aspect that may make FLUKA superior over alternative transport codes is the fact that benchmarking of novel features against experimental data is an integral part [136].

From the physics point of view, FLUKA treats hadron-nuclear interactions with a very powerful nuclear interaction package, called PEANUT (Pre-Equilibrium Approach to NUclear Thermalization) [137]. Detailed information on the implemented physics can be extracted from the official manual [133] and publications [138, 139].

Input description

Generally, FLUKA input comprises a set of commands or options, denoted as "cards" (see fig. 3.1). Regardless of the type, all cards share the same structure and have; **(i)** a *KEYWORD*, **(ii)** six floating point values ("*WHAT*") and **(iii)** a character string at the end ("*SDUM*").

The different WHAT's can represent numerical quantities such as energy or integer values referring to a certain FLUKA internal data base (e.g. default materials), while the SDUM string is limited to eight characters and further specifies the card. All cards yielding output data are termed as scoring cards or "estimators" in FLUKA.

```
* ..+....1....+....2....+....3....+....4....+....5....+....6....+....7....+....
*  KEYWORD   WHAT(1)   WHAT(2)   WHAT(3)   WHAT(4)   WHAT(5)   WHAT(6)SDUM
BEAM        -70.E-03       0.0       0.0       0.0       0.0       0.0PROTON
BEAMPOS          0.0      5.64       0.0      10.0                   CYLI-VOL
BEAMPOS          0.0       0.0       0.0       0.0       0.0
```

Figure 3.1: FLUKA input card structure. Exemplary, the definition of the proton source as used in all simulations is shown.

The description of the geometry of radiation transport problems is implemented into FLUKA by means of the strong Combinational Geometry (CG), as a modified version of the MORSE [140] program. Once bodies are defined, one can specify different regions by combining bodies with boolean operations; **(i)** *Union*, **(ii)** *Subtraction* and **(iii)** *Intersection*. For complex geometries, computer-aided design (CAD) files can be load with supplementary tools such as FluDAG [141].

Though input files have been prepared in the ASCII format in a normal text editor in any case, *flair* [142, 143] has been used as an advanced graphical user interface to discriminate against errors and to visualize the geometry with the implemented flair geometry editor.

Low energy neutron transport in FLUKA

In FLUKA, neutrons carrying a kinetic energy of less than 20 MeV are referred to as "low-energy neutrons". Internally the transport is handled by means of a discrete multigroup algorithm, dividing neutrons between 20 MeV and 1E-14 GeV into 260 energy groups.

Elastic and inelastic interactions of neutrons are simulated with group-to-group probabilities based on a downscattering matrix. In this matrix, a Legendre polynomial expansion is used to quantify the scattering transfer probability between individual groups [133]. Though pointwise transport may be an alternative offered in the case of a few elements, the multigroup procedure as adopted in FLUKA by default is generally characterized by much smaller computing times.

Activation of low-energy neutron transport was requested with a *LOW-NEUT* card, though it was redundant as it is activated by default anyway. However, artefacts may occur in thin samples or related to the energy structure [133].

Neutron energy groups

The *USRBIN* scoring card is able to yield the total neutron fluence (n/cm^2) as a function of the target depth z, but cannot distinguish between different neutron energies. In contrast, the *USRTRACK* card scores the differential energy spectrum ($d\Phi/dE$), but lacks a binned investigation.

In order to obtain depth information on the neutrons' density coupled with information on their corresponding energy, two measures were done; first of all, the target was divided into 50 equal regions (i.e. each of 0.01 cm thickness). To each of these regions then a corresponding *USRTRACK* card was referred to obtain energy spectral data. Secondly, the *USRTRACK* data for each bin was divided into 5 energy groups (see table 3.3) and post processed with MS Excel.

Table 3.3: Division of the neutron energy spectrum into different energy groups. As the FLUKA internal energy boundaries are fixed and did not coincide with the theoretical proposed values, the adjusted FLUKA values were chosen to be as close as possible to the theory ones.

Neutron group	Energy range [MeV]			
	Theory		FLUKA	
	E_{min}	E_{max}	E_{min}	E_{max}
Cold	1.00E-09	1.00E-08	9.21E-10	1.33E-08
Thermal	1.00E-08	5.00E-07	1.33E-08	5.32E-07
Epithermal	5.00E-07	2.00E-06	5.32E-07	2.38E-06
Resonance	2.00E-06	1.00E-02	2.38E-06	1.03E-02
Fast	1.00E-02	7.00E+01	1.03E-02	7.00E+01

Moderators

The primary neutrons emitted in the Ta target have typically kinetic energies of some MeV, with a peak at $\sim$ 0.5 MeV (see fig. 4.14). The spectrum demanded by the individual scattering, imaging and analytical instruments however demands neutron energies between 1 meV and a few keV only [26].

Therefore, in order to reduce the energy of the neutrons, the target is inserted into a thermal moderator (see table 3.4). The target and moderator ensemble is then in turn surrounded by a reflector and a radiation shielding cage, as illustrated in appendix A.2. In the case of this thesis, the reflector was neglected as it was found out it would not have made a significant difference for displacements (see chap. 5).

For an efficient moderating process, a suitable moderator must decrease the neutrons' energy quickly within a few collisions only. This is quantified in the *macroscopic slowing down power (MSDP)*, defined as the product of the logarithmic energy decrement ξ and the macroscopic scattering cross section Σ_s, i.e. $\xi\,\Sigma_s$ [144]. As moderators should also not absorb neutrons, efficient moderators are additionally characterized by a high *moderating ratio (MR)*, in turn defined as $\xi\,\Sigma_s/\Sigma_a$ with Σ_a as the macroscopic absorption cross section.

Table 3.4: Simulated moderator materials with important parameters. MSDP and MR values are taken from [144]. Light water and polyethylene densities were taken from the FLUKA output files, the heavy water density was taken from [145] and that one for reactor graphite from [146].

Moderator		MSDP [cm^{-1}]	MR	ρ [g/cm^3]
Light water	H_2O	1.28	58.00	1.00
Heavy water	D_2O	0.18	21000.00	1.11
Reactor graphite	^{12}C	0.06	200.00	1.82
Polyethylene	$(C_2H_4)_n$	3.26	122.00	0.94

Apart from light water and polyethylene already being available in the FLUKA default material list, heavy water and reactor graphite had to be defined as new materials. The way of how to define a new material or compound in FLUKA is shown in figure 3.2 exemplary for the case of the heavy water moderator.

```
* ..+....1....+....2....+....3....+....4....+....5....+....6....+....7....+....
* Definition of deuterium
MATERIAL          1.                 1.                                 2.DEUTERIU
* D2O bound Deuterium neutron cross section library at 296 K, Fluka Manual p. 343
LOW-MAT     DEUTERIU       1.0      +2.0     296.0
* Density of D2O = 1.11 g/cm^3
MATERIAL                          1.11                                  DEUTOXID
* Definition of deuterium oxide compound
COMPOUND          2.  DEUTERIU        1.    OXYGEN                      DEUTOXID
```

Figure 3.2: Definition of D_2O as a new material in the FLUKA input. New materials can be defined with proper *MATERIAL* and *COMPOUND* cards.

Since heavy water is a compound made of two deuterium atoms and one oxygen atom, one has to use the *COMPOUND* card. Deuterium was defined as a new material with a unique SDUM (DEUTERIU). The density was set as given in table 3.4 with another *MATERIAL* card and a *COMPOUND* card was used to combine deuterium and oxygen atoms in the right atomic ratio (i.e. 2:1).

A *LOW-MAT* card has been used to link new materials to a proper neutron cross section library.

FLUKA geometry and input parameters

The initial geometrical setup utilized consists only of a bare tantalum target ("simple geometry") and got continuously modified over time towards a more realistic illustration of the target environment as applied in the HBS project. Nevertheless, also the final geometry (see fig. 3.3) including moderators and a beamstop is kept fairly simple, as simulations intend to puzzle out the displacement damage in a qualitative way.

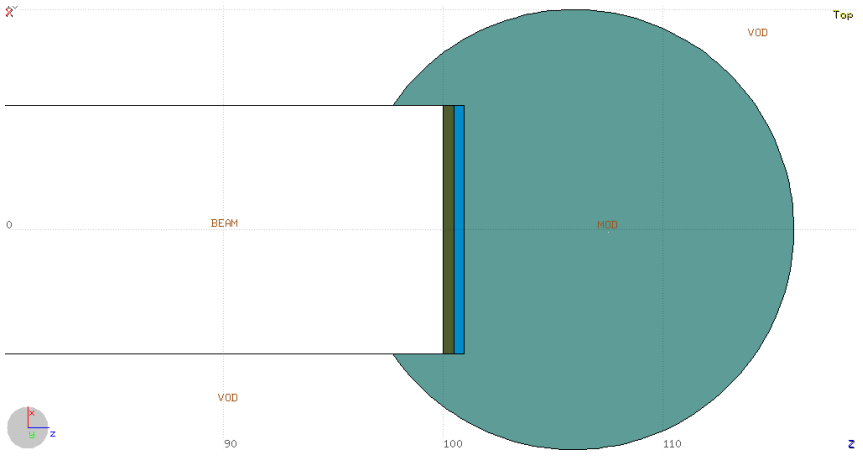

Figure 3.3: Final FLUKA geometry taken from flair. The proton beam impinges from the left perpendicular on the target (dark green), the emitted neutrons get thermalized in the spherical moderator (light green) beyond a beamstop (blue).

The complete geometry (depicted in appx. B.2) is surrounded by a void region ("*VOD*"), which in turn is enveloped by a blackhole region ("*Blk*"), defining the boundary of the system.

The primary proton beam was defined as a 10 cm long cylindrical volume source between two concentric cylinders, the inner one having a radius of 0 cm and the outer one a radius equal to the target radius, i.e. 5.64 cm. The source is centered at the coordinate origin and the protons are emitted in vacuum either in the *BEAM* or *VOD* region (see fig. 3.3 and appx. B.2). The distance present between the source and the target was chosen to be 100 cm, which should just illustrate a LINAC but does not influence the simulations and computing time in any way.

The beamstop, made of ordinary water (H_2O), was modeled with a thickness of 0.45 cm, sufficient to stop protons (except those entering the moderator through lateral scattering in the target, see fig. 4.2 and 4.6). The spherical moderator of radius r= 10 cm is centered 5 cm behind the beamstop.
The geometric arrangement with its dimensional specifications of all relevant parts is summarized in table 3.5.

Table 3.5: Geometrical parameters set for the FLUKA simulations.

Parameter	**Target**	**Beamstop**	**Moderator**
Material	Tantalum (Ta)	Light water (H_2O)	Varying
Radius r [cm]	5.64	5.64	10.00
Thickness d [cm]	0.50	0.45	-
Center pos. (x, y, z) [cm]	0, 0, 100.25	0, 0, 100.725	0, 0, 105.95

Regarding the particle transport, a global threshold energy of 1E-14 GeV was defined by a *PARTH-THR* card for all hadrons, muons and neutrinos generated during the collision cascade. Radioactive decay of residual nuclei was ignored as it is switched off by default. For electrons, positrons and photons the default transport and production thresholds were used, as a minor contribution to atomic displacements from these particles was expected and partly also been observed (see fig. 4.11 and 4.13).

In order to obtain satisfying statistics and to prevent artefacts due to statistical fluctuations, the number of primary source protons to be simulated was always set to be 10^7.

Damage calculation with FLUKA

Radiation damage studies are a very traditional application of FLUKA, since it was originally developed for that purpose. In contrast to SRIM it is possible to obtain dpa values as a direct output of simulations in FLUKA, a feature enabled by use of the *DPA-SCO* option available in the SDUM of the *USRBIN* scoring card.

FLUKA uses a sophisticated model for dpa calculations, based on an uniform implementation of the classical standard NRT formula (eq. 2.29) with a minimum input of the user [103]. The only parameter that has to be defined is the TDE, done with a *MAT-PROP* card and the SDUM as *DPA-ENER*.

Table 3.6: Details of the different scorings in FLUKA. All simulations described were performed with the simple geometry and the denoted moderators. Filtering of the estimators' content for different particles was done via an *AUXSCORE* card.

Atomic displacements (dpa)						
Card	**WHAT(2)**	**Avg.**	**Peak**	**z-bins**	**r-bins**	**Mod.**
USRBIN	DPA-SCO	Yes	No	-	-	All
USRBIN	DPA-SCO	No	Yes	100	1	All
USRBIN	DPA-SCO	-	-	50	50	D_2O
USRBIN	RES-NIEL	Yes	No	-	-	None
USRBIN	RES-NIEL	No	Yes	100	1	D_2O
Energy deposition						
Card	**WHAT(2)**	**Avg.**	**Peak**	**z-bins**	**r-bins**	**Mod.**
USRBIN	ENERGY	Yes	No	-	-	All
USRBIN	ENERGY	No	Yes	100	1	All
USRBIN	ENERGY	-	-	50	50	D_2O
Neutron spectra (fluence)						
Card	**WHAT(2)**	**E_{min} [MeV]**	**E_{max} [MeV]**	**z-bins**	**r-bins**	**Mod.**
USRBIN	NEUTRON	-	-	100	1	All
USRTRACK	NEUTRON	1.0E-15	100.0	-	-	All

For atomic displacements, the FLUKA output is given as average dpa in each bin per unit primary weight (i.e. source protons), but care must be taken that the region binned values in contrast to the axially binned values actually not exactly give the desired dpa values. As it was figured out in a discussion with the code developers in the FLUKA mailing list, region binned values are multiplicated by the volume of the region, thus one has to divide these values by the target volume (~ 50 cm^3).

As an alternative to the FLUKA internal "*DPA-SCO* method", for the simple geometry dpa values have been also obtained based on the NIEL. The concept of NIEL is implemented into FLUKA exactly based on a way described in equations 2.22 to 2.27 given in chapter 2 [103]. It was evaluated as the energy-restricted NIEL with E_d as the lower energy boundary via the *USRBIN* card SDUM option *RES-NIEL* (see table 3.6). These values were then processed with the following formalism:

$$N_{d,NIEL} = \frac{N_F \, \phi \, M}{\rho \, N_{Av}} \qquad \text{(Eq. 3.4)}$$

with N_F as the number of FPs after the original KP model, i.e. $T_d/2\,E_d$ with T_d as the damage energy (energy value given by *RES-NIEL* scoring).

Simulation procedure and data processing

All simulations were run on an internal server of the research centre Jülich, on which the Fluka2011.2x.8 version is installed. The server could be accessed also from outside the research centre area, in any case the Ubuntu 18.04 LTS console was used to log into the server. Although there are several important commands [133], the most noteworthy command is that one to run a simulation:

$FLUPRO/flutil/rfluka -N0 -M3 filename

The FLUKA simulations are executed using the rfluka script that can be launched for multiple FLUKA cycles, which are independent from each other and all start with another random seed. The filename has to be written without the ending .inp. In the command above, the number following -N specifies the previous cycle that has been completed, -M specifies the total number of cycles to be run. In all simulations a total of three cycles were run.

To access the results requested by the individual estimators, the binary output was processed with different readout codes depending on the estimator type. These codes take the average of the requested radiometric quantities for all cycles and calculate the error on a cycle-by-cycle basis and not on a history-by-history basis as common in most MC codes [147].

Further post-processing was done in a spreadsheet program (MS Excel), and the data was visualized with Matlab R2017a. In particular, any values containing the unit of energy were scaled from units of GeV to units of MeV.

4. Simulations

In this chapter the outcome of all the simulations is presented in the form of plots. Though first comments are done, the detailed and broad discussion of the results as well as their interpretation in the frame of a damage estimation of the target follows in chapter 5, in which any numerical data will be given.

FLUKA simulations comprise the main body of all simulations. They are complemented by SRIM simulations for reasons of plausibility checks and intercode comparisons.

4.1 Investigations with SRIM

Though the tracking of neutral particles is possible in SRIM with some efforts principally [125], in the case of this thesis the transport of uncharged particles was not requested but only that of charged ones. Consequently, these simulations are intended to reflect the displacement damage due to the primary source protons and Ta recoil atoms. From the .txt files generated it was also evident that SRIM automatically divided the target width of 5 mm into 100 bins, i.e. bins of 0.05 mm thickness.

In the HBS project both, the proton energy and target thickness, are matched in a way that the protons' highest energy deposition (i.e. Bragg peak) occurs very close behind the target in a thin layer of water, called "beamstop". This represents a design optimization since the required cooling is reduced significantly without a considerable reduction in the obtained neutron yield at the same time.

In SRIM it is not possible to get the complete energy loss (nuclear and electronic) plotted as a function of the target depth, rather it produces a datafile called IONIZ.txt containing energy losses from ions and produced recoils to electrons. Also the axial distribution of the Ta recoils was obtained, both depicted in figure 4.1, already hinting that the nuclear energy loss responsible for displacements is highest at the back of the target with the highest recoil density.

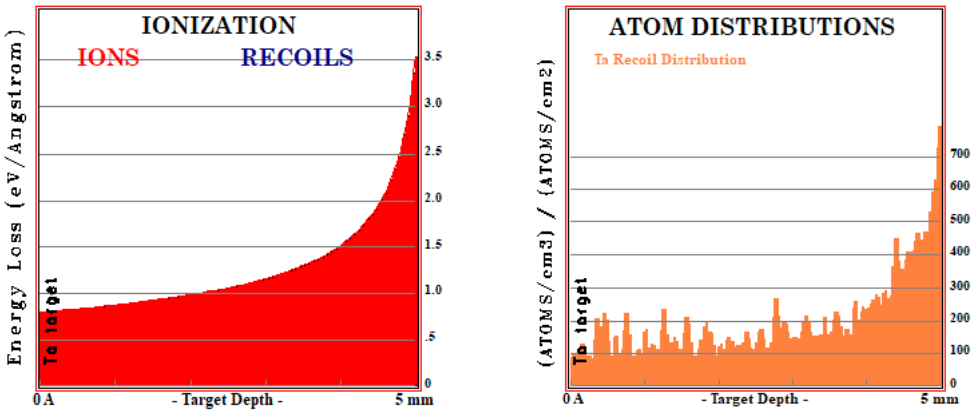

Figure 4.1: Proton energy deposition along the target depth and recoil atom distribution in SRIM. Left: The protons deposit more and more energy with increasing target depth, the maximum (Bragg peak) is not located in the target. Right: Distribution of produced Ta recoil atoms along the target depth.

The trajectories of the protons in the target and their stopping in the thin beamstop is shown in figure 4.2. With increasing penetration depth the beam broadens up and it can be considered to be stopped after a subsequent water layer of $\sim$ 2 mm (see also fig. 4.6).

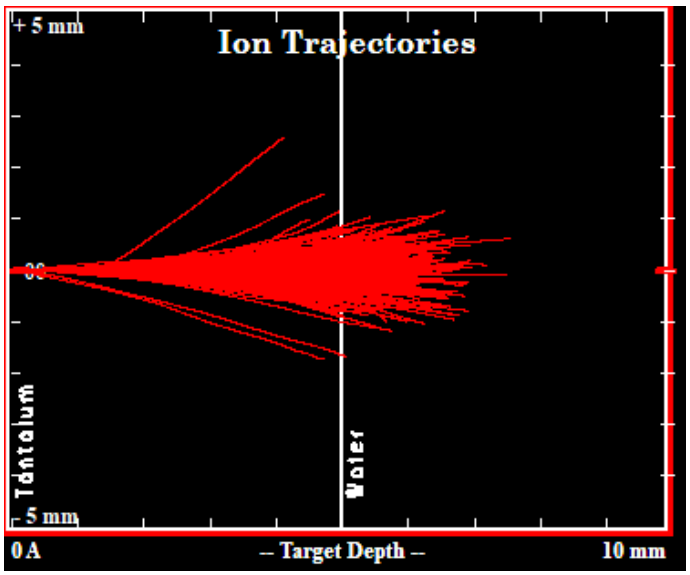

Figure 4.2: SRIM ion trajectories along the Ta target. Roughly 300 ions were tracked, since the visualization of the trajectories is at the expense of a large computing time. In the HBS project, the protons will deposit the majority of their energy (Bragg peak) within a subsequent "beamstop" made of ordinary water. Obviously, a thin layer of $\sim$ 2 mm is sufficient to completely stop the proton beam.

In order to quantify the extent of atomic displacements in the target, three plots were obtained and corresponding dpa values were extracted in the manner described in table 3.2. For all these plots (collision events, energy to recoils, phonons) $\sim$ 91% of the protons transmitted the tantalum target layer, only 6 (i.e. 0.04%) of them experienced intense collisions and occured to be backscattered.

Collision events

For the purpose of radiation damage calculations SRIM offers the possibility to plot various collision events over the target depth. These events comprise target (atomic) displacements, target vacancies and replacement collisions. They are related to each other as:

$$\textbf{Target displacements} = \textbf{Vacancies} + \textbf{Replacement collisions}$$

In principle, it could be argumented for both target displacements and vacancies to be taken as a basis for damage calculations, making the decision non-trivial. However, as mentioned in chapter 3, a conservative way neglects replacement collisions and is based on the total number of displacements occured.
Therefore, the amount of target displacements required for the dpa calculations of average and peak values based on equations 3.1 and 3.2 is shown in figure 4.3. Obviously, the back of the target is mostly endangered with the majority of displacements.

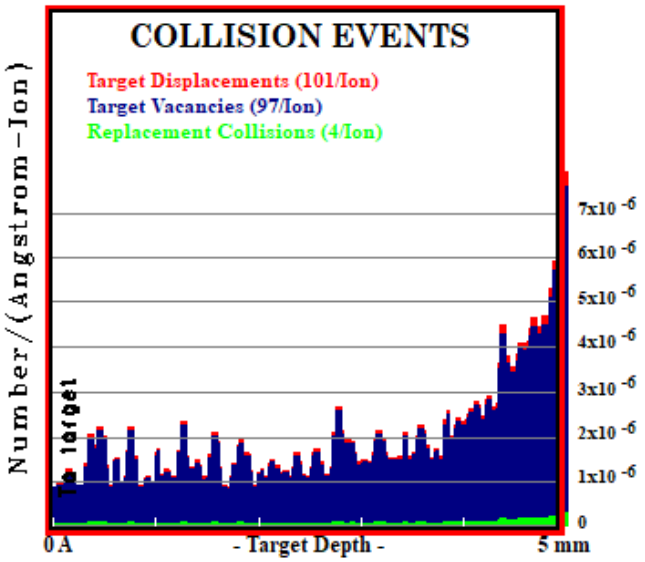

Figure 4.3: Different collision events in the Ta target of the SRIM simulation. Calculations are based on the number of target displacements, i.e. 101/Ion in the case of an average and $\sim 8 \cdot 10^{-4}$/Å/Ion for a peak value.

Recoil and phonon data

As damage values can also be extracted from the amount of energy transferred to the recoil atoms, the energy spectrum of tantalum recoils is shown in figure 4.4. As energy deposited in inelastic stopping processes such as ionization, excitation or the emission of bremsstrahlung is incapable to induce atomic displacements, only the nuclear deposited energy should serve for calculations to be as meaningful as possible. Indeed, the recoil energy depicted reflects energy lost due to nuclear stopping.

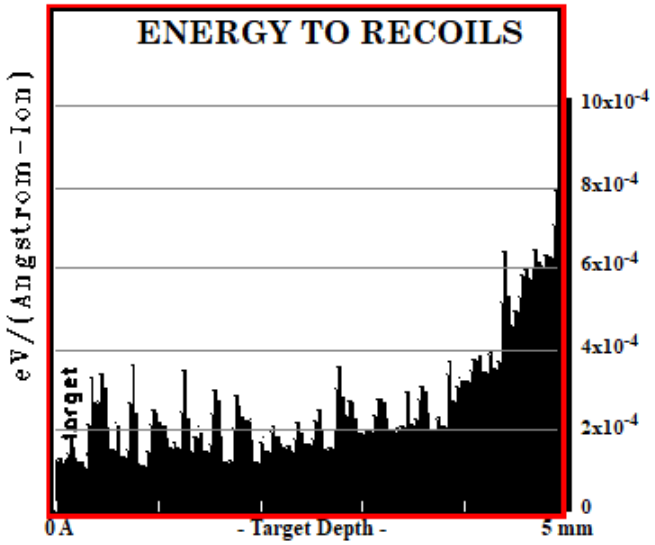

Figure 4.4: SRIM recoil atom energy spectrum. The energy depicted is nuclear deposited energy as that one is the energy transferred in elastic collisions from the protons to the tantalum atoms in the displacement process. Numerical calculations use the maximum value of $\sim 10.11 \cdot 10^{-4}$/eV/Å/Ion from the E2RECOIL.txt file.

As declared in [67], recoiled atoms in turn will also deposit energy in a nuclear way by the emission of phonons. The primary source protons will also partly exhaust some of their energy for phonon production. Therefore, for an improved dpa calculation after [67] the creation of phonons (see fig. 4.5) should be taken into account.

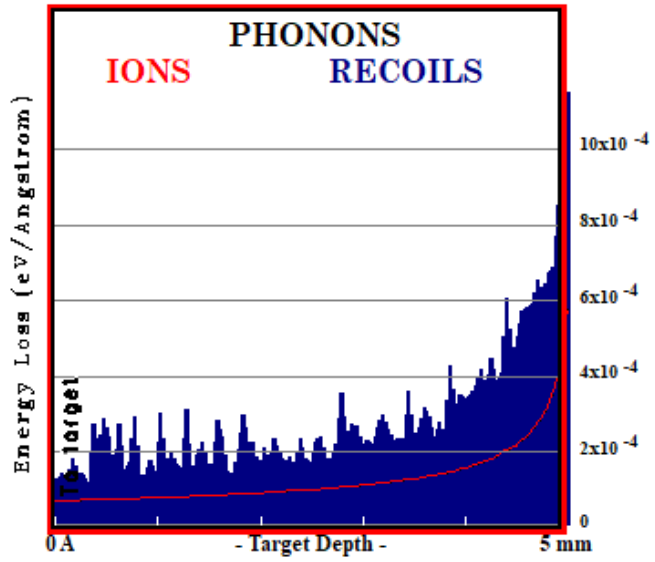

Figure 4.5: SRIM energy losses resulting in phonon creation. Note that the PHONON.txt file showed the unit to be eV/Å/Ion, so the maximum energy loss from protons to phonons used in calculations is $\sim 5.71 \cdot 10^{-4}$/eV/Å/Ion.

However, it shall be already mentioned here that phonon production mostly is referred to as a sub-threshold reaction, as such taking place preferentially at energies less than E_d. Hence, if the additional consideration of energy losses due to phonon production is really justified and if it leads to an improved damage assessment, will be discussed in chapter 5.

4.2 Investigations with FLUKA

Representing the main part of the simulative work in the frame of this thesis, FLUKA simulations intend to determine information on atomic displacements coupled with energy deposition and neutron spectral data (see table 3.6).

Aiming to give a first hint about the expected damage and its connected characteristics, first of all rough preliminary overview simulations utilizing the simple geometry have been performed. Therefore, the hadronic collision cascade was investigated for a broad spectrum of charged and uncharged particles and for proton energies of 10, 30, 50, 70 and 90 MeV. The characterization of the collision cascade aims to reveal the main contributors to the atomic displacements in the HBS tantalum target.

The creation of atomic displacements caused by neutrons created in (p,xn) nuclear reactions between tantalum atoms and impinging source protons was then investigated in detail. After previous SRIM simulations targeted the damage due to protons, FLUKA simulations focus on the damage caused by neutrons.

In particular, the influence of different moderators (see table 3.4) is presented along with corresponding neutron spectra, as moderators generally are expected to increase the neutron population in a target and hence the potential damage. Due to the close relationship between deposited energy and displacements, the energy deposition inside the target was simulated. Plots for the energy deposition of all particles, protons and neutrons with and without beamstop and the varying moderators are mainly given in appendix B.

In order to explain the surprising results due to the neutron damage (see chap. 5), several validation simulations have been conducted also.

4.2.1 Prelmininary overview simulations

Since the goal of the preliminary simulations is to give a broad overview on the displacement damage, simulations were performed with varying proton energies (10, 30, 50, 70 and 90 MeV).

Also, as the extent of displaced atoms strongly depends on the deposited energy, a relationship between these two quantities was worked out. Though indeed only the nuclear deposited energy contributes to atomic displacements, the whole deposited energy including energy losses due to electronic stopping processes was scored. In the frame of the philosophy of a broad overview this however was taken to be sufficient.

Moreover, the hadronic collision cascade was analyzed meticulously, covering a wide range of both charged and neutral particles.

The technological enhancement of stopping the primary proton beam not in the target itself but just closely behind inside a thin layer of water was also demonstrated with FLUKA, which is depicted in figure 4.6.

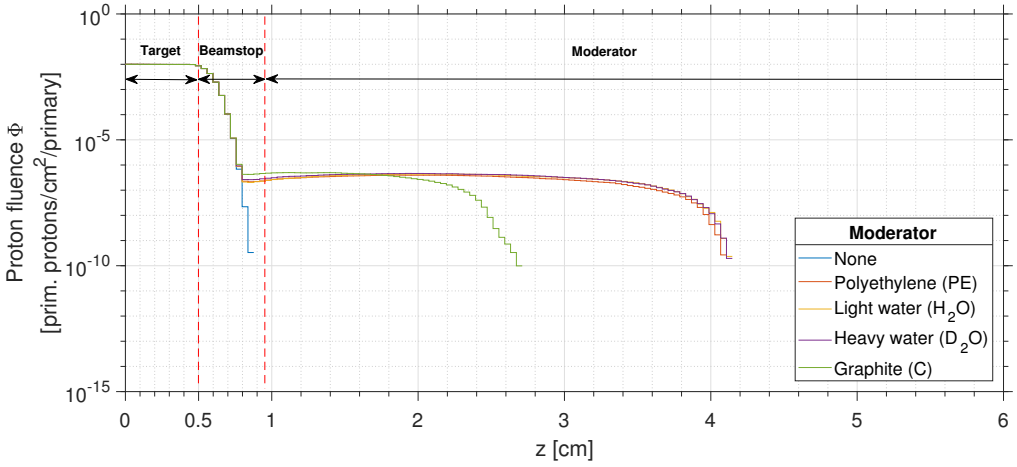

Figure 4.6: Primary source proton distribution along beam direction (z-axis). As the protons do not penetrate far enough to enter the rear region of the moderator, only a part of the moderator is displayed.

Along the z-axis the proton fluence was scored with a *USRBIN* card, binned from the point where the protons enter the target (z= 0 cm) up to the end of the moderator (z= 15.95 cm). That range was divided into the maximum possible number of bins (400) and the data is not shown for the whole length since the protons do not reach the rear region of the moderator. In order to discriminate against secondary protons produced via various nuclear reactions, the *USRBIN* estimator was evaluated with a *BEAMPART* instead of a *PROTON* argument in the WHAT(2) field.

At first sight, one might wonder why protons are stopped in the beamstop but further propagate if a moderator is included. Simply, this is an "artefact" due to the geometry, as protons might enter the moderator laterally (see fig. 3.3).

Deposited energy and displacements

In both, simulating the deposited energy as well as the atomic displacements, no *AUXSCORE* card has been used for filtering the information with regard to different particles. As these simulations are general, rather contributions from all generated particles were considered.

The deposited energy is shown in figure 4.7 and the corresponding displacements are depicted in figure 4.8. As already mentioned, the deposited energy here does not exclusively belong to nuclear stopping but contains also contributions from electronic stopping processes, since this simulation shall be very general and qualitatively only. Therefore, it was also not restricted in energy, i.e. particles with a kinetic energy $<$ E_d contribute as well.

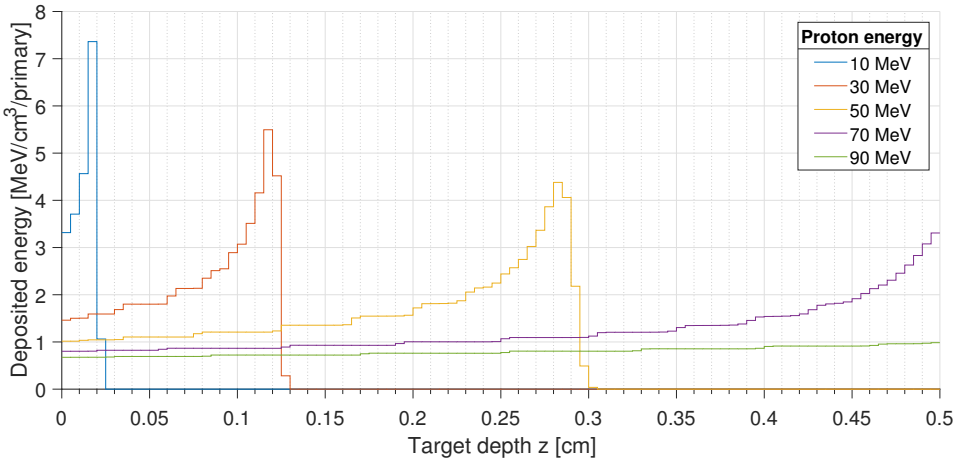

Figure 4.7: Energy deposition of all particles as a function of the target depth for varying proton energies and the simple geometry.

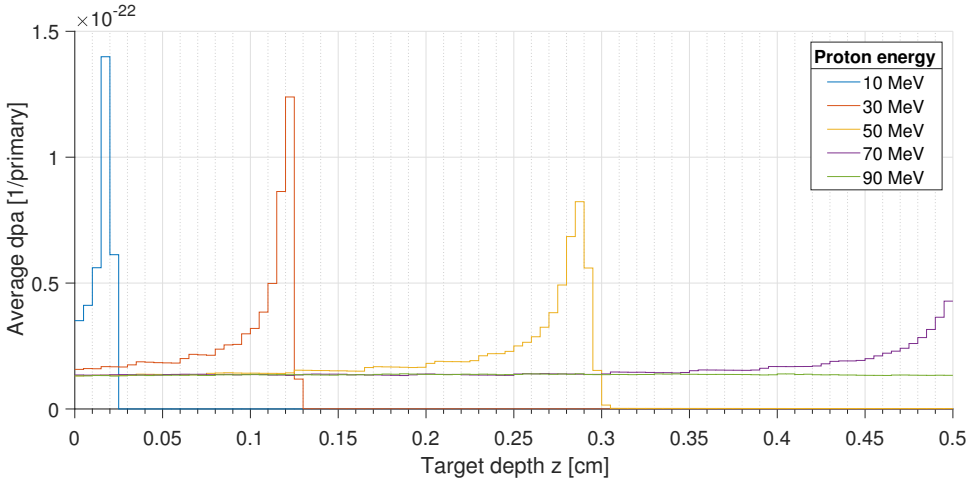

Figure 4.8: Atomic displacements of all particles as a function of the target depth for varying proton energies and the simple geometry.

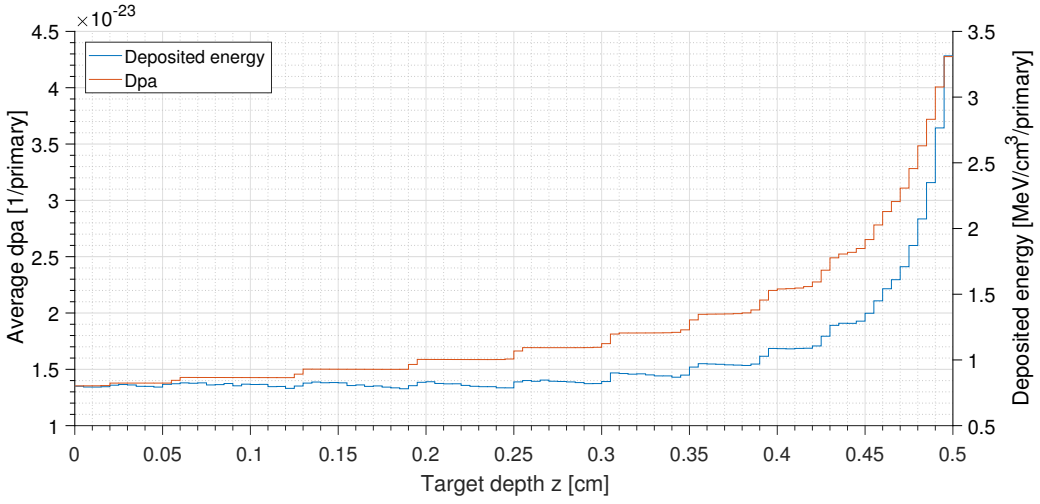

Figure 4.9: Energy deposition and atomic displacements along the target depth for 70 MeV primary proton energy and the simple geometry.

Once again, figure 4.7 nicely shows the increasing energy losses as the penetration depth of protons in the tantalum target rises. Clearly, the Bragg peak is located outside. At 90 MeV, the proton beam actually penetrates the thin target without significant energy deposition.

In order to point out the correlation between deposited energy and displacements more efficiently, figure 4.9 shows both quantities together in one single plot for the case of 70 MeV. Unmistakable, the amount of atomic displacements is a strong function of the deposited energy and hence it is shaped like a stopping curve along the target depth.

Hadronic collision cascade

The hadronic collision cascade was investigated by splitting the displacements per atom evaluation into several charged and neutral particles, which can be found in appendix B.3 together with their corresponding dpa values (per primary source proton).

In the form of a table, the official FLUKA manual [133] contains a library of all particles that can be transported and scored. With regard to this table particles have been selected based on two considerations; first **(i)** of all the particles should have a certain mass, as a tendency of more frequent displacements with greater momenta was assumed. Secondly **(ii)**, this would then inherently exclude any kind of low-mass "exotic" particles, which indeed make the majority of the library.

First of all a very general differentiation of charged and neutral particles as a whole was performed, as illustrated in figure 4.10.

The investigation of charged particles was fanned out into a huge diversity of ions, shown in figure 4.11.

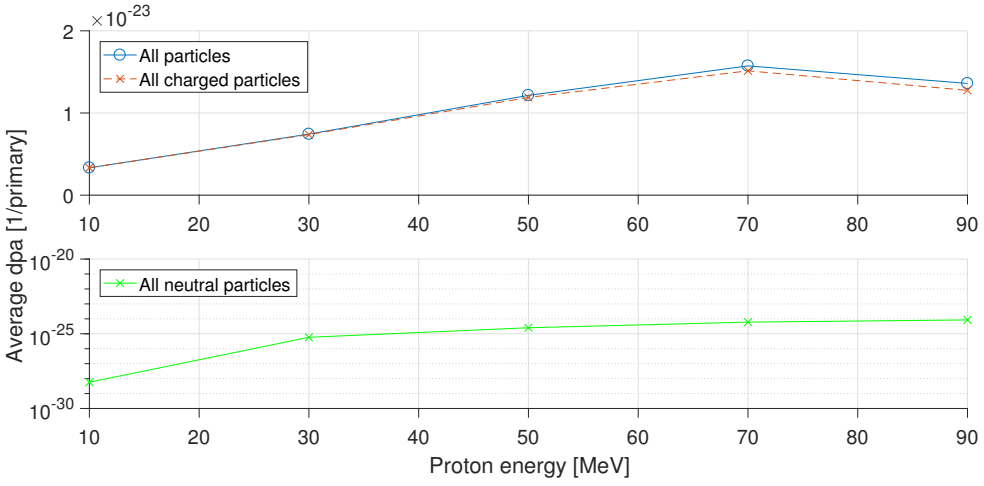

Figure 4.10: Contribution of charged and neutral particles to the total amount of atomic displacements as a function of the proton energy.

As an explicit scoring of tantalum recoils is not possible, the contribution of heavy ion (Z > 2) recoils to atomic displacements has been scored. Since the target is monoatomic and radioactive decay was disabled, it is reasonable to take that value as a first and rough approximation for the Ta recoil contribution to the displacements.

Charged particles such as alpha particles (i.e. Helium-4 nuclei), deuterons or tritons are a result of nuclear reactions inside the tantalum target.

Note, that the particle diversity within a collision cascade can differ from case to case, not all existing particles have to be produced. In particular, Helium-3 was also requested for the scoring but it was probably not produced throughout the whole simulated energy range (see appx. B.3).

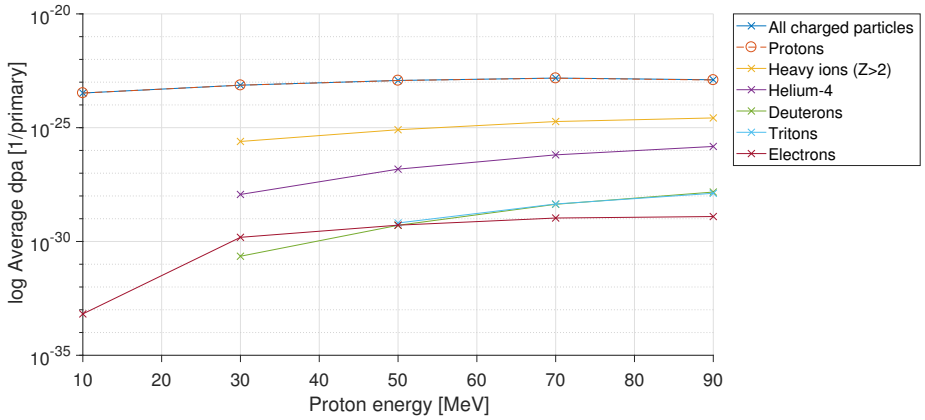

Figure 4.11: Contribution of different charged particles to the total atomic displacements of charged particles.

As it is clearly visible that protons dominate in the atomic displacements by far, another simulation was performed with the goal to figure out the relevance of secondary protons created in nuclear reactions. This is shown in figure 4.12. Analogous to figure 4.6, the *USRBIN* scoring card was evaluated with a *BEAMPART* argument to differentiate from secondaries.

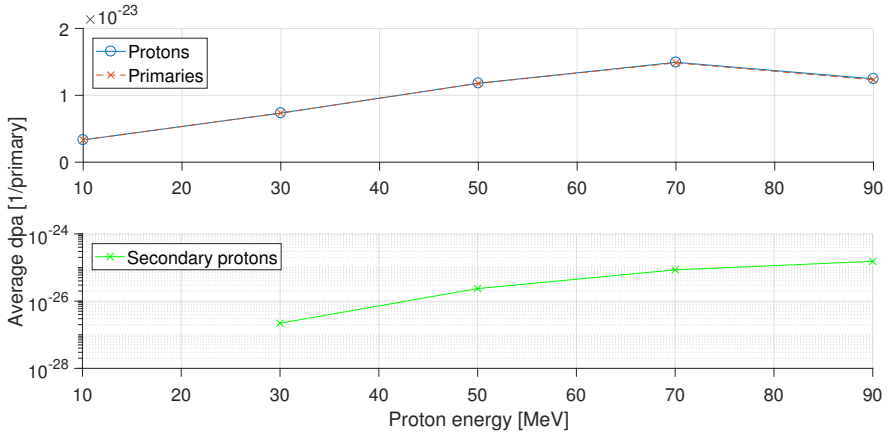

Figure 4.12: Proton atomic displacements for varying energies, splitted into primary source protons and secondary protons produced in nuclear reactions.

As the charged particles have been investigated in details, the contribution of neutral particles was split up as well, namely into neutrons and photons. Again, "exotic" particles such as neutrinos or antineutrinos have been neglected. The competition in atomic displacements between neutrons and photons is depicted in figure 4.13.

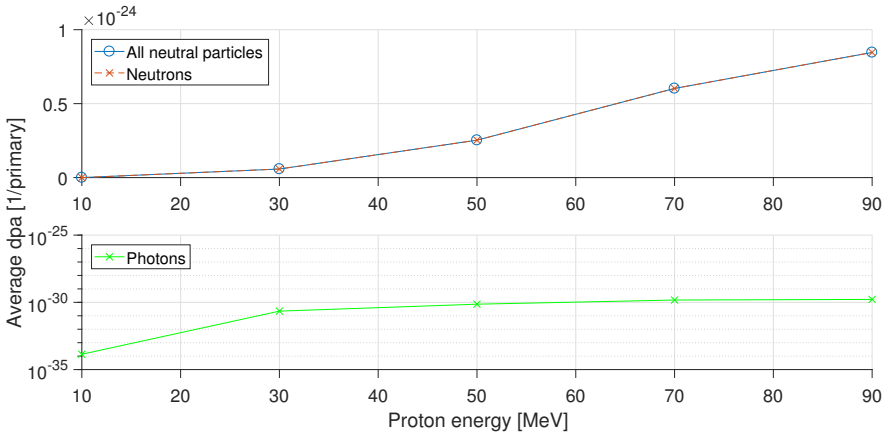

Figure 4.13: Contribution of neutrons and photons to the atomic displacements of all neutral particles as a function of the primary proton energy.

4.2.2 Neutron damage

For the investigation of the neutron damage, the influence of different moderators (see table 3.4) was examined.

For a proper damage assessment regarding neutrons, knowledge about the neutrons' density and their corresponding energies along the target is required. Therefore, spectra were obtained for all cases.

Neutron spectra

First of all neutron spectra were obtained with the simple geometry, i.e. just the bare tantalum target without beamstop and moderator.
Spectras were mostly obtained with the *USRTRACK* card, but also with the *USRBIN* estimator.

The *USRTRACK* data was plotted as differential energy spectra, i.e. $d\Phi/dE$. Though multiplication of each bin value with its corresponding width in units of energy is common, it was found out to be not useful in neutron spectras obtained with FLUKA, as the bin width is not constant. The number of energy bins a user can define in the *USRTRACK* card does actually just affect energies > 20 MeV, for lower energies the width is logarithmically fixed for all 260 neutron groups (see chap. 3). Consequently, it was observed that a multiplication will induce an unphysical discontinuity (jump or drop, see appx. B.4) at 20 MeV.

The neutron energy spectrum for 70 MeV proton energy is depicted in figure 4.14. The data for all other proton energies can be seen in appendix B.5.

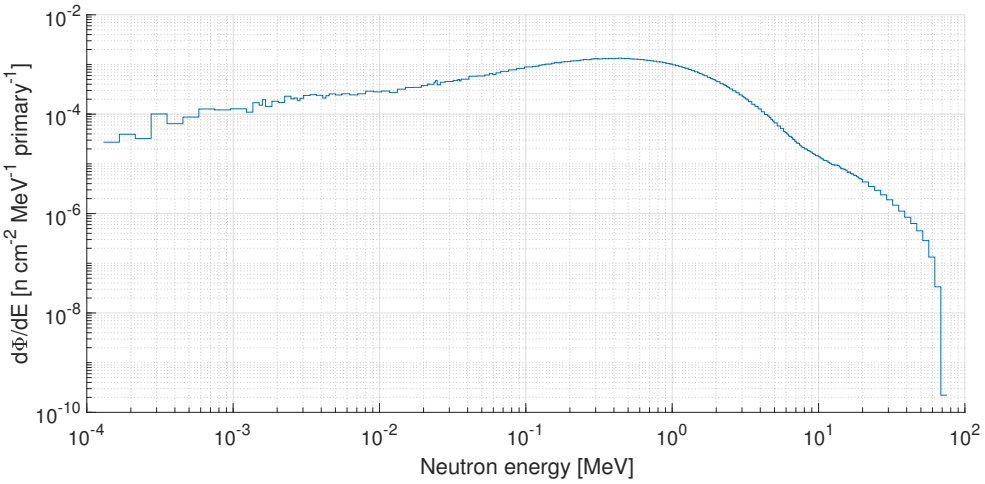

Figure 4.14: Differential neutron energy spectrum of the simple geometry for a proton energy of 70 MeV.

In agreement with [26], the spectrum peaks at an energy of ~ 0.5 MeV.
The result of the *USRBIN* scoring for all energies is given in figure 4.15.

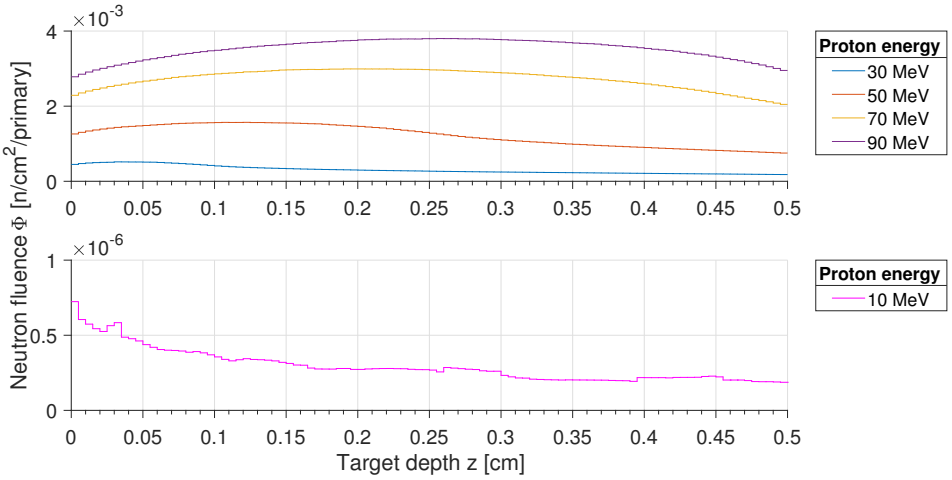

Figure 4.15: Total neutron fluence as a function of the target depth for the simple geometry and varying proton energies.

The total neutron fluence over the target depth for all moderators is shown in appendix B.6, the differential energy neutron spectra for all moderators are shown in figure 4.16, indicating also the value for E_d.

Another "artefact" is visible in the low-energy neutron peak. Although a thermal peak is expected, the representation of the spectrum as differential energy spectrum might lead to an overestimation of that one. As each bin is normalized per MeV, and the bin width below 20 MeV is much smaller compared to bins beyond 20 MeV, bins below 20 MeV are much more emphasized.

The spectra were also divided into different neutron energy groups (see chap. 3, table 3.3). The neutron fluence of these groups is exemplary shown for a D_2O moderator in figure 4.17. The fluence for all 5 energy groups is given from appendix B.7 to B.11.

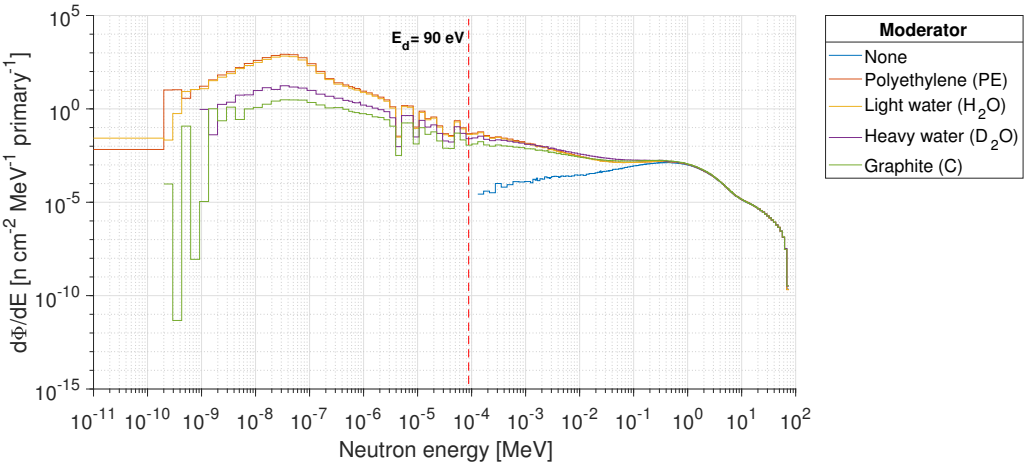

Figure 4.16: Differential neutron energy spectra for all moderators and 70 MeV proton energy.

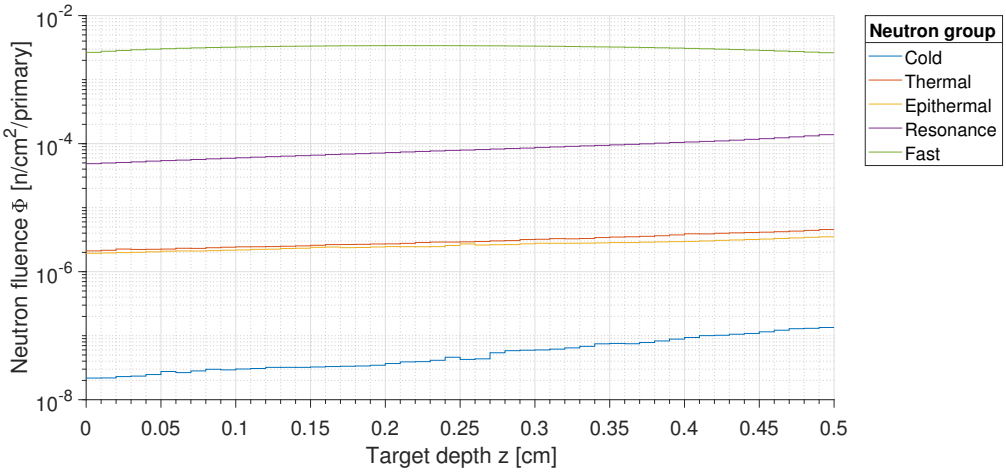

Figure 4.17: Neutron spectrum divided into different energy groups according to table 3.3 for a D_2O moderator.

Bare target

For the bare target, atomic displacements have been plotted as a function of the target depth for all particles, protons and neutrons (see fig. 4.18).

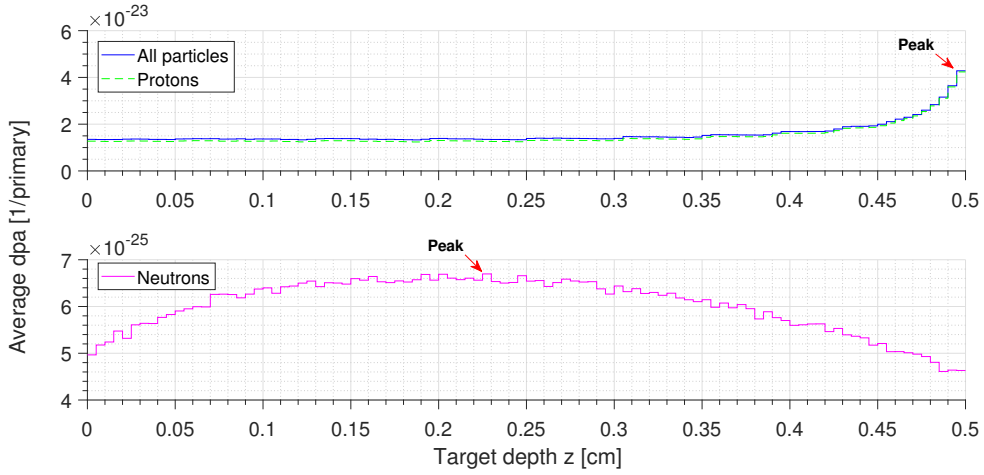

Figure 4.18: Atomic displacements of all particles, protons and neutrons as a function of the target depth for the simple geometry without beamstop and moderator.

Additionally, the target was investigated by means of a 2-dimensional binning with 50 radial and axial bins (see fig. 4.19 and table 3.6). It should be noted that the radial binning did not distinguish between the top or bottom side of the target. However, as the primary proton beam was anyway defined as a homogenous source, this plays no role.

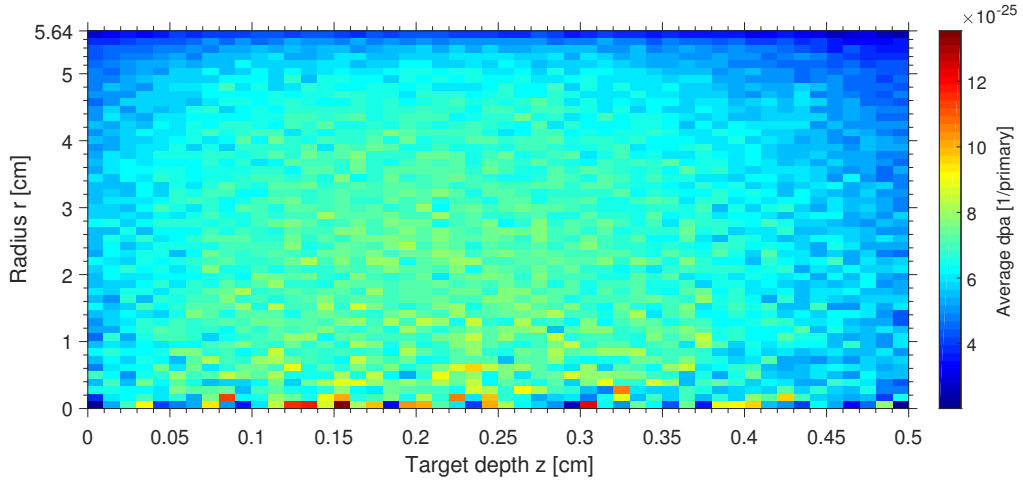

Figure 4.19: Neutron atomic displacements as a function of the target depth and radius for the simple geometry without moderator and beamstop.

Moderators and beamstop

The neutron atomic displacements for all moderators are depicted in figure 4.20. The corresponding energy deposition is given in appendix B.12 (appx. B.13 and B.14 also give that one of all particles and the protons).

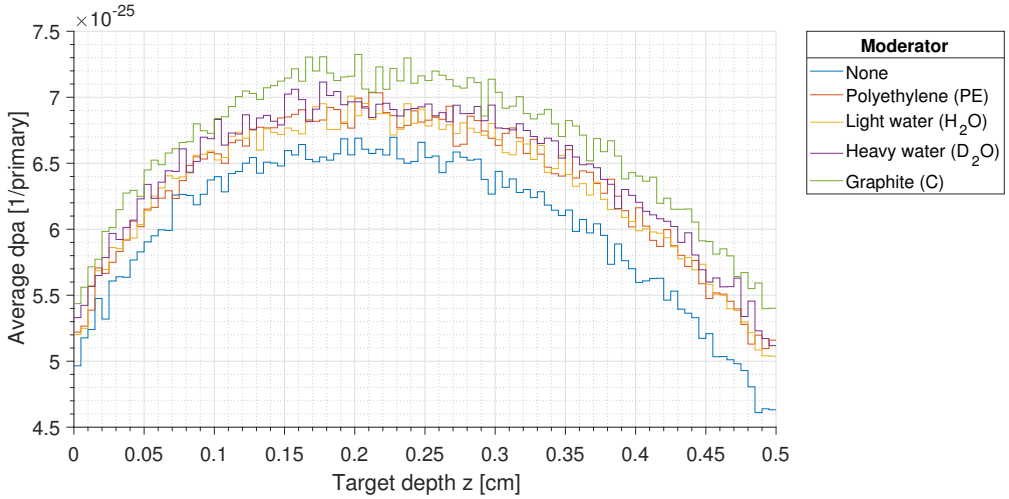

Figure 4.20: Neutron atomic displacements as a function of the target depth for different moderators.

In addition to neutrons, both the energy deposition as well as displacements have been plotted 2-dimensional for all particles and protons and with and without moderator. However, since the plots with and without moderators were found out to be extremely similar (comp. fig. 4.19 and 4.21) in a qualitative way, appendix B.15 to B.19 just represent data with regard to the D_2O moderator.

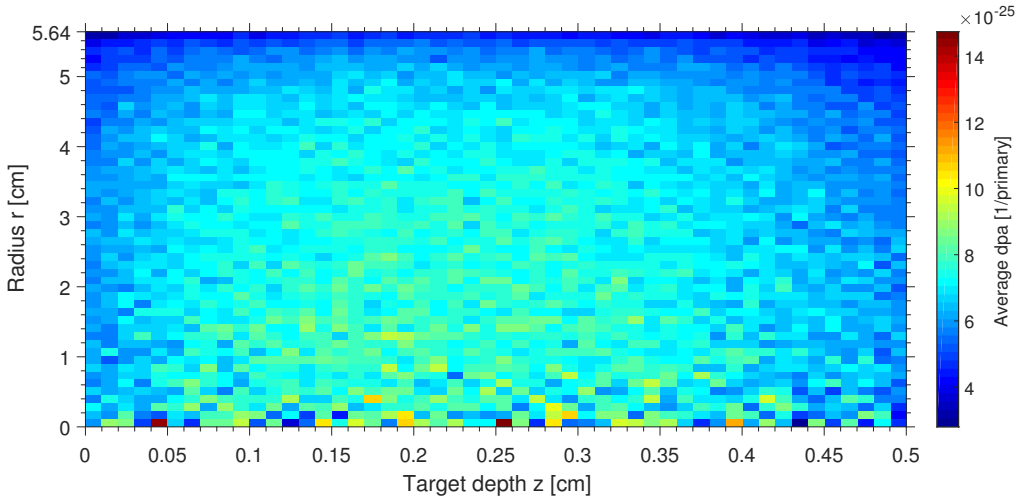

Figure 4.21: Neutron atomic displacements as a function of the target depth and radius for a D_2O moderator.

Dpa with Non-Ionizing Energy Loss (NIEL)

As an alternative to the FLUKA internal *DPA-SCO* method, dpa values were also obtained based on the NIEL concept (see chap. 3) for the simple geometry.

In order to visualize differences efficiently, the results of both methods are shown in figure 4.22. Numerical results, which also compare the different methods, are also given for all particles and protons in chapter 5.

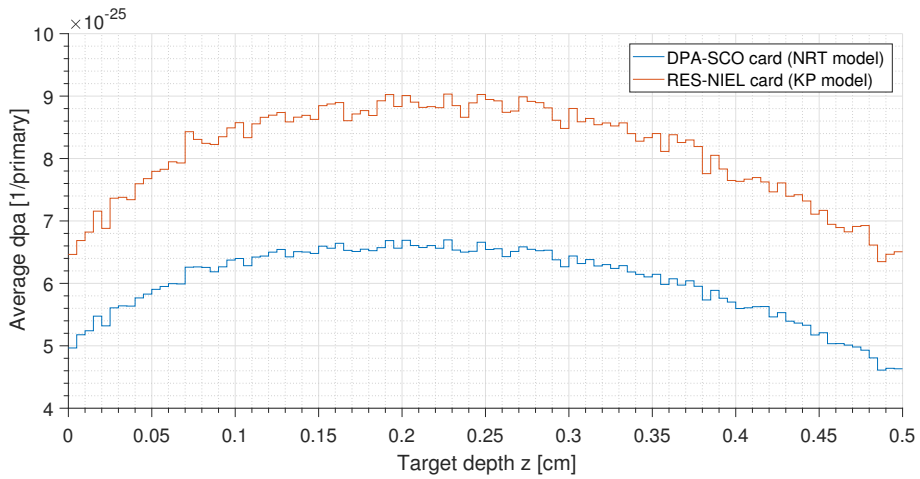

Figure 4.22: Neutron atomic displacements obtained via *DPA-SCO* card (NRT model) vs *RES-NIEL* card (KP model).

Validation simulations

As already visible and also in the disussion of the simulation data in chapter 5, the neutrons' contribution to the atomic displacements is negligible in comparison to the damage induced by protons.

In order to find a reason for that damage pattern, several systematic validation simulations have been performed.

First of all, the influence of the moderator size was simulated. Calculated average and peak neutron displacement doses (dpa/year) are shown in figure 4.23 for the case of a D_2O moderator. The doses have been evaluated for a moderator radius between 0 and 50 cm in steps of 5 cm.

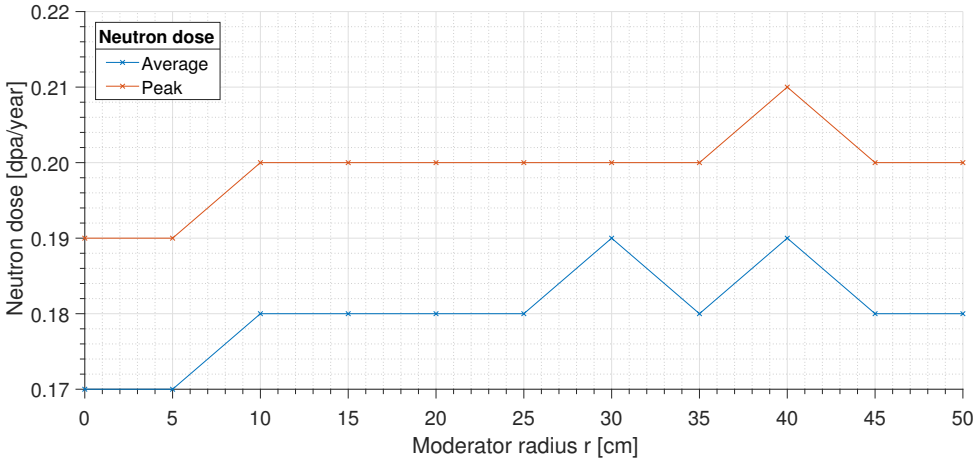

Figure 4.23: Average and peak neutron displacement doses (dpa/year) as a function of a D_2O moderators radius.

Moreover, the neutron dose was plotted as a function of varying target thicknesses. A total range of 10 cm was covered with the intervals being finer for thicknesses $<$ 1 cm as depicted in figure 4.24.

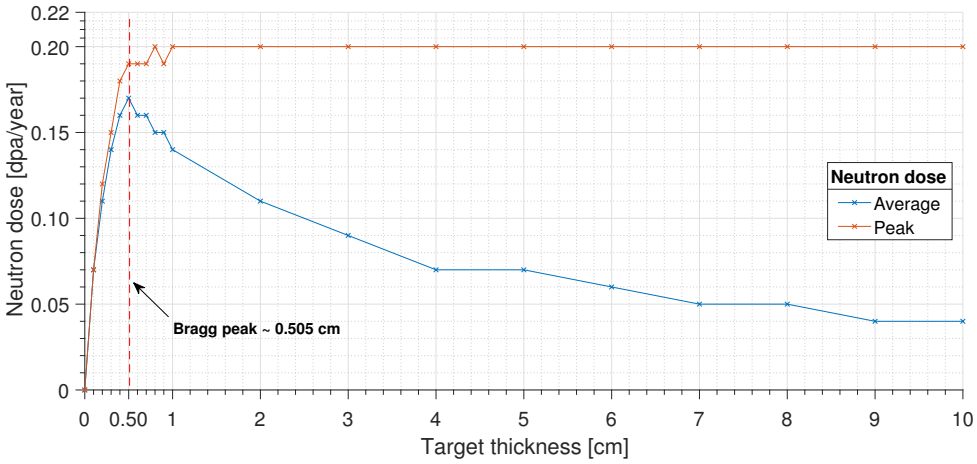

Figure 4.24: Average and peak neutron displacement doses (dpa/year) as a function of varying target thickness for the simple geometry.

Finally, it was also tried to increase the neutron damage by reaching greater fast neutron densities inside the tantalum target. Therefore, the moderator material was substituted with uranium (see fig. 4.25), which is well known to be a good reflector for fast neutrons.

As uranium is not available in the FLUKA default material library, it had to be defined as a new material (defined with 0.72% of U-235 and 99.28% of U-238).

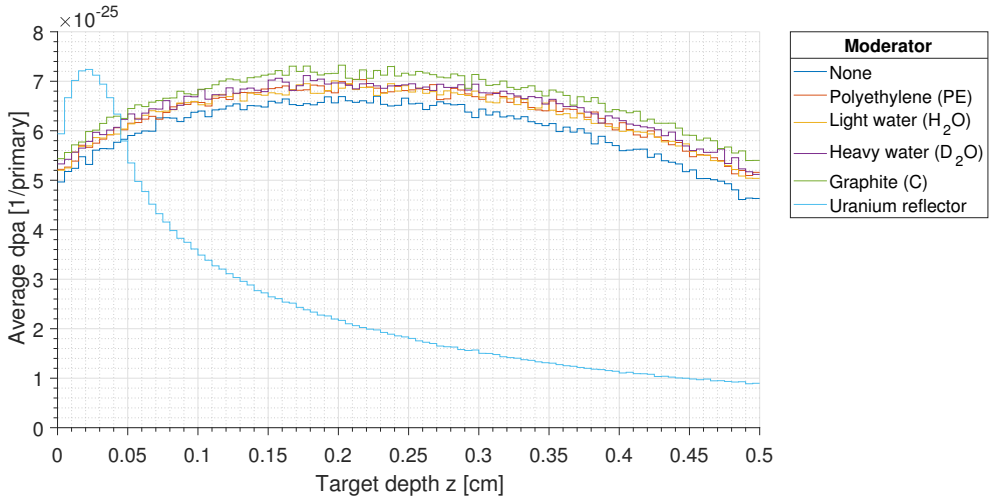

Figure 4.25: Influence of a uranium reflector on the neutron atomic displacements.

5. Results and discussion

In this chapter the outcomes of all simulations (see chap. 4) and their meaning will be discussed in a broad context. Therefore, graphical results presented in chapter 4 are complemented with corresponding numerical data and intercode comparisons between the codes are carried out.

The discussion of results first of all exclusively focuses on physical and code specific aspects and explains all the findings based on the theory provided in chapter 2. A critical comparison of obtained numerical results with the literature and subsequent classification of the damage is done in the frame of a final damage assessment.

This damage assessment also includes considerations of major frame conditions concerning the operation of the target and thereby accounts for non-standard deviations from the ideality assumed in the simulations. In particular, the influence of the reached temperature in the target on the radiation damage is discussed as well as the activation of the target is taken into account.

Finally, a rough and cautious qualitative estimation about the target's expected lifetime based on all simulations and corresponding results is done.

5.1 SRIM simulations

The numerical outcomes from the SRIM simulations are given in table 5.1, details of the various calculation methods are described within chapter 3 (see table 3.2).

As SRIM generally provides many different routes of damage calculation to obtain dpa values, as expected a strong fluctuation in the values between the different methods is visible for the same irradiation condition (time, flux). The nature of the BCA and the KP formalism as well as the absence of highly accurate reference values from experiments or MD simulations excludes the statement that one of these values is definitely right or wrong or superior over the others [67].

Table 5.1: Numerical results from the SRIM simulations. The calculation methods of depicted values are described in chapter 3 in details.

Calculation method	R_d [10^{-6} dpa/s]		Annual dose [dpa]	
	Average	**Peak**	**Average**	**Peak**
Plot (a) & eq. 3.1	0.33	-	10.26	-
Plot (a) & eq. 3.2	-	1.29	-	40.65
Plot (b) & eq. 3.3	-	0.91	-	28.54
Plot (b) & (c) & eq. 3.3	-	1.42	-	44.66

Endangered area

Figure 4.3 clearly defines the back of the target as the most endangered zone with the highest number of target displacements. If the target experiences critical harm associated with atomic displacements, the damage evolution will most probably originate at the back.

Figure 4.1 shows that the protons increasingly lose energy in inelastic reactions with electrons as they reach deeper layers in the target, i.e. become slower. At the first sight this is unexpected, as the electronic stopping for charged particles usually dominates at high ion energies and velocities [148], hence near the entrance area in a material. However, the actual stopping curves strongly depend on the mass of the particles relative to that one of the material atoms and for light ions as protons this behavior has been observed [149].

Nevertheless, the nuclear energy losses responsible for atomic displacements become increasingly important as the ions slow down and peak at lower energies near the Bragg peak. If one assumes the energy transferred to recoils in figure 4.4 to be the total nuclear deposited energy (excluding energy transfers to phonons) and scales the value of $\sim 10.11 \cdot 10^{-4}$/eV/Å/Ion with the total of 15.000 ions, one obtains an energy deposition of ~ 15 eV/Å. Compared to ~ 3.5 eV/Å of electronic energy losses in figure 4.1 at the back of the target that is high.

The increasing nuclear energy deposition is the reason for why the amount of produced Ta recoils increases towards the back of the target (see fig. 4.1) and hence ultimately also the number of atomic displacements.

Review of the calculation methods

In figure 4.3 it can be seen that the number of replacement collisions increases towards the back of the target. Though one could simply explain that with the increased extent of available vacancies and recoils, this suggests that the phenomenon plays a crucial role at lower proton energies, where nuclear stopping dominates.

The proton displacement cross section for tantalum is observed to rise towards lower ion energies [150]. Hence, with regard to chapter 2 the average mean free path length λ_d (eq. 2.6) between atomic collisions decreases, ultimately leading to an increased energy and defect density, favoring replacement collisions. Also many-body collisions during thermal spikes will increase the number of replacement collisions, but as the BCA can only depict binary collisions this is not accounted for in SRIM.

Figure 4.4 allowed to calculate peak values for the number of displacements based on the nuclear deposited energy. As described in [67], additional consideration of energy losses due to phonons shall result in an improved calculation. However, as already mentioned, phonon production is a subthreshold reaction below E_d, and hence the meaningfulness of this method should be reviewed carefully. Additionally, usually it is the released binding energy E_l ($< E_d$) of a recoiling atom being displaced that leads to phonon creation [125]. As consideration of phonon creation leads to a large increase in damage values (see table 5.1), hence this route should probably not be taken as the prime choice.

Contrasting to FLUKA simulations, one should be aware that any calculation of peak values based on the calculation methods used in SRIM assumes damage values to be homogenously distributed along the whole target thickness. Though the user cannot define volumes but just layers, the evaluation of values however is still only related to the atoms present within the considered bin.

As SRIM generally lacks the prediction of nuclear reactions [125] resulting in the formation of residual nuclei, the accumulation and displacement of transmuted atoms is not accounted for. Consequently, also atomic displacements due to radioactive decay processes are totally neglected (as also in FLUKA).

As any method used for the estimation of displacements per atom that is based on the BCA and the original KP equation (eq. 2.28), SRIM overestimates the damage. The incapability of the BCA to depict many-body collisions and associated defect recombination processes, especially during thermal spikes, inherently limits the precision of SRIM values.

Large uncertainties in the electronic stopping powers utilized in SRIM have been reported [151]. These may then affect the qualitative outcome of damage assessments as well, since nuclear and electronic stopping are always competing processes.

In [122] deviations are reported between SRIM values obtained based on various processing methods of deposited energy and collisional events, i.e. vacancies obtained by the VACANCY.txt file. Stoller et al. propose methods based on deposited energy to be more reliable. However, information about vacancies from that file have not been used in the frame of this thesis for damage calculation purposes.

5.2 FLUKA simulations

The numerical results for the annual displacement doses of all particles (Tot.), protons (p^+) and neutrons (n) obtained with the FLUKA internal *DPA-SCO* method are given in table 5.2. Since the presence of moderators did not exhibit significant influence on the displacement behavior, values have been averaged over all different moderators. The data of each single moderator can be taken from appendix B.20 and appendix B.21 additionally gives the damage rates R_d corresponding to the HBS flux.

Table 5.2: FLUKA numerical *DPA-SCO* results for the annual displacement dose. As the influences of all moderators were negligible, average values were taken. The complete data for every moderator is given in appendix B.20.

Moderator	Annual dose [dpa]					
	Average			Peak		
	Tot.	p^+	n	Tot.	p^+	n
No	4.43	4.20	0.17	12.06	11.92	0.19
Yes	4.44(1)	4.20	0.18	12.07	11.93(1)	0.20(1)

Correlation between deposited energy and displacements

Owing the fact that atomic displacements are a strong function of deposited energy, figure 4.7 and 4.8 reveal a great similarity between these two quantities, particularly emphasized in figure 4.9 with both quantities plotted together.

Additionally, the majority of energy deposition (see appx. B.22) and atomic displacements (see table 5.2) is due to protons, completely unaffected by moderators. As secondary protons are negligible (see fig. 4.12), figures of both energy deposition and atomic displacements hence exhibit the shape of a classical ion stopping curve with a Bragg peak at the end.

In comparison, atomic displacements rise much steeper to a thinner peak. This is mainly attributed to the fact, that the nuclear deposited energy becomes dominant near the Bragg peak where the ions are slowed down. The Bragg peak of the energy deposition is broader since also the electronic losses increase towards the back of the target, as demonstrated in the SRIM simulations (see fig. 4.1).

In order to obtain a clear relationship between energy and displacements, the amount of average dpa per primary was plotted as a function of the deposited energy, as depicted in figure 5.1.

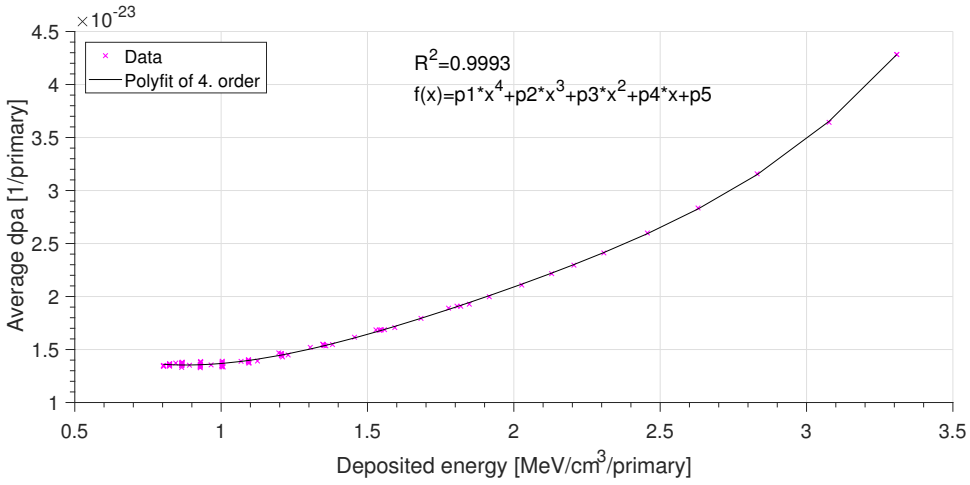

Figure 5.1: Correlation between the deposited energy and the number of atomic displacements. The displacements are due to all particles and the correlation was done for the case of the simple geometry and 70 MeV primary proton energy.

The data points were fitted with a polynomial fit of 4th order, indicating that there is no linear dependence. Rather, with increasing energy the extent of displacements grows overproportional. This is reasoned in the fact that the whole deposited energy is plotted and nuclear energy losses are favored as the particles are slowed down by depositing a growing amount of energy. Though linear behavior could be expected in the case of NIEL, anyway at some energy a saturation character would appear beyond which no additional displacements take place (see chap. 2).

The benefit of such a correlation would be a fast and conservative estimation of the amount of displacements if one knows the amount of deposited energy. Extrapolation of the data set would then also allow to make estimations of even lower or higher energy depositions, though one should cover a greater range of energy deposition (by shifting the Bragg peak) before to increase the reliability of extrapolations.

Major damage contributors

As depicted in figure 4.10, charged particles dominate in the creation of atomic displacements by far. In addition, a detailed investigation of a huge variety of charged particles (see fig. 4.11) impressively defines protons to be the main damage contributors, consistent with the numerical results given in table 5.2.

A differentiation of protons as a whole into primary and secondary protons also revealed that the contribution of secondaries is negligible ($\sim$ 0.57% at 70 MeV). Protons are pointed out as the main damage contributor also in [152] and with special regard to tantalum in the Ta spallation target of the TRADE facility [153].

As expected, from the neutral particles neutrons dominate in atomic displacements (see fig. 4.13). The contribution of photons is totally negligible as photons generally have to release particles via photonuclear reactions, with high threshold energies.

As radioactive decay processes were not activated, only the photons released in relaxation processes of compound nuclei are considered.

Consideration of the neutron spectra with and without moderators and beamstop (see fig. 4.14, 4.15, 4.16 and appx. B.6) shows the influence of the moderators, namely an increase of the neutron population in the Ta target. As shown in the energy divided neutron spectra (figure 4.17 and appx. B7 to B.11) the density of neutrons inside the target falls down with energy, i.e. fast neutrons dominate.

The unmoderated target yields only fast and resonance neutrons, the moderation mostly increases the amount of low energy neutrons incapable to induce displacements since their energy is below E_d, indicated by negligible changes in atomic displacements (see fig. 4.20). Appendix B.5 also shows that the neutron production starts at $\sim$ 10 MeV and is quite well maximized with an energy of 70 MeV.

Spatial damage distribution

Radial and axial binning of energy deposition and atomic displacements enabled to get an impression of the 2-dimensional damage pattern (see fig. 4.19 and 4.21 and appx. B.15 to B.19).

Besides the great similarity between deposited energy and atomic displacements again, for protons and the total displacements one can observe a radial homogenously distributed pattern at every depth. Based on the ion trajectory pattern obtained with SRIM (see fig. 4.2), one would not have expected such a pattern. However, in SRIM a point source has been used whereas protons were emitted homogenously within a cylindrical volume in the FLUKA simulations.

For neutrons, the amount of dpa peaks approximately in the middle of the target with and without moderators and beamstop (see fig. 4.19 and 4.21), indicating that the protons are slowed down there to an energy corresponding to the maximum ^{181}Ta(p,xn)W reaction cross section. Radially, and also axially, the extent of damage generally decreases towards the outer surfaces. Therefore, in contrast to the protons, the 2-dimensional damage pattern of neutrons looks like a "cloud".

In the spatial damage patterns the binning did not distinguish between the top and bottom side of the target. In the case of the homogenous source however there is no reasonable misinformation.

Validation of the neutron damage

At 70 MeV primary proton energy the neutrons' contribution to average displacements is $\sim$ 4% and to peak displacements even less with $\sim$ 1.5%, entirely regardless if a moderator and beamstop are taken into account. This damage pattern was also shown for the Ta spallation target in the TRADE project [153].

A negligible contribution of neutrons in atomic displacements was unexpected as close impact collisions are not hindered by coulomb repulsion as in the case of charged particles. Furthermore, it is well known that neutrons can degrade RPVs substantially with high amounts of atomic displacements [154].

Also, the effect of every single moderator is totally insignificant, although the density of neutrons inside the target carrying a kinetic energy $> E_d$ according to the neutron spectra is slightly enlarged. In order to explain this surprising damage pattern of the neutrons and to find a reason, several systematic validation simulations have been performed.

First of all it was tried to increase the extent of displacements due to neutrons by increasing the moderator radius (see fig. 4.23). Although in principle both the average as well as the peak dose tend to rise with increasing radius, the absolute influence is totally negligible. Anyway, increasing the chosen radius of 10 cm will not tend to increase the neutron dose, implying that the dimensions are already optimized for a perfect neutron moderation in the HBS project.

The influence of the target thickness was also investigated (see fig. 4.24). The average as well as the peak dose both rise steeply within the first 0.50 cm, as expected since source protons can interact more frequently with tantalum atoms to produce neutrons. Beyond that thickness the average dose drops down, whereas the peak dose remains constant. The curves imply that the major damage occurs at a thickness just sufficient to completely stop the primary ion beam.

Further enlargement of the thickness will decrease the average dose since the protons as main damage contributors will not penetrate deeper but the ($\sim$ same) number of displacements has to be related to more target atoms. The peak dose remains constant, as it is always evaluated for a local area regardless the actual target thickness. For a constant primary proton beam energy and minor contribution of neutrons, this area is always located around the Bragg peak.

As fast neutrons, carrying the highest amount of kinetic energy, should induce potentially most displacements, the moderator was also substituted by a uranium reflector (see fig. 4.25).

As uranium is generally well known to be a proper reflector for fast neutrons, it was thereby tried to increase the fast neutron population inside the target. Actually reflected fast neutrons induced some displacements near the front side of the target, but the effect was minor again.

For an efficient displacement of atoms, the spatial frequency of displacements should be high, i.e. the mean free path length between collisions should be small. Therefore, the mean free transport path length λ_{tr} was plotted as a function of the neutrons' energy (see fig. 5.2).

With a *LOW-NEUT* card a printing flag was set in the WHAT(4) field, which gives all total cross sections of all 260 neutron energy groups (1E-11 to 20 MeV) for all defined media in the FLUKA output file. The macroscopic transport cross section Σ_{tr} was calculated as the product of this total cross section and the number density of tantalum. The mean free transport path length λ_{tr} was then in turn calculated as the inverse of the macroscopic cross section, according to equation 2.6.

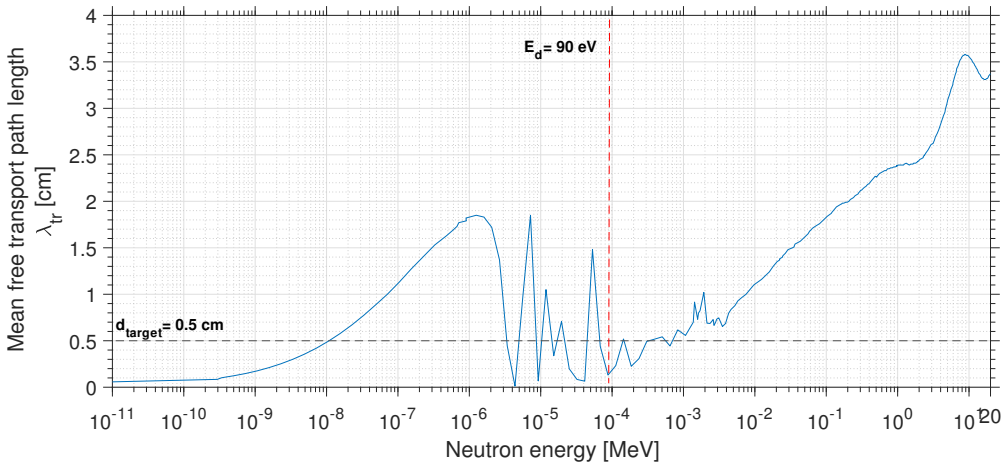

Figure 5.2: Mean free transport path length λ_{tr} of neutrons inside the tantalum target.

Undoubtedly, figure 5.2 distinctly shows that the great majority of all neutrons traverses the target without undergoing even a single collision. Only in the resonance region around E_d a few neutrons are able to induce displacements. Cold neutrons undergo more interactions, but their energy is too far below E_d.

Finally, neutrons' contribution to atomic displacements is totally negligible due to their high pathlength λ_{tr} between collisions. It does not matter how big the neutron density is or gets enlarged with surrounding moderators, the neutrons obviously just "fly" undisturbed through the target. Hence, even if an additional consideration of a surrounding reflector in the utilized geometrical model results in a further increase of neutrons inside the target it would not add here any value. As λ_{tr} strongly depends on the element besides the energy, the neutron damage pattern may look completely different for another target material.

In the case of the tantalum target designed for the HBS project however neutrons are totally negligible, at least with regard to atomic displacements.

NIEL dpa and comparison to SRIM

The numerical results for NIEL dpa values are given in appendix B.23. A comparison with the FLUKA internal *DPA-SCO* method obtained values (see table 5.2) can be assumed to compare the KP and NRT model qualitatively, though in the original KP model the whole energy losses serve as input (see chap. 2).

As expected, the KP model (NIEL) yields higher values as the NRT model. The NIEL dpa are basically in the range of the SRIM values (see table 5.1), in contrast to the FLUKA values based on the NRT model. This highlights again that the difference between FLUKA and SRIM is reasoned in the physical models.

The consideration of the displacement efficiency η (= 0.8) in the *DPA-SCO* method accounting for defect recombination processes decreases the number of displacements compared to SRIM. A further decrease is done, as η is actually implemented into FLUKA as a function of the kinetic particle energy above $\sim$ 1-2 keV [103]. Hence, η is not constant but variable and migration and recombination of FPs are taken into account in an improved manner. In the "manual" calculation by the NIEL this feature is not taken into account, also resulting in an increased amount of displacements obtained by this route.

5.3 Final damage assessment

The ultimate fate of any damage parameters obtained by intensive simulative methods is a prediction and estimation of the lifetime for components exposed to strong radiation fields. Therefore, the final objective and intention of this thesis is to make a statement about the tantalum target's expected lifetime.

As already declared in the introductory part of this work however, the literature yet lacks reliable reference values beyond one can surely assume the material to be destroyed. Even if such values would exist, a completely sole reliance on simulative dpa values could still pose a risk.

In order to make rational conclusions as meaningful as possible, the lifetime estimation is done in a qualitative way. For this purpose, the existing literature was scanned thoroughly to extract rough hints about the expected lifetime. In harmony with that, a minimum lifetime is proposed rather than a maximum one.

A qualitative and precious damage assessment also includes considerations of special frame irradiation conditions. Hence, the assessment outcomes will also be related to the conditions prevailing in the HBS project.

No doubt, although dpa is the standard measure in radiation damage analyzes, a numerical quantity alone lacks to provide information on the actual damage pattern on a microscopic scale. Regarding this circumstance, limitations and drawbacks of a sole reliance on displacement values will be clarified as well as the use of further investigations by other means is presented and recommended.

Qualitative literature review

Overall, the available literature concerning radiation damage investigations of tantalum based on the dpa quantity is quite sparsely and limited. However, as it is

frequently used as spallation material and also regarded as a plasma-facing material [155] and solid target for neutrino production [156], a few data exists. In addition, tungsten (Z=74) behaves quite similar as tantalum and is often alloyed or coated with tantalum (solid solution) to reduce corrosion-erosion effects [157–162]. Investigations of such Ta-clad W targets may at least partly also reflect the radiation damage behavior of tantalum.

Proposed in [163], as a very general rule of thumb, for most solids the lifetime dose against radiation damage by protons can be taken as $\sim 10^{22}$ p^+/cm^2. Related to the surface area of 100 cm^2 in the HBS target this would mean that the target can withstand a total of 10^{24} primary source protons. Considering the average beam current of 1.43 mA would hence propose a lifetime of roughly 3.5 years.

Nevertheless, this should be taken only as a very coarse estimation since specific irradiation conditions such as the energy of the protons are not further accounted for. Depending on the geometrical dimensions of the target and Bragg peak location, different lifetimes should be expected. Also, though minor, secondary protons might also reduce that time.

A very suitable possibility to estimate the lifetime is given by the pulsed spallation source ISIS (Spallation Neutron Source at Rutherford–Appleton Laboratory), as they used tantalum for a long time and still use it nowadays as cladding for W targets. In an extensive test program for the lifetime of structural components of spallation targets, Chen et al. investigated spent target components from spallation facilities [164, 165]. Based on investigations of the irradiation-induced alterations of mechanical properties, the testing also included a spent tantalum target of ISIS.

In several irradiation campaigns over six years, this target was irradiated with 800 MeV protons up to a maximum fluence of $1.7 \cdot 10^{21}$ p^+/cm^2 ($\sim$ 1.7 Ah) below temperatures of 200°C. Microhardness measurements, three-point bending tests, tensile tests and optical micrography at RT and 250°C revealed radiation hardening accompanied with a drop in ductility already below doses of 0.6 dpa.

However, remarkably the tantalum target retained a very high ductility even after a displacement dose of **11 dpa**. Scanning electron microscope (SEM) investigations revealed typical ductile fracture surfaces and between 0.6 dpa and 11 dpa the strain-to-necking ratio remained constant.

In the work above by Chen et al., the calculated displacement damage of 11 dpa refers solely to protons [165], hence neglecting neutrons. Therefore, in [166] Byun and Maloy report the irradiation of a tantalum target from ISIS exclusively by neutrons in the high flux isotope reactor (HFIR) at the Oak Ridge National Laboratory (ORNL) at an irradiation temperature of 100°C. Already at a dose of **0.14 dpa** tensile tests at RT and 250°C showed that the tantalum target experienced embrittlement.

In the same measurements, also a Ta-10W (90% Ta and 10% W) specimen has been tested. The probe broke at a dose of 25.2 dpa with minor necking strain, indicating a substantial loss in ductility.

Also at ISIS, the 800 MeV synchrotron provides protons for two Ta-clad W target stations (TS) [167–169]. In neither of them the lifetime is limited due to radiation damage. In TS1 (160 kW power) the lifetime is $\sim$ 4-5 years and only limited by a thermocouple failure, whereas TS2 (32 kW power) has a lifetime of $\sim$ 1.5 years, limited to release of activation products into the cooling water circuit (probably a welding failure).

Ipatova et al. found out that radiation induced voids in pure tantalum, irradiated with 3 MeV protons, order and grow at 0.25 dpa (fluence of $2.8 \cdot 10^{18}$ p^+/cm^2) [170]. As voids are favored places for the accumulation of reaction products (see chap. 2), especially mobile hydrogen and helium, hence blistering and swelling can start to continuously degrade the mechanical integrity.

Yasunaga et al. observed that the swelling however is negligible below $\sim$ 730°C and 20 dpa in the case of heavy ion irradiation [171]. Wiffen also determined the swelling of tantalum after neutron irradiation to be negligible below 425°C [172].

In another work, Ipatova et al. investigated the effect of alloying content on the defect structure formation and evolution in the Ta-W system [173]. Studies of pure tantalum, irradiated with 3 MeV protons and 9.5 mA beam current for 36 hours at $\sim$ 350°C, showed that radiation induced hardening starts to occur roughly after irradiation begin, i.e. at doses $\leq$ 0.3 dpa. Dislocation loops as the starting point for the evolution of complex damage patterns are reported to occur in the same dose region but only at elevated temperatures of 700°C.

Villagrasa-Roussel et al. obtained simulated dpa values for a tantalum spallation target with conditions as proposed for the TRADE experiment [174]. The data for four different primary proton energies (140, 300, 500 and 1000 MeV) was fitted and extrapolated to the origin in order to derive a value corresponding to the HBS energy of 70 MeV (see appx. C.1). The beam current of 0.14 mA was scaled to 1.43 mA, resulting in a dpa value of 107. As expected, this value exceeds all obtained values due to occurance of spallation reactions. Unfortunately, no proper experimental data about the TRADE project is evident in the literature.

Rough lifetime estimation

A definitive and precise statement about the expected target's lifetime, solely based on simulative damage values, is neither possible nor recommendable. For this purpose experiments are indispensable. However, based on the literature review above it is possible to give a rough and cautious estimation about the **minimum lifetime** τ_{min} that could be reasonably expected.

The reference values of **11 dpa** and **0.14 dpa** obtained from Ta targets operated at ISIS should be reasonable, especially in the case of the 11 dpa value as the extent of damage inside this target must be assumed to exceed that one in the HBS target due to spallation processes (800 MeV proton energy). Furthermore, it is reported that this target was not replaced due to radiation damage. Rather, ISIS performed a change to Ta-clad W targets for reasons of increased neutron output, reduced decay heat and enhanced thermal conductivity [168]. Hence, it can be assumed that the target probably would have been able to withstand even higher doses.

Although the contribution of neutrons to displacements is negligible in the HBS project compared to that one of protons, it seems that even small doses might be sufficient to cause substantial changes in material properties. However, Byun and Maloy marked the mentioned embrittlement in [166] as premature. One should be aware that the target was annealed for 2 hours at 1200°C before irradiation, hence accumulation of oxygen might have weakened the material and be the reason for the early embrittlement.

The minimum lifetimes are estimated based on the ISIS proposed dpa values (i.e. 11 and 0.14 dpa) and the obtained average damage rates R_d (dpa/s), as depicted in table 5.3. Calculation of τ_{min} based on peak rates would surely lead to smaller lifetimes, but for the qualitative lifetime estimation it was decided to consider the complete target volume as peak values anyway "only" consider a small region which may degrade the representativity of results.

Table 5.3: Estimations of the expected average minimum target lifetime τ_{min}.

Reference	**Minimum lifetime τ_{min}**			
	SRIM		**FLUKA**	
[dpa]	**[a]**	**[Ah]**	**[a]**	**[Ah]**
11	1.06	13.24	2.48	31.12
0.14	-	-	0.82	10.30

Further, FLUKA values of the *DPA-SCO* method have been used since this is superior over the presented alternative route of the NIEL dpa values. Apart from that, in contrast to *DPA-SCO* values the latter ones were obtained by processing with the original KP formalism, which overestimates the produced damage.

Values corresponding to 11 dpa were obtained based on total damage rates, whereas those based on 0.14 dpa were calculated with the damage rates of neutrons. Values are given in units of years (a) and units of total accumulated primary proton beam charge (Ah) in the target (see table 5.3).

As expected, SRIM proposes a shorter value for τ_{min} than FLUKA due to the differences in the physical dpa models. However, since the NRT model reflects the

damage more realistic one has to assume the FLUKA proposed values to be more accurate and reliable.

Influence of frame irradiation conditions

A meaningful lifetime estimation regarding radiation induced material damage by atomic displacements should always consider actual irradiation conditions. With respect to these conditions, the temperature exhibits the most notable and dominating influence on atomic displacements. As the HBS project yet lacks data of experimental investigations of activated material, the influence of predominant irradiation conditions is accounted for in a qualitative way.

In particular, it is of major interest for the HBS group to know whether limiting radiation damage occurs before or after the target has to be replaced by another one due to material activation.

Due to the intense exposure of the tantalum target with protons and produced neutrons, a huge number of radionuclides will be produced over time (see appx. A.3). As the HBS however will be operated at an energy insufficient to induce spallation reactions (i.e. < 100 MeV), these radionuclides belong to a few elements only with atomic numbers around that one of tantalum ($\sim$ Z=73). Indeed, various isotopes of tantalum (Ta), tungsten (W), hafnium (Hf) and lutetium (Lu) are formed, with the ^{182}Ta isotope being the most relevant for radiation protection purposes due to the highest activity ($\sim$ PBq).

Although it is not clear at the moment how often the target has to be replaced with regard to activation limits, the activity of the HBS target is in the same order of magnitude of the Ta-clad W target of the ISIS facility [175]. At a total exposure of 1.94 Ah with 800 MeV protons it was replaced after approximately 540 days.

With respect to appendix A.4, in the HBS a total activity in the range of PBq is already reached within the first 30 days of continuous operation ($\sim$ 1.0 Ah). Assuming the target has to be replaced after that time span due to radiation safety and disposal issues, with regard to table 5.3 it is clear that no critical radiation damage would be expected to occur before. Even if the target will be replaced one or two times a year, the danger of critical radiation induced damage should still be minor as values in table 5.3 just reflect minimum lifetimes.

As mentioned in chapter 2, the extent and evolution of damage creation is greatly affected by temperature. In appendix A.5 the maximum temperature inside the target is plotted for a 100 mA pulsed proton beam at 24 Hz. Accordingly, the maximum temperature reached will be $\sim$ 120°C and the average temperature is determined to be around $\sim$ 65°C.

As a refractory metal and with regard to the melting temperature T_m ($\sim$ 3000°C), the dominant effect of the radiation will be radiation hardening with associated

reduction in ductility (up to $\sim 0.3\ T_m$ [176]), starting already at roughly 0.1 dpa. Irradiation creep and void swelling are not expected to limit the lifetime substantially as they dominate between 0.3 and 0.6 T_m [176]. Given these low temperatures and a clever internal cooling design (see appx. A.6), a change in the crystal BCC structure of Ta (α-phase) can probably be excluded, also excluding associated changes in the TDE [177] or other fundamental physical properties.

However, one should be aware that simulations of the temperature inside the target yet are subject to strong simplifications. Precise statements about the maximum temperature can only be done when the beam diameter and the final grid speed are known. Therefore, the maximum temperature could be locally higher than 120°C.

Limitations of the dpa quantity and future recommendations

Although dpa is the standard indicator for radiation damage, this purely theoretical quantity lacks to be a proper measure for reflecting the actual damage patterns on a microscopic scale. The absolute numerical dpa value itself gives no insight into the material's microscopic structure and hence does not say anything about the damage on an atomic scale. Rather, the meaningfulness of radiation damage assessments should be supplemented by various experimental methods, deriving a relationship between dpa and macroscopic quantities.

The reason for the failure of any component exposed to intense radiation fields is not the displacement of atoms itself, but the associated deviations in the crystal structure induced. These alterations evolve, starting from the simple PDs of atomic displacements, to more and more complex defects ending in spatial defect clusters (see chap. 2 and fig. 2.2). Consequently, finally macroscopic changes become visible.

The actual damage pattern on a microscopic level is a strong function of the frame irradiation conditions applied, and as the displacement process underlies a random nature coupled with a certain probability (cross section) like radioactive decay, a prediction of damage is generally impeded. The absolute number of atomic displacements does not reflect the microscopic damage, the actual damage pattern can only be assessed by means of advanced microscopic techniques such as transmission electron microscopy (TEM) or scanning electron microscopy (SEM) [178–181]. Application of such methods allows to identify doses (dpa) where critical defect structures start to emerge.

Nevertheless, despite the mentioned drawbacks the dpa quantity has established to be the standard indicator for radiation induced material damage within the nuclear community. That is rightly, since its great meaningfulness is undisputed as it ultimately allows a correlation to macroscopic measurable properties, which are a strong function of dpa. Hence, knowing threshold values for these properties enables to make a statement about a material's lifetime since the irradiation time can be always extracted from dpa values.

In principle, the maximum dpa value a material can tolerate at certain irradiation conditions might be extracted from an extensive row of experiments. Measuring a macroscopic property (e.g. tensile strength) after different irradiation times respectively doses (dpa) might reveal a trend in the data points, allowing to fit and extrapolate to that dose where the material is expected to fail.

Therefore, in order to make precise estimations about the maximum lifetime of a target, experimental investigations of irradiated tantalum under realistic conditions are indispensable. Unfortunately, the investigation of irradiated materials is difficult due to material activation and usually requires remote handling in special environments like hot cell facilities. Fortunately, the research centre Jülich itself in principle has the necessary infrastructure, as the experiments performed with the ISIS Ta target were performed by Chent et al. in Jülich [164, 165]. However, meanwhile such experiments might be problematic at the research centre Jülich since the hot cell facility is primarily used for dose measurements of dismantled parts of the AVR and DIDO reactors. When the reactors are completely dismantled, the hot cell facility itself will be dismantled as well, leaving a green meadow.

A challenge in a row of such experiments will be the determination of the critical property, i.e. the property responsible for the target failure. One might compare this with a water filled barrel with planks of different height. The water level is limited by the shortest plank. In analogy to that, the target's lifetime will be limited to the most critical material property. For example, it does not matter if the induced mechanical stress inside the target is far below a critical value for failing if blistering for example destroys the mechanical integrity too early.

Although the literature suggests that the phenomenon of void formation and gas accumulation is not of major concern in the case of tantalum and the irradiation conditions foreseen to be applied, especially at the comparatively low predicted operating temperatures, the HBS group suspects the accumulation of hydrogen gas in the target due to the intense proton bombardment as a possible failure mode. Therefore, and as it was not accounted within this thesis, future investigations should examine the gas accumulation. Again, if one knows how much hydrogen the target can take up, one can correlate the gas uptake with the atomic displacements and thereby determine a critical lifetime of the target.

The efforts for measurements of highly activated probes might also be reduced if one irradiates tantalum probes at lower energies for shorter times. One might be able to develop a model, on which one can draw conclusions about the expected damage at higher energies. Such corresponding radiation damage test facilities actually already exist [182]. Typically, tandem ion accelerators with ~ 5 MeV ion energy are used. Such test stations are quite compact and might be also built up with small efforts around the great COSY accelerator at the research centre Jülich.

6. Conclusion

In the frame of this thesis, the expected radiation induced material damage inside the tantalum target designed for the Jülich High Brilliance Neutron Source project (HBS) was investigated by means of simulative methods for the first time. Simulation software packages utilizing the Monte Carlo approach, FLUKA and SRIM, have been used to yield information on atomic displacements in units of displacements per atom (dpa). Based on this quantity as a well accepted and powerful standard indicator for radiation damage in condensed matter together with an intense literature review, ultimately cautious and qualitative estimations on the minimum lifetime τ_{min} of the target that can be reasonably expected were drawn.

In the HBS project the primary proton beam of 70 MeV energy is not fully stopped inside the target but rather closely behind within a thin layer of water, the beamstop. This represents a technical design improvement as the deposited energy and hence the damage inside the target is reduced without being at large expense on the neutron yield. Previous simulations with SRIM clearly define the back of the target to be the most vulnerable region, since target displacements and hence the density of tantalum recoils as a consequence of increased nuclear energy losses were found out to be highest within this area. If the target suffers critical damage, it will most likely originate from the rear region. FLUKA simulations confirmed that damage pattern, although there is the possibility for protons to penetrate deeper as the beamstop by lateral scattering into a surrounding thermal moderator.

Whereas SRIM simulations reflect the damage with regard to protons and tantalum recoils, FLUKA simulations enabled the possibility of filtering for different particle types. An investigation of a huge diversity of different charged and uncharged particles in the context of a characterization of the hadronic collision cascade clearly revealed charged particles to be the main damage contributors. From these, protons, mainly belonging to those from the primary ion beam, dominate by far. Secondary protons produced via nuclear reactions were found out to be negligible, justifying no further differentiation between primary and secondary protons with regard to atomic displacements. In contrast to that, electrically neutral particles deliver only a very minor contribution to atomic displacements, with neutrons being the most relevant particles.

The strong connection between deposited energy and atomic displacements was also figured out in FLUKA simulations. Although indeed only nuclear energy losses in elastic collisions lead to atomic displacements, in the philosophy of preliminary overview simulations the whole energy deposited by all particles was scored. Fitting the extent of displacements as a function of deposited energy enabled to reveal a relationship between these two quantities. With increasing deposited energy the number of displacements grows overproportional. Linear behavior was not observed as the whole energy including electronic energy losses has been used. With increasing energy deposition protons are slowed down and nuclear energy losses inside the target become dominant, hence the potential for displacements grows.

In the frame of the FLUKA simulations, the main simulative work was dedicated to the displacements caused by neutrons produced in nuclear reactions. The influence of different thermal moderators was investigated meticulously with the addition of corresponding neutron spectra. Regardless the constitution of the moderator and its physical dimensions, the contribution of neutrons was totally minor in comparison to that one of protons. Although a splitting of the neutron spectra into different energy regions along the target in principle demonstrated an increase in the neutron density inside the target, these neutrons' energy was mostly too low to induce displacements.

As a minor contribution of neutrons was not expected and in order to find a reason, several validation simulations were performed. Neither increasing the target thickness, the moderator's radius nor substitution of the moderator by a natural uranium reflector to increase the fast neutron population inside the target were sufficient to explain the results. Plotting the mean free transport path length λ_{tr} between the interactions of neutrons as a function of the neutrons' energy finally revealed the reason for the negligible contribution; λ_{tr} usually exceeds the thickness of the target. Consequently, the majority of neutrons just "fly" through the target without any interactions and hence no significant contribution in atomic displacements.

Compilation of numericial results (annual doses in dpa/year) showed large deviations between values obtained with SRIM, depending on the calculation method. SRIM values have been obtained by running the full damage cascades mode, which also tracks recoil atoms until their kinetic energy drops below the threshold displacement energy E_d. There exist many ways to process the data obtained by SRIM to extract dpa values, but since the literature lacks reliable reference values for many materials yet it is somewhat unclear what method depicts the reality most precisely. Anyway, consideration of nuclear energy losses leading to phonon production was not defined as useful as these processes take place at energies below E_d.

Intercode comparisons between FLUKA and SRIM also revealed large deviations, with FLUKA values being smaller than those obtained with SRIM. These deviations are mainly reasoned in the differences of the physical models, on which the calculation methods are based. SRIM values are obtained based on the original

KP formalism, which totally neglects defect recombination processes and hence inherently leads to an overestimation as the BCA is incapable to depict many-body collisions in an appropriate way. In contrast, FLUKA values are based on the NRT model, which accounts for recombination processes.

Further enhancement of FLUKA values obtained with the FLUKA internal *DPA-SCO* method is done as the displacement efficiency η becomes a function of kinetic particle energy above $\sim$ 1-2 keV. The differences between the KP and NRT model were also evident by consideration of dpa values obtained with the energy restricted NIEL, scored in FLUKA. The NIEL was processed with the original KP formalism, and similar to SRIM it overestimated the amount of atomic displacements compared to the FLUKA internal *DPA-SCO* method.

Since it is neither possible nor recommendable to propose a reasonable value for the maximum expected lifetime of the tantalum target solely based on theoretical and simulative dpa values, the literature was scanned very thoroughly to get some clues for a qualitative estimation. Although the literature concerning radiation induced material damage in tantalum is quite sparsely, appropriate reference values have been found on which a rational and reasonable estimation of an average minimum lifetime τ_{min} of the target was possible. Since FLUKA obtained values are based on the more realistic NRT model, these values should be taken as superior and prime choice over the smaller value proposed by SRIM.

The ISIS reference value of 11 dpa considers damage creation due to protons, whereas the value of 0.14 dpa exclusively accounts for neutrons. The reference value of 11 dpa should be reasonably taken as more realistic than the 0.14 dpa reference, as it is very likely that the mentioned early embrittlement there was premature due to oxygen uptake after previous annealing. Anyway, protons dominate by far in atomic displacements, whereas neutrons show only a very minor contribution. Therefore, assuming a continuous full power operation without interruptions, it is reasonable to assume a total minimum lifetime of the tantalum target of $\boldsymbol{\tau_{min} \approx 2.5}$ **years**.

After a discussion of the outcomes in relation to the most important irradiation frame conditions foreseen to be applied in the HBS project, it is most rational to assume no substantial and limiting radiation induced material damages during the whole accumulated operation period of a single tantalum target, as tantalum was anyway found out to be a very radiation resistant material. Though unclear at the moment how often, the target anyway has to be replaced frequently due to observance of radiation safety and disposal issues. Additionally, the operation temperature will most probably remain in a moderate frame insufficient to favor the formation of complex and dangerous defect structures, also owing to the clever internal cooling system going to be applied.

To clarify the radiation damage clearly, and to estimate a maximum lifetime of the target, experimental investigations are indispensable. Therefore, tantalum targets

should be irradiated up to different doses (dpa) and subsequently be tested with regard to several macroscopic material properties. Deriving a correlation between the displacement dose supplemented by analyzation of microscopic damage patterns by means of strong microscopic techniques then ultimately allows to predict a maximum lifetime of the target in the applied irradiation conditions. Such tests are challenging with regard to activation of the samples, and remote handling is most probably required. In principle however, the research centre Jülich itself possesses the necessary infrastructure and experimental stations might be built up without big efforts in a compact way.

Surely, the added value of this research thesis predominantly is of use for the HBS project as the simulations have been conducted with specifications prevailing in this one. The meticulous identification of the radiation induced material damage and the qualitative final damage assessment represent a milestone as it has not been considered so detailed before. Furthermore, the outcomes contribute towards a facilitated and uncomplicated licensing process of the project in the future.
The nuclear community benefits of the outcomes as it once more clarifies the importance and need of radiation damage assessments in any facility that has to deal with energetic radiation. It emphasizes the importance of experimental investigations, necessary to fill existing gaps of reference values in the literature. Apart from that, it might give useful hints about the methodology to obtain reliable damage values.

Bibliography

[1] N. P. Cheremisinoff and P. N. Cheremisinoff, Eds., *Handbook of advanced materials testing*, vol. 9, Materials engineering, New York: Dekker, 1995, 1019 pp.

[2] (2020, Aug. 16). "Nmi3–integrated infrastructure initiative for neutron scattering and muon spectroscopy," [Online]. Available: https://nmi3.eu/.

[3] D. L. Chichester, "Production and applications of neutrons using particle accelerators," in *Industrial accelerators and their applications*, Singapore and Hackensack, N.J.: World Scientific Pub. Co, 2012, pp. 243–305.

[4] R. P. Spencer, T. G. Mitchell, and E. King, "Medical applications of neutron activation analysis," *Int. J. Appl. Radiat. Isot.*, vol. 3, pp. 104–112, 1958.

[5] B. Loeper *et al.*, "Neutrons for medicine," *Neutron News*, vol. 21, pp. 16–19, 2010.

[6] F. Fernandez-Alonso and D. Price, Eds., *Neutron scattering, Applications in biology, chemistry, and materials science*, vol. 49, Experimental methods in the physical sciences, Cambridge, MA et al.: Elsevier AP Academic Press, 2017, 753 pp.

[7] P. B. Moore, "Applications of neutron scattering to biology," *Phys. Today*, vol. 38, pp. 62–72, 1985.

[8] J. Walker, "Uses of neutrons in engineering and technology," *Physics in Technology*, vol. 13, pp. 239–248, 1982.

[9] A. Letourneau *et al.*, "Development of compact accelerator neutron source," *EPJ Web Conf.*, vol. 146, 2017.

[10] F. Ott, *Compact neutron sources for neutron scattering.* [Technical Report] Commissariat à l'énergie atomique (CEA) Paris Saclay, 2018.

[11] A. Kowalczyk, "Proton induced spallation reactions in the energy range 0.1 - 10 GeV," Ph.D. dissertation, Jagiellonian University, 2007.

[12] D. Kiselev, "Activation and radiation damage in the environment of hadron accelerators," *CERN Accelerator School: High Power Hadron Machines, CAS 2011 - Proceedings*, 2013.

[13] R. E. Masterson, *Introduction to Nuclear Reactor Physics*, 1st ed., ser. 500 Tips. Milton: CRC Press, 2017, 1108 pp.

[14] J. R. Lamarsh and A. J. Baratta, *Introduction to nuclear engineering*, 3rd ed., ser. Addison-Wesley series in nuclear science and engineering. Upper Saddle River, N.J.: Prentice Hall, 2001, 783 pp.

[15] M. Salvatores and G. Palmiotti, "Radioactive waste partitioning and transmutation within advanced fuel cycles: Achievements and challenges," *Prog. Part. Nucl. Phys.*, vol. 66, pp. 144–166, 2011.

[16] I. S. Anderson *et al.*, "Research opportunities with compact accelerator-driven neutron sources," *Phys. Rep.*, vol. 654, pp. 1–58, 2016.

[17] G. S. Bauer, *Physics and technology of spallation neutron sources*, [Technical Report] Paul Scherrer Institut (PSI) Switzerland Villingen, 1998.

[18] T. Gutberlet *et al.*, "Do neutrons publish? A neutron publication survey, 2005–2015," *Neutron News*, vol. 29, pp. 18–24, 2018.

[19] (2020, July 06). "Union for compact accelerator-driven neutron sources (UCANS)," [Online]. Available: https://www.ucans.org/.

[20] U. Rücker *et al.*, "The Jülich high-brilliance neutron source project," *Eur. Phys. J. Plus*, vol. 131, 2016.

[21] T. Gutberlet *et al.*, "The Jülich high brilliance neutron source project – Improving access to neutrons," *Physica B Condens. Matter*, vol. 570, pp. 345–348, 2019.

[22] T. Cronert *et al.*, "High brilliant thermal and cold moderator for the HBS neutron source project Jülich," *J. Phys. Conf. Ser.*, vol. 746, 2016.

[23] S. Eisenhut *et al.*, "Cryostat for the provision of liquid hydrogen with a variable ortho-para ratio for a low-dimensional cold neutron moderator," *EPJ Web Conf.*, vol. 231, 2020.

[24] H. Zhao *et al.*, Eds., *High-Brilliance Neutron Source Project*, JACoW Publishing, Geneva, Switzerland, presented at the Proceedings of the 14th Int. Conf. on Heavy Ion Accelerator Technology, HIAT2018, Lanzhou, China, 2019.

[25] J. P. Dabruck, *Target Station Optimization for the High-Brilliance Neutron Source HBS, Simulation Studies Based on the Monte Carlo Method*, ser. Springer Theses, Recognizing Outstanding Ph.D. Research. Cham: Springer International Publishing, 2018, 190 pp.

[26] T. Gutberlet and T. Brückel, Eds., *Conceptual design report (CDR)*, [Technical Report] Jülich Centre for Neutron Science (JCNS) Germany Jülich, 2020.

[27] F. Cardarelli, *Materials handbook, A concise desktop reference*, 2nd ed. London: Springer, 2008.

[28] A. San-Martin and F. D. Manchester, "The H-Ta (hydrogen-tantalum) system," *Journal of Phase Equilibria*, vol. 12, pp. 332–343, 1991.

[29] V. T. Astrelin *et al.*, "Blistering of the selected materials irradiated by intense 200 kev proton beam," *J. Nucl. Mater*, vol. 396, pp. 43–48, 2010.

[30] D. Kiselev *et al.*, "Activation of targets and accelerator components at PSI - A comparison of simulation and measurement," *HB 2008 - 42nd ICFA Advanced Beam Dynamics Workshop on High- Intensity, High-Brightness Hadron Beams*, pp. 363–370, 2008.

[31] N. N. Alekseenko, *Radiation damage of nuclear power plant pressure vessel steels*, ser. Russian materials monograph series. La Grange Park, Ill: American Nuclear Society, 1997, vol. 2, 282 pp.

[32] M. S. Wechsler, "Radiation embrittlement in the pressure-vessel steels of nuclear power plants," *JOM*, vol. 41, pp. 7–14, 1989.

[33] J. A. Mascitti and M. Madariaga, "Method for the Calculation of DPA in the Reactor Pressure Vessel of Atucha II," *Science and Technology of Nuclear Installations*, vol. 2011, pp. 1–6, 2011.

[34] S. F. G. Ardekani and K. Hadad, "Monte Carlo evaluation of neutron irradiation damage to the VVER-1000 RPV," *Nuclear Energy and Technology*, vol. 3, pp. 73–80, 2017.

[35] P. Rodriguez, R. Krishnan, and C. V. Sundaram, "Radiation effects in nuclear reactor materials - correlation with structure," *Bull. Mater. Sci.*, vol. 6, pp. 339–367, 1984.

[36] W. Hoffelner, "Irradiation damage in nuclear power plants," in *Handbook of damage mechanics, Nano to macro scale for materials and structures*, ser. Springer reference, G. Z. Voyiadjis, Ed., NY: Springer, 2015, pp. 1427–1461.

[37] J. Fu *et al.*, "Molecular dynamics simulations of high-energy radiation damage in W and W–Re alloys," *J. Nucl. Mater*, vol. 524, pp. 9–20, 2019.

[38] J. Fikar and R. Schäublin, "Molecular dynamics simulation of radiation damage in bcc tungsten," *Nucl. Instrum. Methods Phys. Res., B*, vol. 255, pp. 27–31, 2007.

[39] K. Nordlund *et al.*, "Primary radiation damage: A review of current understanding and models," *J. Nucl. Mater*, vol. 512, pp. 450–479, 2018.

[40] A. Tundwal *et al.*, "Monte Carlo simulation of radiation damage produced in iron and vanadium by primary knock on atom 'PKA'," *Radiat. Eff. Defects Solids*, vol. 171, pp. 658–667, 2016.

[41] H. Ullmaier, *Design properties of tantalum or everything you always wanted to know about tantalum but were afraid to ask*, [Technical Report] European Spallation Source (ESS) Sweden Lund, 2003.

[42] R.E. Stoller, "Primary radiation damage formation," in *Comprehensive Nuclear Materials*, vol. 1, Elsevier, 2012, pp. 293–332.

[43] (2020, Aug. 02). "Radiate collaboration - radiation damage in accelerator target environments," [Online]. Available: https://radiate.fnal.gov/.

[44] J. Linke *et al.*, "Challenges for plasma-facing components in nuclear fusion," *Matter Radiat. at Extremes*, vol. 4, 2019.

[45] J.-A. Wang *et al.*, "Radiation Effects on Spacecraft Structural Materials," 2002.

[46] G. R. Odette and B. D. Wirth, "Radiation Effects in Fission and Fusion Reactors," in *Handbook of Materials Modeling*, S. Yip, Ed., Springer Netherlands, 2005, pp. 999–1037.

[47] H. Ullmaier, "Radiation Damage in Metallic Materials," *MRS Bull.*, vol. 22, pp. 14–21, 1997.

[48] K. E. Holbert, "Radiation Effects and Damage 1. Ionizing Radiations," 2007.

[49] N. V. Mokhov and F. Cerutti, "Beam–Material Interactions," 2016.

[50] M. I. Guseva *et al.*, "Influence of target structure on blister formation by helium and hydrogen ions bombardment," *J. Nucl. Mater*, vol. 76-77, pp. 224–227, 1978.

[51] I. Gavish Segev *et al.*, "Blister formation at subcritical doses in tungsten irradiated by Mev protons," *J. Nucl. Mater*, vol. 496, pp. 77–84, 2017.

[52] P. B. Johnson and D. J. Mazey, "Helium gas bubble lattices in face-centred-cubic metals," *Nature*, vol. 276, pp. 595–596, 1978.

[53] T. Rinckel *et al.*, "Target Performance at the Low Energy Neutron Source," *Phys. Procedia*, vol. 26, pp. 168–177, 2012.

[54] R. Ronningen, "Proc. 46th ICFA Advanced Beam Dynamics Workshop on High-Intensity and High-Brightness Hadron Beams (HB2010)," Morschach, Switzerland, 2010, p.662.

[55] M. Nastasi and J. W. Mayer, *Ion Implantation and Synthesis of Materials*, 1st ed., ser. Springer Series in Materials Science, v.80. Berlin, Heidelberg: Springer-Verlag Berlin Heidelberg, 2006.

[56] B. L. Eyre, "Transmission electron microscope studies of point defect clusters in fcc and bcc metals," *J. Phys. F: Met. Phys.*, vol. 3, pp. 422–470, 1973.

[57] A. Hashimoto *et al.*, "Direct evidence for atomic defects in graphene layers," *Nature*, vol. 430, pp. 870–873, 2004.

[58] M. Ghaly and R. S. Averback, "Effect of viscous flow on ion damage near solid surfaces," *Phys. Rev. Lett.*, vol. 72, pp. 364–367, 1994.

[59] S. Roorda *et al.*, "Structural and electrical defects in amorphous silicon probed by positrons and electrons," *J. Appl. Phys.*, vol. 72, pp. 5145–5152, 1992.

[60] K. Laaziri *et al.*, "High-energy x-ray diffraction study of pure amorphous silicon," *Phys. Rev. B*, vol. 60, pp. 13 520–13 533, 1999.

[61] G. S. Was, *Fundamentals of Radiation Materials Science, Metals and Alloys*, 2nd ed. New York, NY and s.l.: Springer New York, 2017, 1002 pp.

[62] Dornberger, E., "Prediction of OSF Ring Dynamics and Grown-in Voids in Czochralski Silicon Crystals," Ph.D. dissertation, 1997.

[63] G. Gottstein, *Physical Foundations of Materials Science*. Berlin, Heidelberg and s.l.: Springer Berlin Heidelberg, 2004, 502 pp.

[64] T. Troev *et al.*, "Model calculation of positron states in tungsten containing hydrogen and helium," *J. Phys.: Conf. Ser.*, vol. 207, 2010.

[65] D. Kiselev *et al.*, "Radiation damage of components in the environment of high-power proton accelerators," JACoW Publishing, Geneva, Switzerland, presented at the Proceedings of the 21st Int. Conf. on Cyclotrons and their Applications, Cyclotrons2016, Zurich, Switzerland, 2017.

[66] R. W. Cahn and P. Haasen†, Eds., *Physical Metallurgy*, 4th ed., Oxford: North-Holland, 1996.

[67] K. Nordlund *et al.*, *Primary Radiation Damage in Materials. Review of Current Understanding and Proposed New Standard Displacement Damage Model to Incorporate in Cascade Defect Production Efficiency and Mixing Effects*, 2015. [Online]. Available: https://www.oecd-nea.org/science/docs/2015/nsc-doc2015-9.pdf (visited on 08/02/2020).

[68] S. A. Santa and S. Suwoto, "Neutron Radiation Damage Estimation in the Core Structure Base Metal of RSG GAS," *J. Phys.: Conf. Ser.*, vol. 962, 2018.

[69] S. Meigo *et al.*, *Measurement of displacement cross section of proton in energy region between 3 and 30 GeV for high-intensity proton accelerator facility*, J-PARC Center, Japan Atomic Energy Agency (JAEA) Japan/J-PARC Center, High Energy Accelerator Research Organization (KEK), Japan, 2017. [Online]. Available: https://j-parc.jp/researcher/Hadron/en/pac_1707/pdf/P67_2017-12.pdf (visited on 05/13/2020).

[70] D.-Y. Lin, H. Song, and X. Hui, "Molecular dynamics simulation of threshold displacement energy and primary damage state in Niobium," 2017.

[71] H. Schroeder and B. Stritzker, "Resistivity annealing of gold after 150 kev proton irradiation at 0.3 k," *Radiat. Eff. Defects Solids*, vol. 33, pp. 125–126, 1977.

[72] T. D. Swinburne, P.-W. Ma, and S. L. Dudarev, "Low temperature diffusivity of self-interstitial defects in tungsten," *New J. Phys.*, vol. 19, 2017.

[73] M. Biget *et al.*, "On the spontaneous recombination volume of Frenkel defects in irradiated b.c.c. metals," *Solid State Commun.*, vol. 16, pp. 949–952, 1975.

[74] W. Schilling and K. Sonnenberg, "Recovery of irradiated and quenched metals," *J. Phys. F: Met. Phys.*, vol. 3, pp. 322–350, 1973.

[75] M. T. Robinson and I. M. Torrens, "Computer simulation of atomic-displacement cascades in solids in the binary-collision approximation," *Phys. Rev. B*, vol. 9, pp. 5008–5024, 1974.

[76] K. Nakashima, R. E. Stoller, and H. Xu, "Recombination radius of a Frenkel pair and capture radius of a self-interstitial atom by vacancy clusters in bcc Fe," *J. Phys. Condens. Matter*, vol. 27, 2015.

[77] B. Beeler *et al.*, "Effect of strain and temperature on the threshold displacement energy in body-centered cubic iron," *J. Nucl. Mater*, vol. 474, pp. 113–119, 2016.

[78] J. C. Meyer *et al.*, "Accurate measurement of electron beam induced displacement cross sections for single-layer graphene," *Phys. Rev. Lett.*, vol. 108, 2012.

[79] T. Susi *et al.*, "Isotope analysis in the transmission electron microscope," *Nat. Commun.*, vol. 7, 2016.

[80] A. Karim *et al.*, "Electron radiation damage in H.C.P. metals – I. The determination of the threshold displacement energy in Zn, Cd, Mg and Ti," *Acta Metall.*, vol. 26, pp. 975–981, 1978.

[81] M. Robinson, N. A. Marks, and G. R. Lumpkin, "Sensitivity of the threshold displacement energy to temperature and time," *Phys. Rev. B*, vol. 86, 2012.

[82] K. Nordlund, J. Wallenius, and L. Malerba, "Molecular dynamics simulations of threshold displacement energies in Fe," *Nucl. Instrum. Methods Phys. Res., B*, vol. 246, pp. 322–332, 2006.

[83] S. Chen and D. Bernard, "On the calculation of atomic displacements using damage energy," *Results Phys*, vol. 16, 2020.

[84] D. R. Olander, *Fundamental aspects of nuclear reactor fuel elements*, [Technical Report] California University USA Berkeley, 1976.

[85] K. Urban and N. Yoshida, "The threshold energy for atom displacement in irradiated copper studied by high-voltage electron microscopy," *Philos. Mag. A*, vol. 44, pp. 1193–1212, 1981.

[86] E. A. Kenik and T. E. Mitchell, "Orientation dependence of the threshold displacement energy in copper and vanadium," *Philos. Mag.*, vol. 32, pp. 815–831, 1975.

[87] A. J. McKenna *et al.*, "Threshold displacement energy and damage function in graphite from molecular dynamics," *Carbon*, vol. 99, pp. 71–78, 2016.

[88] J. Bourgoin and M. Lannoo, *Point Defects in Semiconductors II, Experimental Aspects*, ser. Springer Series in Solid-State Sciences. Berlin and Heidelberg: Springer, 1983, vol. 35, 295 pp.

[89] M. Griffiths, "Displacement energies for Zr measured in a HVEM," *J. Nucl. Mater*, vol. 165, pp. 315–317, 1989.

[90] K. Nordlund *et al.*, "Improving atomic displacement and replacement calculations with physically realistic damage models," *Nat. Commun.*, vol. 9, 2018.

[91] D. A. Thompson, "High density cascade effects," *Radiat. Eff. Defects Solids*, vol. 56, pp. 105–150, 1981.

[92] K. Nordlund *et al.*, "Heat spike effects on ion beam mixing," *Nucl. Instrum. Methods Phys. Res., B*, vol. 164-165, pp. 441–452, 2000.

[93] J. A. Brinkman, "On the Nature of Radiation Damage in Metals," *J. Appl. Phys.*, vol. 25, pp. 961–970, 1954.

[94] J. A. Brinkman, "Production of Atomic Displacements by High-Energy Particles," *Am. J. Phys.*, vol. 24, pp. 246–267, 1956.

[95] A. Seeger, Ed., *On the theory of radiation damage and radiation hardening*, presented at the Proceedings of the Second United Nations international conference on the peaceful uses of atomic energy, vol. 6, Geneva, 1958.

[96] T. D. de la Rubia *et al.*, "Role of thermal spikes in energetic displacement cascades," *Phys. Rev. Lett.*, vol. 59, pp. 1930–1933, 1987.

[97] D. C. Agarwal *et al.*, "Phase transformation of ZnMoO 4 by localized thermal spike," *J. Appl. Phys.*, vol. 115, 2014.

[98] K. Nordlund and R. S. Averback, "Point defect movement and annealing in collision cascades," *Phys. Rev. B*, vol. 56, pp. 2421–2431, 1997.

[99] E. B. Podgorsak, *Radiation Physics for Medical Physicists*, 3rd ed., ser. Graduate Texts in Physics. Cham: Springer, 2016, 906 pp.

[100] C. Consolandi, "Displacement damage induced by cosmic rays in silicon devices using Geant4 toolkit for space applications," Doctoral thesis, University Milano Bicocca, Italy, 2009.

[101] C. Leroy and P.-G. Rancoita, *Principles of radiation interaction in matter and detection*, 4th ed. New Jersey et al.: World Scientific, 2016, 1345 pp.

[102] S. Messenger *et al.*, "Nonionizing Energy Loss (NIEL) for heavy ions," *IEEE Trans. Nucl. Sci.*, vol. 46, 2004.

[103] A. Fasso *et al.*, "FLUKA Realistic Modeling of Radiation Induced Damage," *J. Nucl. Sci. Technol.*, vol. 2, pp. 769–775, 2011.

[104] G. H. Kinchin and R. S. Pease, "The Displacement of Atoms in Solids by Radiation," *Rep, Prog. Phys.*, vol. 18, pp. 1–51, 1955.

[105] K. R. Whittle, *Nuclear materials science*, ser. IOP expanding physics. Bristol: IOP Publishing, 2016.

[106] M. I. Bratchenko *et al.*, "Comments on DPA calculation methods for ion beam driven simulation irradiations," *Probl. Atom. Sci. Tech.*, pp. 11–16, 2013.

[107] ASTM International, *ASTM E693-94, Standard Practice for Characterizing Neutron Exposures in Iron and Low Alloy Steels in Terms of Displacements Per Atom (DPA), E706(ID), ASTM International*, ASTM International West Conshohocken. [Online]. Available: www.astm.org.

[108] M. J. Norgett, M. T. Robinson, and I. M. Torrens, "A proposed method of calculating displacement dose rates," *Nucl. Eng. Des*, vol. 33, pp. 50–54, 1975.

[109] J. Lindhard, M. Scharff, H. E. Schiøt, "Range concepts and heavy ion ranges (notes on atomic collisions, II)," *Mat.-fys. Medd.r-Kong. Danske Vid. Selsk*, vol. 33, pp. 1–42, 1963.

[110] S. Chen *et al.*, "Calculation and verification of neutron irradiation damage with differential cross sections," *Nucl. Instrum. Methods Phys. Res., B*, vol. 456, pp. 120–132, 2019.

[111] J. Lindhard *et al.*, "Integral equations governing radiation effects (Notes on atomic collisions, III)," *Mat. Fys. Medd. Dan. Vid. Selsk.*, vol. 33, pp. 1–42, 1963.

[112] L. Malerba, "Molecular dynamics simulation of displacement cascades in α-Fe: A critical review," *J. Nucl. Mater*, vol. 351, pp. 28–38, 2006.

[113] R. S. Averback and K. L. Merkle, "Radiation-annealing effects in energetic displacement cascades," *Phys. Rev. B*, vol. 16, pp. 3860–3869, 1977.

[114] D. Reiter, "The Monte Carlo Method, an Introduction," *Lect. Notes Phys.*, vol. 739, pp. 63–78, 2007.

[115] J. M. Hammersley and D. C. Handscomb, *Monte Carlo Methods*, ser. Monographs on Applied Probability and Statistics. Dordrecht: Springer, 1964, 188 pp.

[116] M. Yano *et al.*, *Math, Numerics and Programming: For Mechanical Engineers*. 2013.

[117] I. H. Hutchinson, *A student's guide to numerical methods*. Cambridge: Cambridge University Press, 2015, 207 pp.

[118] J. F. Ziegler. (2020, Aug. 14). "James Ziegler - SRIM & TRIM," [Online]. Available: http://www.srim.org/.

[119] J. F. Ziegler, M. D. Ziegler, and J. P. Biersack, "SRIM – The stopping and range of ions in matter," *Nucl. Instrum. Methods Phys. Res., B*, vol. 268, pp. 1818–1823, 2010.

[120] J. Cang *et al.*, "A simple method to calculate the displacement damage cross section of silicon carbide," *Nucl. Eng. Technol.*, vol. 46, pp. 475–480, 2014.

[121] J.-P. Crocombette and C. van Wambeke, "Quick calculation of damage for ion irradiation: implementation in Iradina and comparisons to SRIM," *EPJ Nuclear Sci. Technol.*, vol. 5, 2019.

[122] R. E. Stoller *et al.*, "On the use of SRIM for computing radiation damage exposure," *Nucl. Instrum. Methods Phys. Res., B*, vol. 310, pp. 75–80, 2013.

[123] A. Mohammadi, S. Hamidi, and M. A. Asadabad, "The use of the SRIM code for calculation of radiation damage induced by neutrons," *Nucl. Instrum. Methods Phys. Res., B*, vol. 412, pp. 19–27, 2017.

[124] J. P. Biersack and L. G. Haggmark, "A Monte Carlo computer program for the transport of energetic ions in amorphous targets," *Nucl. Instrum. Meth.*, vol. 174, pp. 257–269, 1980.

[125] J. F. Ziegler, J. P. Biersack, and M. D. Ziegler, *SRIM, The Stopping and Range of Ions in Matter*. Chester, Md.: SRIM Company, 2008, 683 pp.

[126] G. Youngblood, S. Myhra, and J. W. DeFord, "Measurements of the Threshold Displacement Energy in Ta and Nb," *Phys. Rev.*, vol. 188, pp. 1101–1107, 1969.

[127] M. Biget *et al.*, "Near-threshold displacements in tantalum single crystals," *Phys. Rev. B*, vol. 19, pp. 820–830, 1979.

[128] P. Jung and W. Schilling, "Anisotropy of the Threshold Energy for the Production of Frenkel Pairs in Tantalum," *Phys. Rev. B*, vol. 5, pp. 2046–2056, 1972.

[129] C. Broeders and A. Konobeyev, "Defect production efficiency in metals under neutron irradiation," *J. Nucl. Mater*, vol. 328, pp. 197–214, 2004.

[130] A. Djaafri *et al.*, "Study of Point Defect Distributions in Tantalum," *Acta Phys. Pol. A*, vol. 133, pp. 39–44, 2018.

[131] A. Konobeyev *et al.*, "Evaluation of effective threshold displacement energies and other data required for the calculation of advanced atomic displacement cross-sections," *Nuclear Energy and Technology*, vol. 3, pp. 169–175, 2017.

[132] T. T. Böhlen *et al.*, "The FLUKA Code: Developments and Challenges for High Energy and Medical Applications," *Nucl. Data Sheets*, vol. 120, pp. 211–214, 2014.

[133] A. Ferrari *et al.*, *FLUKA: A Multi-Particle Transport Code*, 2005.

[134] A. Ferrari *et al.* (2020, Aug. 16). "The official FLUKA site: FLUKA home," [Online]. Available: http://www.fluka.org/fluka.php.

[135] G. Battistoni *et al.*, "FLUKA Capabilities and CERN Applications for the Study of Radiation Damage to Electronics at High-Energy Hadron Accelerators," *Prog. Nucl. Sci. Technol.*, vol. 2, pp. 948–954, 2011.

[136] G. Battistoni *et al.*, "The Application of the Monte Carlo Code FLUKA in Radiation Protection Studies for the Large Hadron Collider," *Prog. Nucl. Sci. and Technol.*, vol. 2, pp. 358–364, 2011.

[137] G. Battistoni *et al.*, "A neutrino-nucleon interaction generator for the FLUKA Monte Carlo code," *CERN-Proceedings*, vol. 2, 2009.

[138] F. Ballarini *et al.*, "The physics of the FLUKA code: Recent developments," *Advances in Space Research*, vol. 40, pp. 1339–1349, 2007.

[139] A. Fasso *et al.*, "The physics models of FLUKA: status and recent development," 2003.

[140] M. B. Emmett, *Morse Monte Carlo Radiation Transport Code System*, 1975.

[141] A. Davis *et al.*, "FluDAG: A CAD based tool for high energy physics," *Nucl. Instrum. Methods Phys. Res. A*, vol. 915, pp. 65–74, 2019.

[142] V. Vlachoudis, *Flair for fluka*, 2008. [Online]. Available: http://www.fluka.org/web_archive/earchive/new-fluka-discuss/att-8425/flair.pdf (visited on 09/08/2020).

[143] V. Vlachoudis, "FLAIR: A Powerful but User Friendly Graphical Interface for FLUKA," 2009.

[144] OCW Massachusets Institute of Technology, *Lecture 2 macroscopic interactions 22.106 neutron interactions and applications spring 2010*, 2010. [Online]. Available: https://ocw.mit.edu/courses/nuclear-engineering/22-106-neutron-interactions-and-applications-spring-2010/lecture-notes/MIT22_106S10_lec02.pdf (visited on 09/08/2020).

[145] M. Yehya *et al.*, "Neutron imaging of hydraulic flow within structural concrete," 2017.

[146] B. J. Marsden, "Nuclear graphite for high temperature reactors," 2001. [Online]. Available: https://www.osti.gov/etdeweb/servlets/purl/20198178 (visited on 09/08/2020).

[147] (2020, Aug. 13). "Home | the official cern fluka website," [Online]. Available: https://fluka.cern/.

[148] K. Nordlund, "Molecular dynamics simulations of atomic collisions for ion irradiation experiments," Ph.D. dissertation, 1995.

[149] J.-P. Shen *et al.*, "Proton-implanted waveguides in neodymium-doped calcium lithium niobium gallium garnet crystals," *Results Phys.*, vol. 15, 2019.

[150] C. Broeders and A. Konobeyev, "Displacement cross-sections for tantalum and tungsten irradiated with protons at energies up to 1 GeV," *J. Nucl. Mater*, vol. 336, pp. 201–209, 2005.

[151] W. J. Weber and Y. Zhang, "Predicting damage production in monoatomic and multi-elemental targets using stopping and range of ions in matter code: Challenges and recommendations," *Curr. Opin. Solid State Mater. Sci.*, vol. 23, 2019.

[152] Y. Dai and G. Bauer, "Status of the first SINQ irradiation experiment, STIP-I," *J. Nucl. Mater*, vol. 296, pp. 43–53, 2001.

[153] C. Rubbia *et al.*, "The TRADE Experiment: Status of the Project and Physics of the Spallation Target," 2004.

[154] N. H. Tiep *et al.*, "Investigation of the VVER-1000 reactor pressure vessel neutron fluence and displacement per atom using MCNP6," *Radiat. Phys. Chem.*, vol. 177, 2020.

[155] J. Brooks *et al.*, "Plasma-facing material alternatives to tungsten," *Nucl. Fusion*, vol. 55, 2015.

[156] G. Skoro *et al.*, "Solid Target for a Neutrino Factory," *European Strategy for Future Neutrino Physics 2009, Proceedings*, 2008.

[157] E. Lopez Sola *et al.*, "Design of a high power production target for the beam dump facility at CERN," *Phys. Rev. Accel. Beams*, vol. 22, 2019.

[158] Q. Yu, T. Liang, and W. Yin, "Activity and radiation protection studies for the W-Ta target of CSNS," *Radiat. Prot. Dosim.*, vol. 136, pp. 216–221, 2009.

[159] A. T. Nelson *et al.*, "Fabrication of a tantalum-clad tungsten target for LANSCE," *J. Nucl. Mater*, vol. 431, pp. 172–184, 2012.

[160] P. Hosemann *et al.*, "Oxygen effects on irradiated tantalum alloys," *J. Nucl. Mater*, vol. 384, pp. 25–29, 2009.

[161] A. Dey and L. Jones, "Strategies to improve ISIS TS2 target life," *J. Nucl. Mater*, vol. 506, pp. 63–70, 2018.

[162] G. S. Bauer, "Overview on spallation target design concepts and related materials issues," *J. Nucl. Mater*, vol. 398, pp. 19–27, 2010.

[163] K.T McDonald, *High-Power Targets for Neutrino and Muon Colliders*, Princeton University, 2009. [Online]. Available: https://www.cap.bnl.gov/mumu/conf/MC-090125/talks/KMcDonald1-090125.pdf (visited on 09/15/2020).

[164] J. Chen *et al.*, "Mechanical properties of pure tantalum after 800 MeV proton irradiation," *J. Nucl. Mater*, vol. 298, pp. 248–254, 2001.

[165] J. Chen *et al.*, "Summary of the results from post-irradiation examination of spent targets at the FZ-Juelich," *J. Nucl. Mater*, vol. 318, pp. 56–69, 2003.

[166] T. S. Byun and S. A. Maloy, "Dose dependence of mechanical properties in tantalum and tantalum alloys after low temperature irradiation," *J. Nucl. Mater*, vol. 377, pp. 72–79, 2008.

[167] D. Wilcox, *Simulating Performance of Tantalum-Clad Tungsten Targets*, High Power Targets Group, Rutherford Appleton Laboratory, 2016. [Online]. Available: https://conference.sns.gov/event/20/images/2907-Simulating_Performance_of_Tantalum_Clad_Tungsten_Targets_-_Dan_Wilcox.pdf (visited on 09/15/2020).

[168] J. Thomason, "The ISIS Spallation Neutron and Muon Source–The first thirty-three years," *Nucl. Instrum. Methods. Phys. Res. B*, vol. 917, pp. 61–67, 2019.

[169] D. Wilcox *et al.*, "Stress levels and failure modes of tantalum-clad tungsten targets at ISIS," *J. Nucl. Mater*, vol. 506, pp. 76–82, 2018.

[170] I. Ipatova *et al.*, "Radiation-induced void formation and ordering in Ta-W alloys," *J. Nucl. Mater*, vol. 495, pp. 343–350, 2017.

[171] K. Yasunaga *et al.*, "Microstructure of tantalum irradiated with heavy ions," *J. Nucl. Mater*, vol. 258-263, pp. 879–882, 1998.

[172] F. W. Wiffen, "The microstructure and swelling of neutron irradiated tantalum," *Journal of Nuclear Materials*, vol. 67, pp. 119–130, 1977.

[173] I. Ipatova and E. Jimenez-Melero, "Effect of Alloying Content on the Defect Structure Formation and Evolution in the Ta-W system," in *European Microscopy Congress 2016: Proceedings*, Weinheim, Germany: Wiley-VCH Verlag GmbH & Co. KGaA, 2016, pp. 353–355.

[174] C. Villagrasa-Roussel, C. Broeders, and A. Konobeyev, "Irradiation Damages in Tantalum Spallation Target," *Kerntechnik*, vol. 71, pp. 113–123, 2006.

[175] D. J. S. Findlay *et al.*, "Experimental verification of spallation inventory calculations," *Appl. Radiat. Isot. : including data, instrumentation and methods for use in agriculture, industry and medicine*, vol. 125, pp. 1–3, 2017.

[176] S. J. Zinkle and F. W. Wiffen, "Radiation Effects in Refractory Alloys," *AIP Conference Proceedings*, vol. 699, 2004.

[177] Y. Smirnov and V. Finkel, "Crystal Structure of Tantalum, Niobium, and Vanadium at 110-400°K," *J. Exp. Theor.*, vol. 22, p. 750, 1966.

[178] I. Ipatova *et al.*, "Void evolution in tungsten and tungsten-5wt.% tantalum under in-situ proton irradiation at 800 and 1000 °C," *J. Nucl. Mater*, vol. 526, 2019.

[179] I. Ipatova *et al.*, "Characterisation of lattice damage formation in tantalum irradiated at variable temperatures," *J. Microsc.*, vol. 270, pp. 110–117, 2018.

[180] S. Das, "Recent advances in characterising irradiation damage in tungsten for fusion power," *SN Applied Sciences*, vol. 1, 2019.

[181] R. C. Birtcher *et al.*, "In situ Transmission Electron Microscopy Investigation of Radiation Effects," *J. Mater. Res.*, vol. 20, pp. 1654–1683, 2005.

[182] P. T. Wady *et al.*, "Accelerated radiation damage test facility using a 5 MV tandem ion accelerator," *Nucl. Instrum. Meth. A*, vol. 806, pp. 109–116, 2016.

Appendices

A. HBS related specifications

A.1 : Accelerator related parameters. Taken and adjusted from [26].

Parameter	Specifications	Unit
Accelerator type	RF Linac	N/A
Particle type	Protons	N/A
Final energy	70	MeV
Average target power	100	kW
Beam duty cycle	2	%
Pulse length	52/208/833	μs
Repetition rate	384/96/24	Hz
Peak beam current	71	mA
Average beam current	1.43	mA
	8.92606E+15	protons/s
	8.92606E+13	protons/cm^2/s

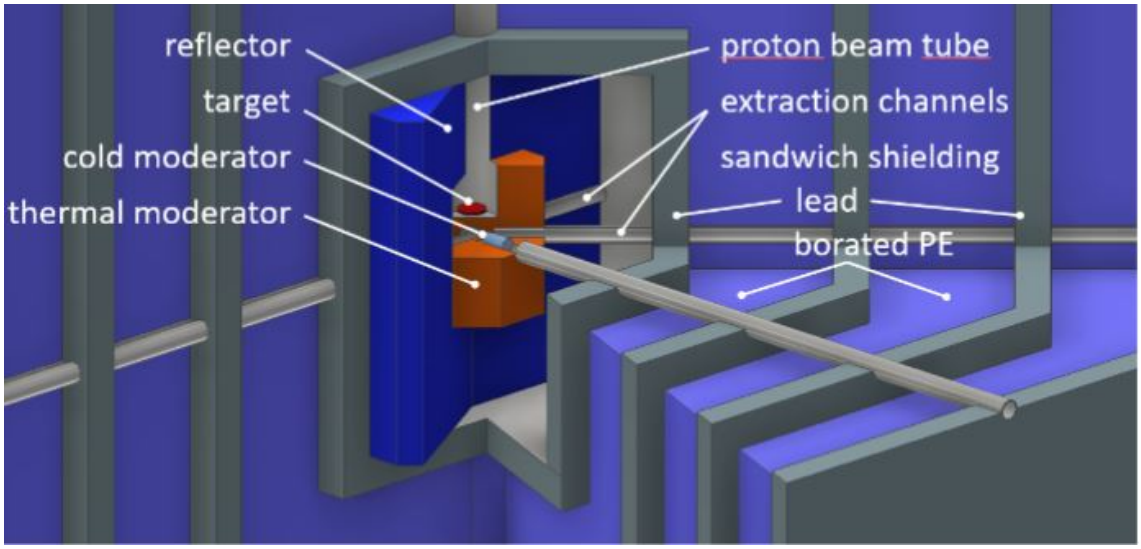

A.2 : Target-Moderator-Reflector (TMR) unit. [26]

A.3 : Activity of main radionuclides produced in the tantalum target during operation. [26]

Proton induced					
Isotope	**$T_{1/2}$**	**Activity after irradiation time [Bq]**			
		30 d	90 d	180 d	360 d
^{179}W	37.05	3.42E+15	3.42E+15	3.42E+15	3.42E+15
^{177}W	135 m	3.05E+15	3.17E+15	3.17E+15	3.17E+15
^{176}W	2.5 h	2.44E+15	2.60E+15	2.60E+15	2.60E+15
^{175}W	35.2 m	1.88E+15	1.88E+15	1.88E+15	1.88E+15
^{178}Ta	9.31 m	1.75E+15	1.75E+15	1.75E+15	1.75E+15
^{174}W	31 m	1.05E+15	1.05E+15	1.05E+15	1.05E+15
^{180}Ta	8.15 h	7.60E+14	1.22E+15	130E+15	131E+15
^{176}Ta	8.09 h	3.42E+14	5.43E+14	5.81E+14	5.84E+14
^{174}Ta	1.05 h	1.77E+14	1.77E+15	1.77E+15	1.77E+15
^{175}Ta	10.5 h	1.56E+14	2.75E+14	3.11E+14	3.17E+14
^{177}Ta	56.56 h	1.30E+14	3.44E+14	5.09E+14	8.54E+14
^{173}W	7.6 m	7.76E+14	7.76E+14	7.76E+14	7.76E+14
^{178}W	21.6 d	4.89E+13	1.45E+14	2.85E+14	5.84E+14
^{173}Ta	3.14 h	4.82E+13	4.82E+13	4.82E+13	4.82E+13
^{180m}Hf	5.5 h	2.16E+13	2.16E+13	2.16E+13	2.16E+13
^{173}Hf	23.6 h	8.84E+12	2.03E+13	2.85E+13	3.31E+13
^{171}Hf	12.1 h	6.22E+12	1.16E+13	1.36E+13	1.40E+13
^{169}Hf	3.24 m	3.46E+12	3.46E+12	3.46E+12	3.46E+13
^{170}Hf	16.1 h	2.89E+12	5.94E+12	7.50E+12	8.02E+12
^{172}Ta	36.8 m	2.63E+12	2.63E+12	2.63E+12	2.63E+12
^{181}W	121.2 d	1.11E+12	3.31E+12	6.59E+12	1.31E+13
^{179}Ta	1.82 y	1.04E+12	3.14E+12	6.27E+12	1.25E+13
^{175}Hf	70 d	2.76E+11	8.27E+11	1.66E+12	3.25E+12
^{179}Lu	4.59 h	2.17E+11	2.73E+11	2.76E+11	2.76E+11
^{178}Lu	28.4 m	1.96E+11	1.96E+11	1.96E+11	1.96E+11
^{178m}Lu	23.1 m	1.15E+11	1.15E+11	1.15E+11	1.15E+11
^{172}Hf	1.87 y	1.63E+10	3.52E+10	7.03E+10	1.40E+11
^{3}H	12.33 y	1.54E+10	4.61E+10	9.16E+10	1.80 E+11
Neutron induced					
^{182}Ta	114.43 d	8.62E+15	21.8E+15	34.5E+15	46.0E+15
^{182m}Ta	15.84 m	2.20E+13	2.20E+13	2.20E+13	2.20E+13
^{180}Ta	8.15 h	1.31E+12	1.31E+12	1.31E+12	1.31E+12
^{181}Hf	42.39 d	2.28E+08	4.53E+08	5.57E+08	5.87E+08
^{179}Ta	1.82 y	6.56E+07	1.90E+08	3.64E+08	6.67E+08

A.4 : Target activity data. Dose rates were calculated with the SISy software (v. 2.5.2) and correspond to a distance of 1 m from the unshielded target. [26]

Parameter	Irradiation parameters			
	30 d	**90 d**	**180 d**	**360 d**
	1.03 Ah	**3.09 Ah**	**6.18 Ah**	**12.36 Ah**
Activity [PBq]	24.0	38.6	51.9	64.0
Proton induced	15.4	16.8	17.4	18.0
Neutron induced	8.6	21.8	34.5	46.0
Decay heat [kW]	6.6	10.8	14.7	18.1
Proton induced	4.1	4.5	4.7	4.7
Neutron induced	2.5	6.3	10.0	13.4
Heat deposition [kW]	0.99	1.57	2.00	2.39
Proton induced	0.70	0.84	0.84	0.85
Neutron induced	0.29	0.73	1.16	1.54
Dose rate [Sv/h]	2422	5116	7626	9917
Proton induced	752	889	936	997
Neutron induced	1670	4227	6690	8920

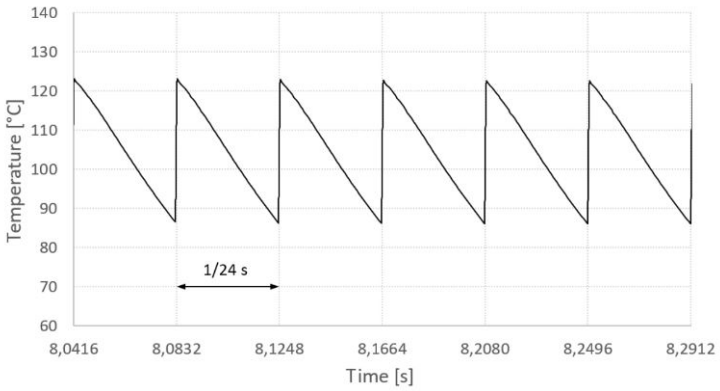

A.5 : Time dependent temperature maximum inside the internally cooled target caused by a 100 mA pulsed proton beam at 24 Hz. [26]

A.6 : Scheme of the internally cooled target. The water enters the target by a feed water line through a flow laminator. It will then flow through fish-bone like microchannels to carry away the released heat. [26]

B. Supplementary simulation data

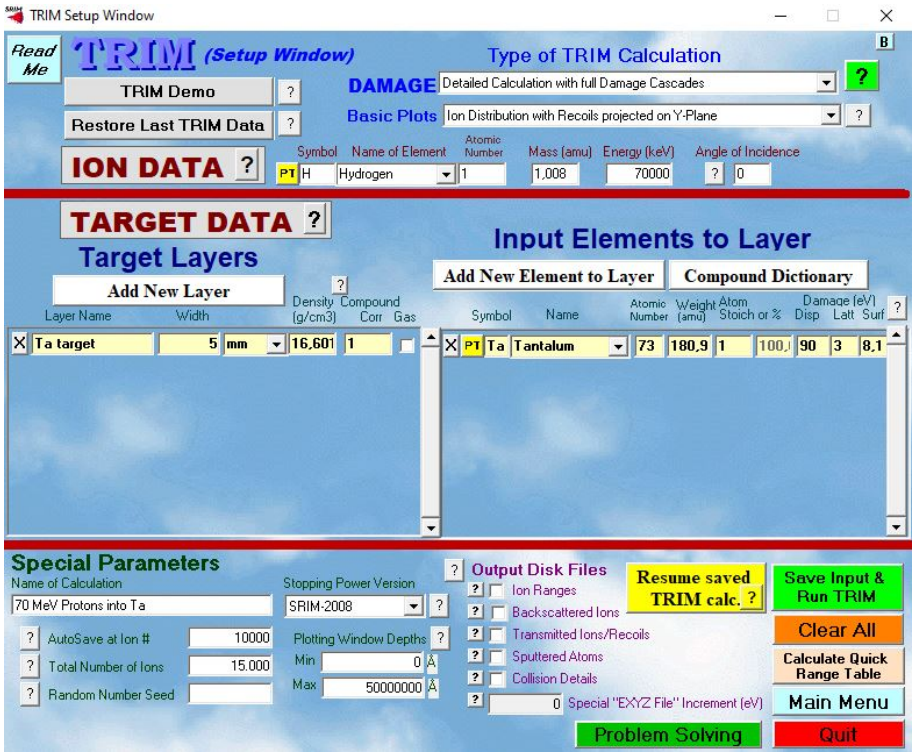

B.1 : User interface of SRIM. Except for the ion type, the ion energy, the layer (material and thickness) and the number of primary particles default values have been kept.

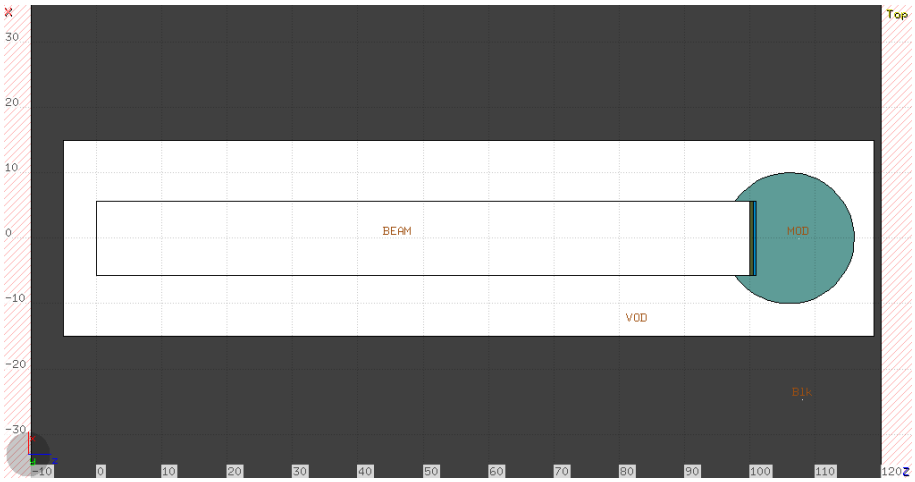

B.2 : Full FLUKA geometry. The picture is taken from the flair geometry editor.

B.3 : Average number of atomic displacements for varying proton energies and different particles of the hadronic collision cascade. The data was obtained with the FLUKA internal *DPA-SCO* scoring method.

Particle	**Average dpa/primary for different energies [MeV]**				
	10	**30**	**50**	**70**	**90**
All	3.34E-24	7.43E-24	1.21E-23	1.57E-23	1.36E-23
All charged	3.34E-24	7.37E-24	1.19E-23	1.15E-23	1.28E-23
Protons	3.34E-24	7.35E-24	1.18E-23	1.49E-23	1.25E-23
Primaries	3.34E-24	7.34E-24	1.18E-23	1.49E-23	1.23E-23
Electrons	6.57E-34	1.52E-30	5.21E-30	1.07E-29	1.25E-29
Heavy ions (Z>2)	0.00E+00	2.48E-26	8.13E-26	1.86E-25	2.68E-25
Helium-4	0.00E+00	1.17E-28	1.51E-27	6.40E-27	1.50E-26
Helium-3	0.00E+00	0.00E+00	0.00E+00	0.00E+00	0.00E+00
Deuteron	0.00E+00	2.25E-31	5.14E-30	4.30E-29	1.48E-28
Triton	0.00E+00	0.00E+00	6.51E-30	4.44E-29	1.31E-28
All neutral	8.22E-29	2.10E-25	8.87E-25	2.19E-24	3.09E-24
Neutrons	5.72E-29	5.80E-26	2.53E-25	6.03E-25	8.46E-25
Photons	1.38E-34	2.22E-31	7.29E-31	1.48E-30	1.65E-30

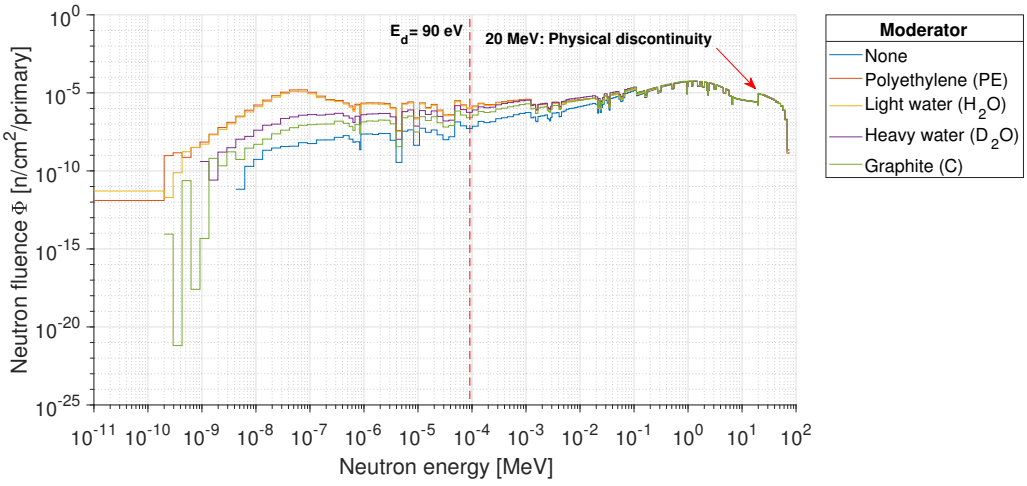

B.4 : Non-differential neutron energy spectra. Due to unequal bin widths below and above 20 MeV, a physical discontinuity appears at 20 MeV. The case without moderator included the beamstop, hence thermal neutrons are visible.

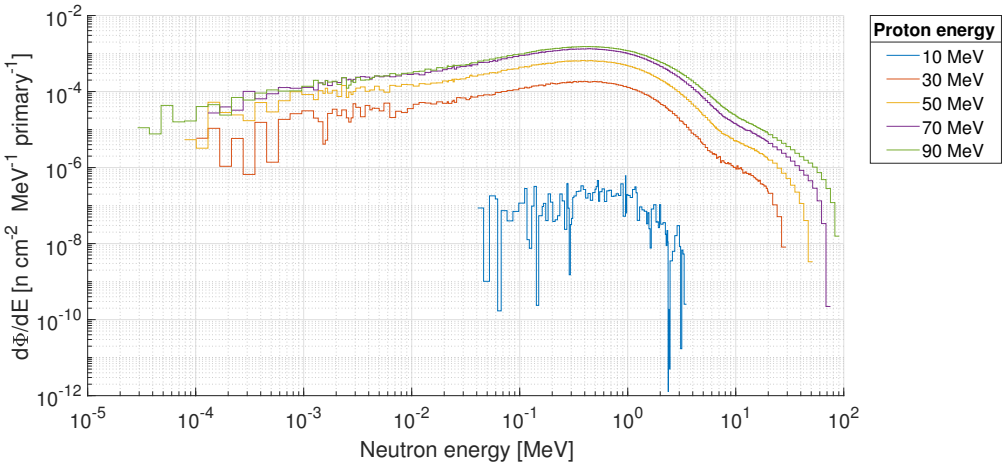

B.5 : Differential neutron energy spectra of the simple geometry and varying proton energies.

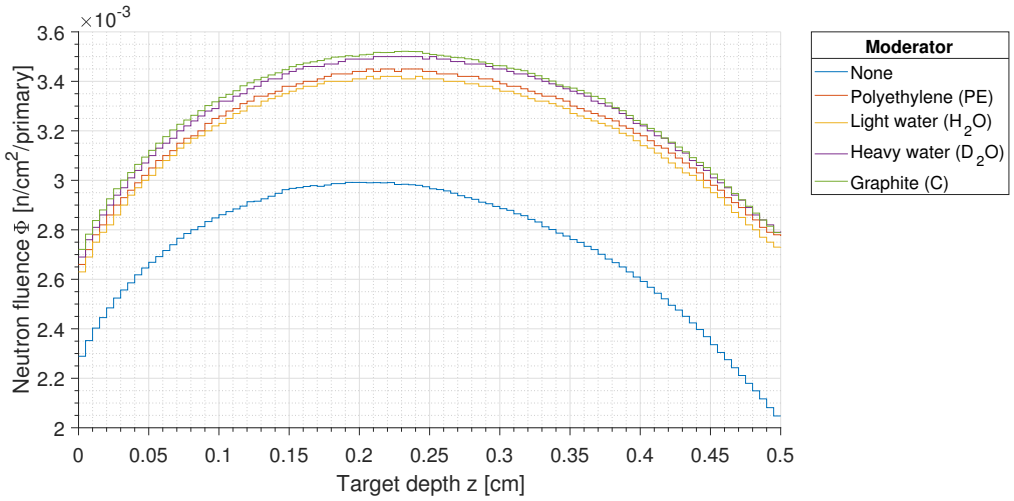

B.6 : Total neutron fluence as a function of the target depth with and without beamstop and moderators.

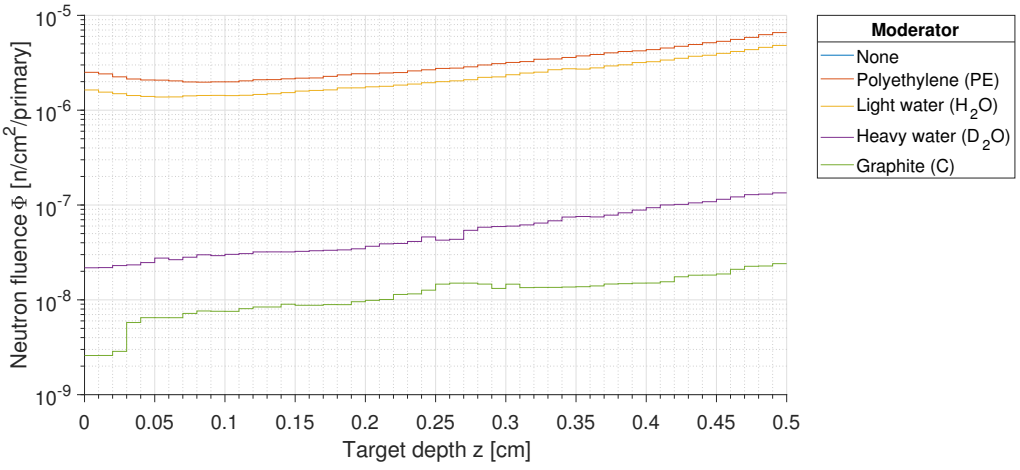

B.7 : Cold neutron spectra for all moderators and without.

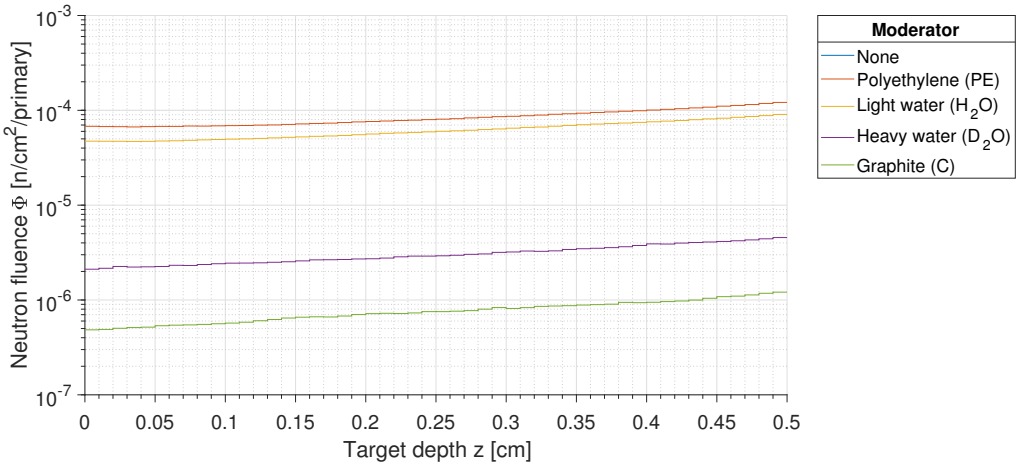

B.8 : Thermal neutron spectra for all moderators and without.

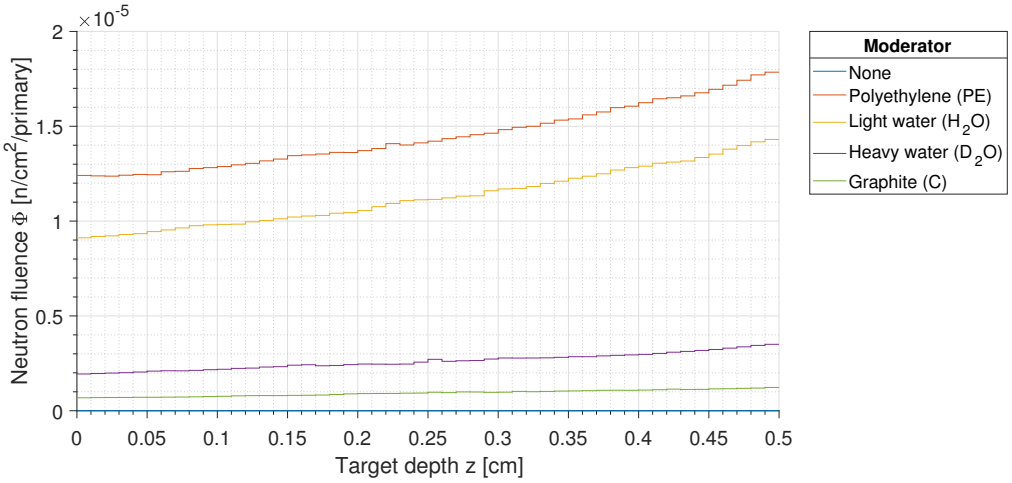

B.9 : Epithermal neutron spectra for all moderators and without.

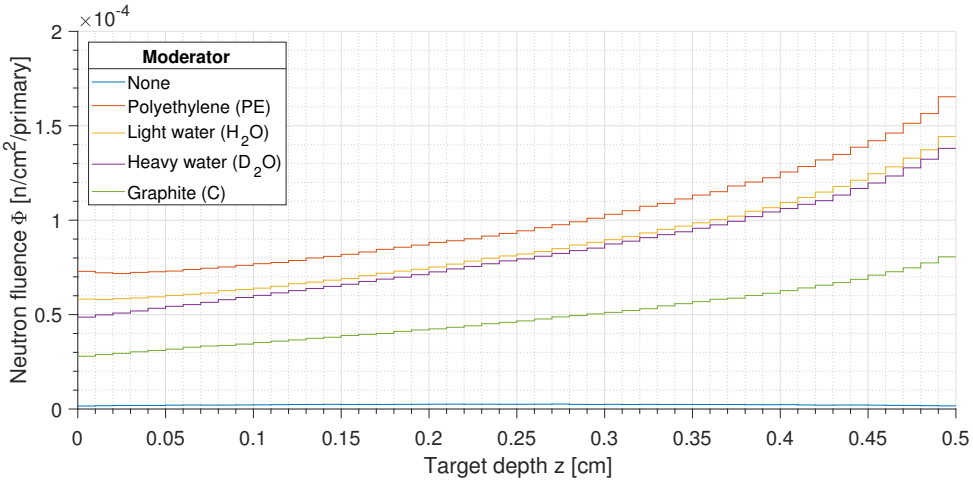

B.10 : Resonance neutron spectra for all moderators and without.

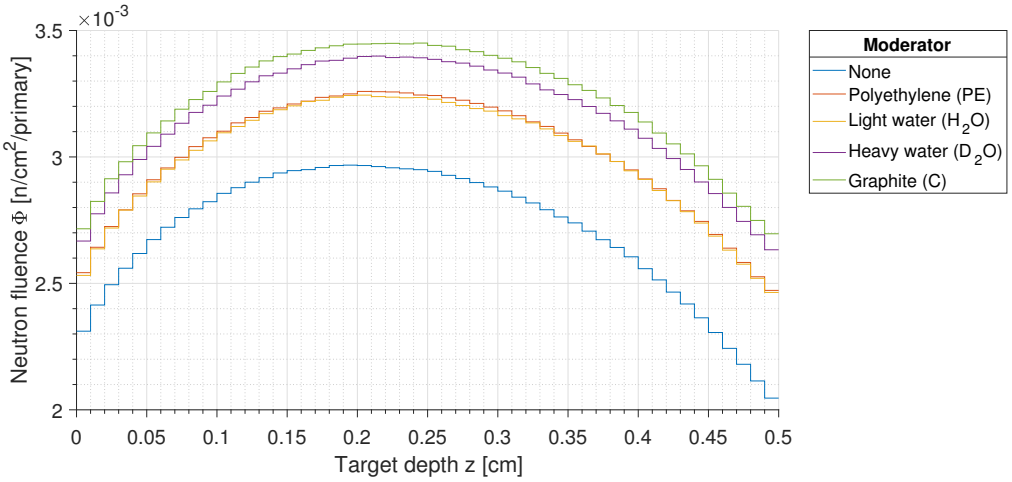

B.11 : Fast neutron spectra for all moderators and without.

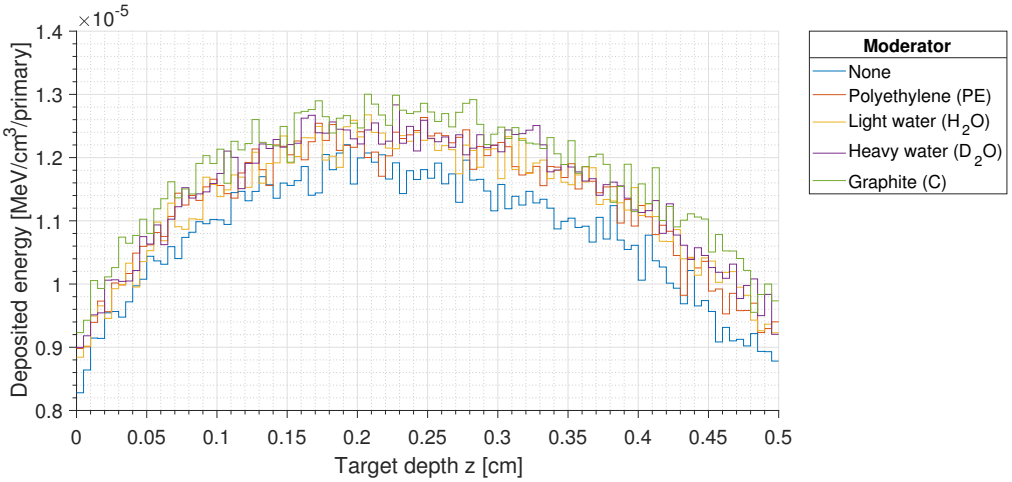

B.12 : Energy deposition of neutrons with various moderators along the target depth.

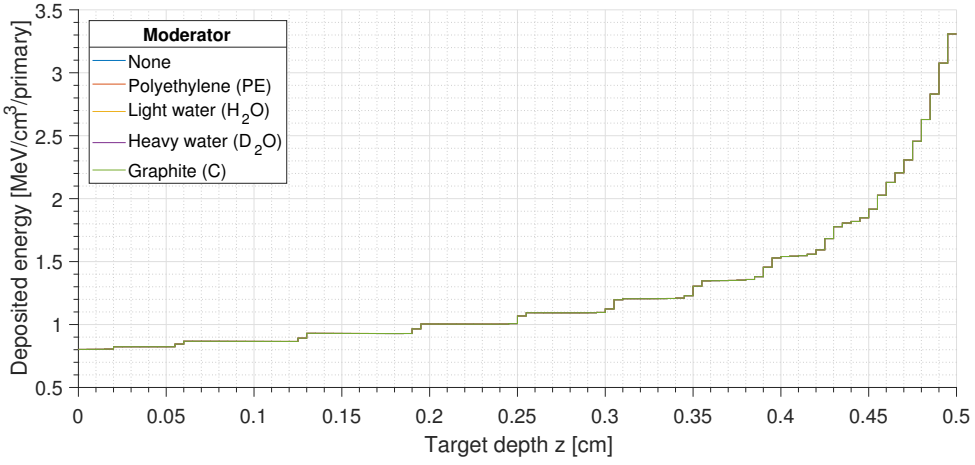

B.13 : Energy deposition of all particles with various moderators along the target depth.

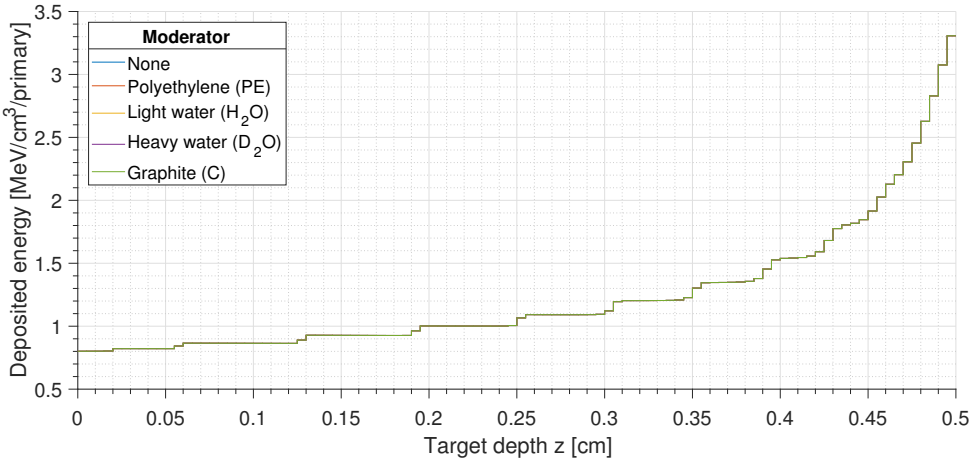

B.14 : Energy deposition of protons with various moderators along the target depth.

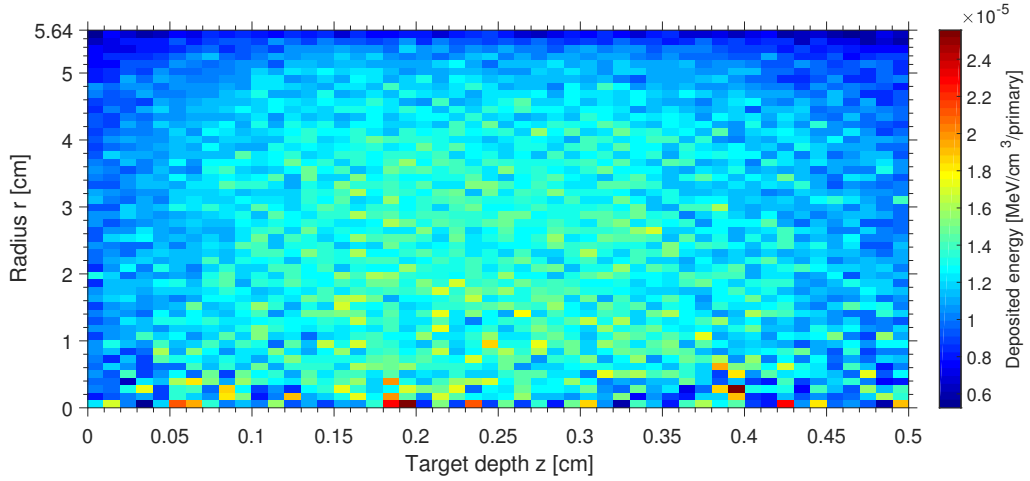

B.15 : Energy deposition of neutrons as a function of the target depth and radius for a D_2O moderator.

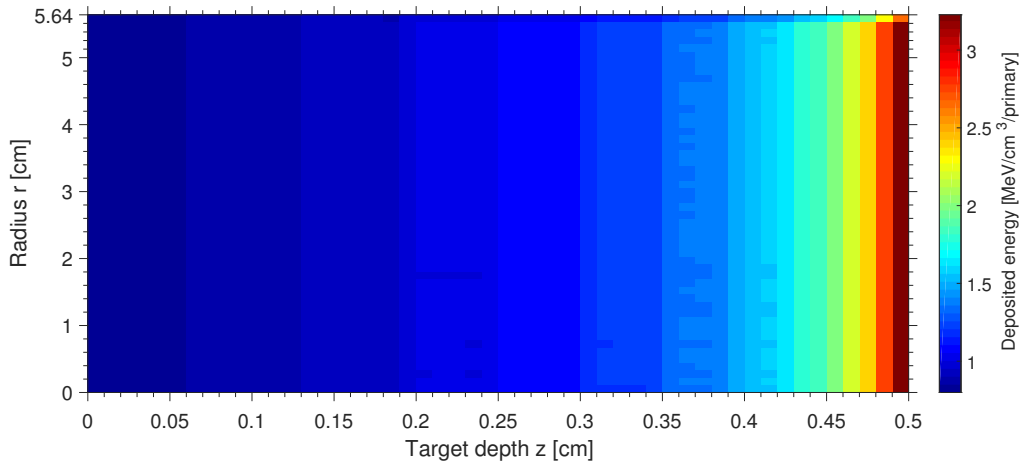

B.16 : Energy deposition of all particles as a function of the target depth and radius for a D_2O moderator.

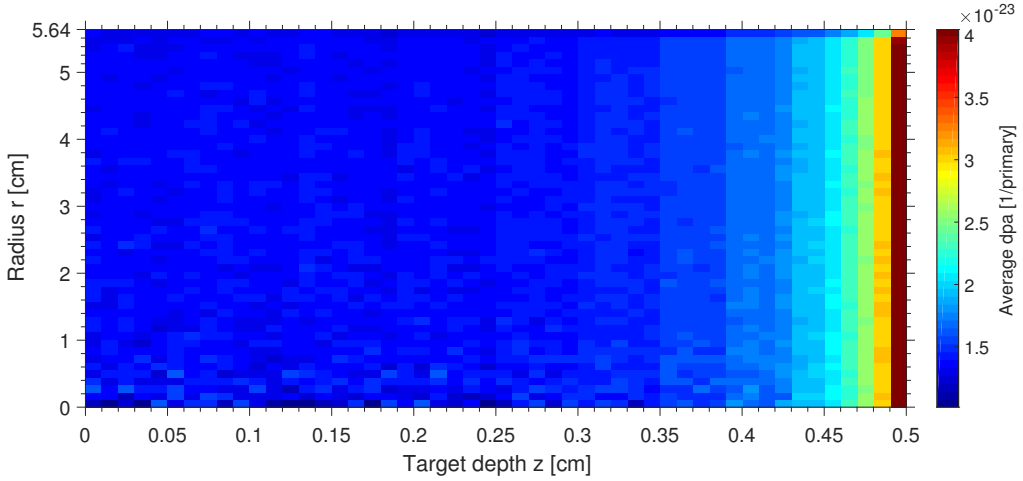

B.17 : Atomic displacements of all particles as a function of the target depth and radius for D_2O moderator.

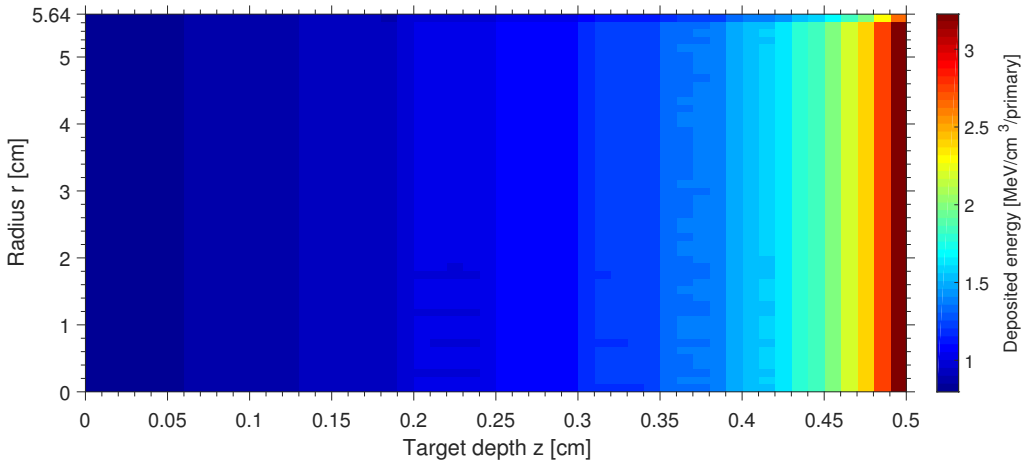

B.18 : Energy deposition of protons as a function of the target depth and radius for a D_2O moderator.

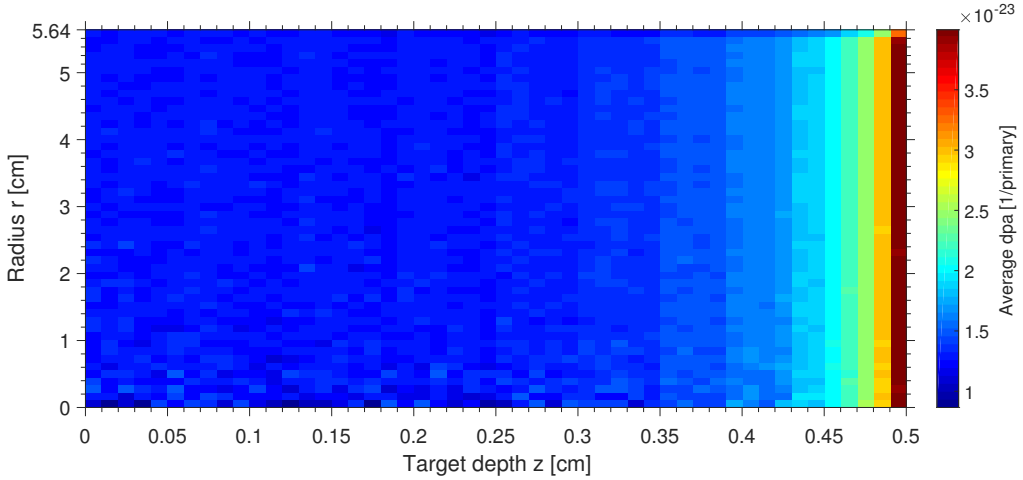

B.19 : Atomic displacements of protons as a function of the target depth and radius for a D_2O moderator.

B.20 : FLUKA numerical *DPA-SCO* results for the annual displacement dose.

Moderator	Annual dose [dpa]					
	Average			Peak		
	Tot.	p^+	n	Tot.	p^+	n
No	4.43	4.20	0.17	12.06	11.92	0.19
Polyethylene (PE)	4.43	4.20	0.18	12.07	11.93	0.20
Light water (H_2O)	4.43	4.20	0.18	12.07	11.93	0.20
Heavy water (D_2O)	4.44	4.20	0.18	12.07	11.92	0.20
Graphite (C)	4.44	4.20	0.18	12.07	11.92	0.21

B.21 : FLUKA numerical *DPA-SCO* results for the damage rate R_d.

Moderator	Damage rate R_d [10^{-8} dpa/s]					
	Average			Peak		
	Tot.	p^+	n	Tot.	p^+	n
No	14.04	13.33	0.54	38.23	37.81	0.60
Polyethylene (PE)	14.06	13.32	0.57	38.28	37.82	0.63
Light water (H_2O)	14.06	13.32	0.56	38.27	37.81	0.63
Heavy water (D_2O)	14.06	13.32	0.57	38.27	37.80	0.64
Graphite (C)	14.09	13.33	0.57	38.29	37.80	0.65

B.22 : Average energy deposition in the target for all particles, protons and neutrons with and without moderators.

Moderator	Average energy deposition [MeV/cm^3/primary]		
	Total	Protons	Neutrons
None	1.23E+00	1.23E+00	1.10E-05
Polyethylene (PE)	1.23E+00	1.23E+00	1.13E-05
Light water (H_2O)	1.23E+00	1.23E+00	1.13E-05
Heavy water (D_2O)	1.23E+00	1.23E+00	1.15E-05
Graphite (C)	1.23E+00	1.23E+00	1.17E-05

B.23 : FLUKA numerical NIEL dpa results. The results were obtained for the simple geometry, for a better comparison also the corresponding *DPA-SCO* method values are given.

Average annual displacement dose [dpa]					
Total		**Protons**		**Neutrons**	
DPA-SCO (NRT)	**NIEL (KP)**	**DPA-SCO (NRT)**	**NIEL (KP)**	**DPA-SCO (NRT)**	**NIEL (KP)**
4.43	11.87	4.20	11.48	0.17	0.23
KP/NRT= 2.68		KP/NRT= 2.73		KP/NRT= 1.35	
Peak annual displacement dose [dpa]					
12.06	25.51	11.92	25.32	0.19	0.25
KP/NRT= 2.12		KP/NRT= 2.12		KP/NRT= 1.32	

C. Evaluation supporting data

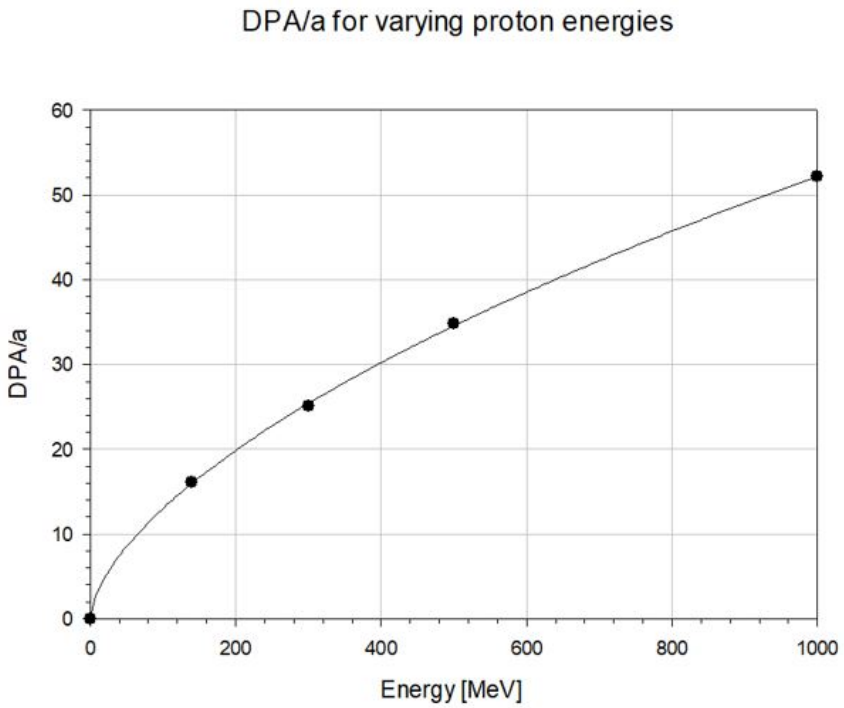

C.1 : Extrapolation of the dpa values in a Ta spallation target obtained by C. Villagrasa-Roussel et al. The curve was fitted with a sigmoidal hill fitting with 3 parameters. [174]